The University Of Sheffield.

Oxide ion conductivity, Resistive-switching and Ferroelectricity of Doped-HfO_2

A thesis Submitted for the Degree of Doctor of Philosophy

Meshari Mohammed Alotaibi

Supervisor: Prof. Anthony R. West

Department of Materials Science and Engineering
Faculty of Engineering

August 2022

Part of this work resulted in the following manuscripts that have already been published.

- Alotaibi, M., L. Li, and A. R. West, Electrical properties of yttria-stabilised hafnia ceramics. Physical Chemistry Chemical Physics, 2021. **23**(45): p. 25951-25960.

- Alotaibi, M., Almutairi, F., and A. R. West, Resistive-switching in yttria-stabilized hafnia ceramics. Journal of the American Ceramic Society, 2023. **106**(2): p. 822-828.

- Schroeder, U., T. Mittmann, M. Materano, P.D. Lomenzo, P. Edgington, Y.H. Lee, M. Alotaibi, A.R. West, T. Mikolajick, and A. Kersch, Temperature-Dependent Phase Transitions in $Hf_xZr_{1-x}O_2$ Mixed Oxides: Indications of a Proper Ferroelectric Material. Advanced Electronic Materials, 2022 **8**(9): p. 2200265.

Acknowledgements

In the name of Allah, the Most Gracious and the Most Merciful. All praises to Allah for His blessing in completing this thesis.

This thesis is the outcome of 7 years of studying in the University of Sheffield. After these long years that have many alternate moments of frustration and exciting discovery, there is one remaining responsibility which is to express my thanks and appreciation to all those people and institutions who assisted me. First of all, I should send my thanks to the University of Sheffield and saying that these seven years was not only educational experience challenging, but also valuable living and environment experience that make me a better person. Also, I would especially thank my supervisor Professor Anthony R West for his support, patience and encouragement to me since I joined his group 6 years ago in my masters project. Professor West gives me a rich scientific experience that builds me to be a good researcher who is able to think, do, and analyse scientific works in his field.

I cannot forget to show my deep gratitude to all members of the Functional Materials and Device Group. Thank you so much for your help in the laboratories and your valuable meetings on Tuesday every week. The help and meetings were the energy that assisted me to enjoy and continue in this scientific journey.

Special thank, from bottom of my heart, is also extended to my mum (Nora), dad (Mohammed), wife (Munirah) and daughter (little Nora) for their love, care, and motivation through these years of studying abroad. My mum, dad, wife and daughter, I never forget the endless support and strength you gave me to reach this position.

I would like, also, to acknowledge all my colleagues and friends, unfortunately too numerous to mention individually, who have generously given their time, ideas and expertise that kept me going.

Finally, a huge thanks go out to my sponsor, Taif university, for a scholarship that was a base which I have stood on to obtain my Masters and Phd degrees.

Meshari Alotaibi
August 2022

Abstract

Yttria-stabilised hafnia, $Hf_{1-x}Y_xO_{2-x/2}$ (x=0.15, 0.30 and 0.45), ceramics were prepared by solid state synthesis and characterised by *ac* impedance spectroscopy. Electrical conductivity of x=0.15 is one order of magnitude higher than x=0.30 and 0.45. All compositions are foremost oxide ion conductors but they contain a small p-type electronic conduction via increasing Y^{3+} concentration and pO_2. YSH materials therefore are mixed conductors. P-type conductivity is attributed to created holes that is believed to be located on under-bonded oxide ions.

A study on the effect of a small dc bias on YSH ceramics shows enhancement of their conductivity, transforming into a resistive switching behaviour. This behaviour is novel for any bulk ceramics other than Ca-doped $BiFeO_3$. Switching of YSH depends on both oxygen partial pressure, pO_2, and temperature. At low applied voltage, the increase in the conductivity is associated with p-type behaviour commenced at the positive electrode/ceramic interface, but with further applied voltage, YSH underwent a transition from p-type to n-type behaviour which is commenced at the negative electrode/ceramics interface. With increasing applied voltage, the total conductivity enhanced sharply by 1.5-2.5 orders of magnitude that is reversible with hysteresis under removal of the applied voltage.

The ac impedance results of $Hf_{1-x}Zr_xO_2$ thin films demonstrate a single homogeneous component attributed to the bulk layer. Resistance of all compositions decreased with increasing pO_2 (N_2-Air-O_2). This decrease in resistance is associated with p-type electronic conduction. In p-type materials, a decrease in resistance is related to the increase in number of holes that can probably be located on under-bonded oxygen or created during the preparation of the thin films. The equivalent circuit of a resistor in parallel with a series-connected CPE-C element gave best fitting to HZO thin film samples. Results of fixed frequency variable temperature sweeps of permittivity, e_r, of HZO show a sharp peak at 464-474 °C with a maximum permittivity of ~ 11100. This result is the first report of a peak in the permittivity of HZO thin films that is attributed to a transition from ferroelectric into paraelectric behaviour at T_c.

Table of Contents

Chapter 1: Introduction

1.1 Brief background

Hafnium oxide, HfO_2, has attracted continual scientific attention due to its distinctive properties. For a long time, HfO_2 has been known as a refractory material because of its low thermal conductivity and high melting temperature, ~ 2758 °C. In 2007, HfO_2 was introduced into the market as a typical high-k dielectric material and replaced SiO_2 that has leakage current issues when the thickness of the SiO_2 layer reduces.

Doping the parent oxide, HfO_2, with acceptor (lower valence) dopants such as Y^{3+} gives rise to high oxide conductivity, similar to that of yttria-stabilised zirconia, YSZ08. However, because of the expensive cost of hafnia and its structural, physical and chemical similarity to ZrO_2, doped hafnia is excluded as the preferred choice for typical electrolyte material. Although YSZ is the classic oxide ion conductor, in recent studies, YSZ has been shown to exhibit electronic conductivity, especially in composition with increasing yttrium concentrations [1] and/or by the application of a small dc bias [2, 3]. This could cause a reduction in its efficiency as an electrolyte in various applications such as solid-oxide fuel cells, SOFCs, oxygen sensors and oxygen separation membranes.

Field-assisted sintering technology (flash-sintering) is a novel densification technique that utilizes the application of a dc bias and heat treatment to sinter particular materials at low temperatures and in a few seconds. Sintering occurs along with a very fast temperature rise, an increase in electrical conductivity and a clear luminescence (flash) event. YSZ is the material that has been used intensively in this technique. Therefore, there is a clear interest to determine (i) whether or not electronic conduction of YSZ is a more general phenomenon in ceramic oxides, and (ii) whether it is important in the flash-sintering technique.

In 2011, ferroelectricity was reported in doped hafnia thin films. Böscke et al. [4] stabilised an orthorhombic phase of doped hafnia under the effect of electrode mechanical stress. Subsequently, a lot of effort has been made in academia and industry communities to understand the ferroelectric properties in thin films of pure and doped HfO_2. The fluorite-

structure ferroelectrics show excellent properties such as a good remanent polarisation and a CMOS-compatibility with a high scalability which is better than that of the well-known perovskite-structure ferroelectrics. This allows HfO_2 thin films to be considered as a promising material in future memory applications. However, ferroelectric doped hafnia thin films show some critical issues such as wake up, fatigue effects and low dielectric permittivity that need to be analysed and understood in order to optimise the performance of ferroelectric hafnia film-based devices.

1.2 Aims, objectives and layout of thesis

This thesis presents an intensive investigation on the electrical properties of doped-HfO_2.

The first aim of this project was to study the oxide ion conductivity of yttria doped hafnium oxide (YSH) and compare it with yttria-stabilised zirconia (YSZ). It was proposed to achieve this by doping HfO_2 with Y^{3+} using solid-state synthesis, sintering ceramic samples and performing impedance spectroscopy measurements as a function of temperature, oxygen partial pressure, pO_2, and dc bias in order to:

1) investigate the effect of changing Y concentration on the electrical properties of hafnia;
2) determine whether YSH is sensitive to pO_2 or not;
3) examine if electronic conductivity can be induced by changing pO_2, similar to what has been reported for YSZ;

A completely unexpected result, that was obtained during the overview studies of YSH materials, was that the electronic conductivity induced by application of a small dc bias transformed into a resistive switching (RS) effect at higher temperature/voltage. This had been observed previously in bulk ceramics of only one material Ca-doped $BiFeO_3$ [5]. It therefore became of great interest as the second aim of the project. The mechanism of resistive switching in YSH ceramics was studied using impedance spectroscopy in order to:

1) identify the effect of pO_2 on RS behaviour of YSH;
2) study the effects of temperature on this behaviour;
3) investigate the effect of changing Y concentration on RS behaviour of YSH;

During this project, we became aware of the research on ferroelectric hafnia films by the Schroeder group in Germany. We requested some samples from them to compare their impedance characteristics with these of our own ceramics samples. The third aim then became to study the electrical properties of doped hafnia thin films by impedance spectroscopy measurements as a function of temperature and oxygen partial pressure, pO_2, so as to:

1) investigate the effect of temperature on the electrical impedance properties of doped HfO_2 thin films;

2) determine their sensitivity to pO_2;

3) measure their permittivity over a wide range of temperatures;

The thesis is presented in the following chapters:

Chapter 1 presents a brief background, aims and layout of the thesis.

Chapter 2 discusses the concepts and basic theory related to oxide ion conductors, ferroelectrics and resistive switching. This chapter, also, gives an overview of HfO_2, its structures and electrical properties.

Chapter 3 describes the characterisation techniques employed to study the properties of doped HfO_2.

Chapter 4 reports the oxide ion conductivity and electronic conduction of cubic-yttria stabilised hafnia, ceramics of formula, $Y_xHf_{1-x}O_{2-x/2}$.

Chapter 5 shows resistive switching behaviour in YSH ceramics.

Chapter 6 reports impedance analysis of $Hf_{1-x}Zr_xO_2$ thin films.

Chapter 7 gives a summary of the main conclusions and suggestions for future work to answer questions raised in this research work.

Chapter 2: Literature review

2.1 Oxide ion conductors

Oxide ion conductors are usually metallic oxides that possess an anionic conduction mechanism. In the past decade, there has been a much attention on oxide ion conductors, driven by the need for new clean power sources with high energy efficiency such as solid oxide fuel cells (SOFCs) as well as new oxygen sensors [6-9]. The aim of this section is to give a clear overview of the fundamental phenomena associated with oxide ion conduction in the solid state, materials that show oxide-ion conductivity and the application of these materials as solid-state electrolytes.

Compounds that exhibit oxide ion conduction are found among oxides that have quadrivalent cations with the fluorite crystal structure such as CeO_2 and ThO_2 or distorted fluorite structures such as ZrO_2 and HfO_2. Since oxygen vacancies are the main contributor to ionic conductivity, these oxides are usually doped with either rare earth elements such as (Sc^{3+}, Y^{3+} and Gd^{3+}) or alkaline earth elements such as Ca^{2+} and Mg^{2+} to create oxygen vacancies as the charge compensation mechanism and also to stabilize the cubic fluorite structure.

The migration of oxygen ions occurs when a) there are vacant anion sites that allow oxygen ions to move through and b) the energy barrier of the oxygen hopping process is relatively low. Oxide ion conductivity is obtained at high temperature in various materials in which the conductivity is strongly dependent on temperature. Oxide ion conductivity is also dependent on dopant concentration. With increasing dopant concentration, oxygen vacancies are created and therefore the charge carrier concentration is enhanced, leading to higher conductivity, but at some point the cation dopants start to interact with and trap the oxygen vacancies which reduces the conductivity [8, 10, 11].

The nature of the electrical behaviour of materials is affected by the defect equilibria within them. For example, in oxides with cubic fluorite structure and doped with lower oxidation state cations, the dominant ionic defects are anion vacancies, but electronic species might be introduced owing to the equilibrium between lattice and gaseous oxygen based on the following equation [10].

$$O_O^X \leftrightarrow 1/2O_2 + V_o^{\bullet\bullet} + 2e^- \qquad 2.1$$

A schematic plot of conductivity against partial pressure of oxygen (pO_2) is shown in Figure 2.1 for the materials that are oxide ion and electron conductors. Based on this schematic, materials may be classified according to the three types of conductions mechanism. The first are materials with n-type conduction mechanism where the conductivity increases on the logarithmic scale at low pO_2. The second are electrolyte materials that are located in the electrolytic domain. In this region, with different pO_2, the ionic transport number ($t_{i,}$) is equal to one which means the conductivity is not influenced by partial pressure of oxygen. The third type of material exhibits p-type conduction where the conductivity increases on the logarithmic scale at high pO_2. In this region, the specimens absorb oxygen either at the surface or in the positions of anion vacancies. Here, the absorbed oxygen dissociates and accepts electrons as shown in the following equation:

$$1/2O_2 + V_O^{\bullet\bullet} + 2e' \rightarrow O_O^X \qquad 2.2$$

That may also be written as

$$1/2O_2 + V_O^{\bullet\bullet} \rightarrow O_O^X + 2h^{\bullet} \qquad 2.3$$

when holes are introduced, they become the dominant charge carrier in the mechanism, leading to an increase in the conductivity [8, 10].

In order to obtain pure oxide ion conductors, the other conduction processes such as electronic or protonic should be negligible. For most oxide ion conductors, the introduction of electronic conduction in conjunction with oxide ion conduction is possible, producing mixed conduction. This introduction of electronic conduction can affect the performance of oxide ion conductors when they are used in the application as an electrolyte in SOFCs. Hence, a very limited number of oxides are pure oxide ion conductors. Both of these types, mixed conductors and oxide ion conductors are useful, but have different applications. This is discussed in more detail in the applications section.

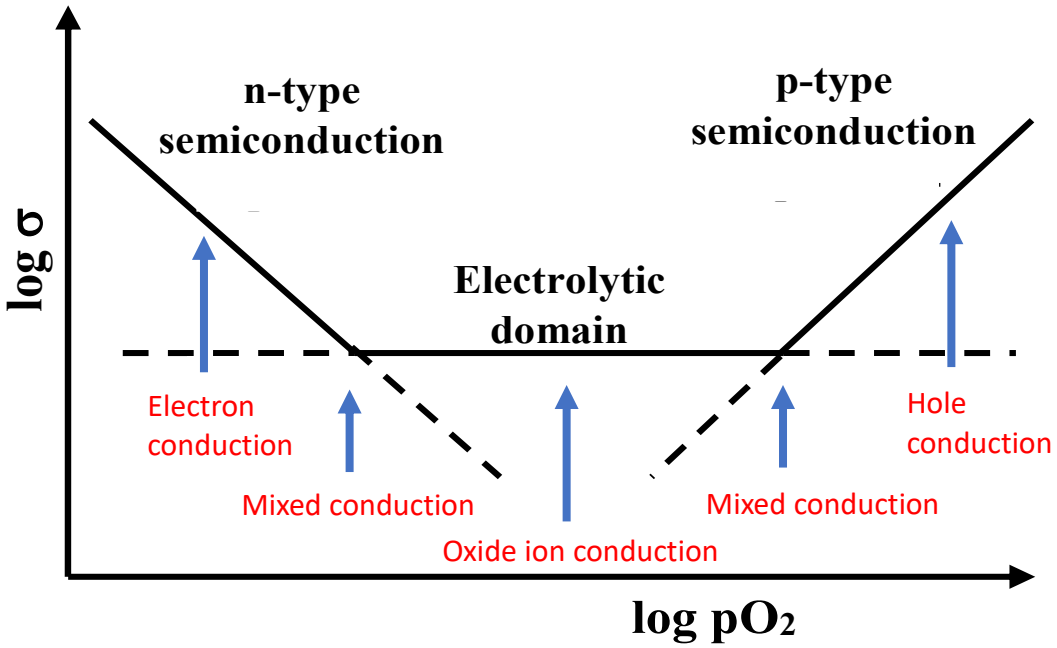

Figure 2.1 The electronic and ionic conductivity domains as a function of partial pressure of oxygen.

In terms of their structure, most oxide ion conductors can be divided into two well-known types: those with a cubic-fluorite structure and those with a perovskite structure. The fluorite-cubic structure is considered as the classical form of oxygen ion conductor because doped materials with the cubic-fluorite structure give the best oxide ion conduction properties compared with other structures. The oxides which have the cubic-fluorite structure at room temperature are ThO_2 and CeO_2, whereas ZrO_2 and HfO_2 have the fluorite structure only at higher temperature or when doped with lower oxidation state elements to induce a stabilised cubic structure at lower temperature. For perovskite-related structures, many studies have demonstrated the oxide ion conduction of doped perovskite (ABO_3) materials such as Al and Mg doped $CaTiO_3$ and doped $LaGaO_3$. More specifically, $CaTi_{1-x}(Al_x$ or $Mg_x)O_{3-\delta}$ shows oxide ion conduction of ~10^{-2} S cm^{-1} at 1000 °C with an oxide transfer number higher than 0.9 [12]. However, $CaTi_{1-x}(Al_x$ or $Mg_x)O_3$ is not desirable for Solid Oxide Fuel Cells (SOFCs) because its oxide ion conduction is lower than that of yttria-stabilized zirconia (YSZ). Surprisingly, $La_{0.9}Sr_{0.1}Ga_{0.8}Mg_{0.2}O_{3-\delta}$ shows oxide ion conduction higher than that of doped ZrO_2, but this material has partial electronic conduction along with the oxide ion conduction, affecting the performance in SOFC applications [13].

2.1.1 Fluorite-structured oxides

The importance of fast ionic conduction in the fluorite-type structure was first studied in 1839, when Faraday showed high ionic conductivity of lead fluoride (PbF_2) at elevated temperature [14]. Henceforth, the properties of oxide ionic conductors with fluorite-type structure have been widely studied. Currently, the preferred candidate for electrolyte materials in most (SOFCs) and oxygen sensors is fluorite-type oxide ionic conductors.

Fluorite-structured oxides are based on MO_2, where M is a tetravalent cation (Zr, Hf, Ce, etc.) located in a face-centered oxygen atom arrangement and surrounded by a cube of oxygen atoms. The space group of the ideal fluorite structure is $Fm\bar{3}m$. Each unit cell contains four M atoms surrounded by eight oxygen atoms as shown in Figure 2.2. MO_2 can be doped with lower valent (divalent or trivalent) oxides by replacing part of the host cations by lower-valent cations which lead to create oxygen vacancies in the anion sublattice so as to maintain the electroneutrality as illustrated in the following equations:

$$RO \rightarrow R''_M + V_O^{\bullet\bullet} + O_O^X \qquad 2.4$$

$$R_2O_3 \rightarrow 2R'_M + V_O^{\bullet\bullet} + 3O_O^X \qquad 2.5$$

The resulting ionic conductivity of doped fluorite-type oxides is largely dependent on the type of dopant as well as on the dopant concentration.

As is well known, the most important fluorite-structured oxide used as a solid electrolyte is yttria-stabilized zirconia, but It should be noted that YSZ is not the best oxide ion conductor because there are other materials which have much better ionic conductivity than YSZ such as CeO_2- 10 mole % Gd_2O_3 as shown in Figure 2.3. However, this material is unstable (the oxidation state of Ce is easily reduced from Ce^{4+} to Ce^{3+}). Its reduction is correlated with a small oxygen loss at higher temperature in atmospheres of lower pO_2. Oxide ions lost from the lattice form O_2 molecules and inject electrons into the structure according to equation 2.1. This electronic conduction is going affect the performance of Gd doped CeO_2 when it is used as an electrolyte.

Electrolytes based upon Bi_2O_3 show the highest oxide ion conductivity with cubic-fluorite structure and have 25% of oxygen vacancies at high temperature. However, below 729 °C the structure of δ-Bi_2O_3 is transformed from cubic to a monoclinic phase, α-Bi_2O_3,

Figure 2.3. $(Bi_2O_3)_{0.75}(Y_2O_3)_{0.25}$ exhibits a greater oxide ion conductivity at high oxygen partial pressure, but is reduced easily at low oxygen partial pressure which affects its performance as an electrolyte for SOFC applications.

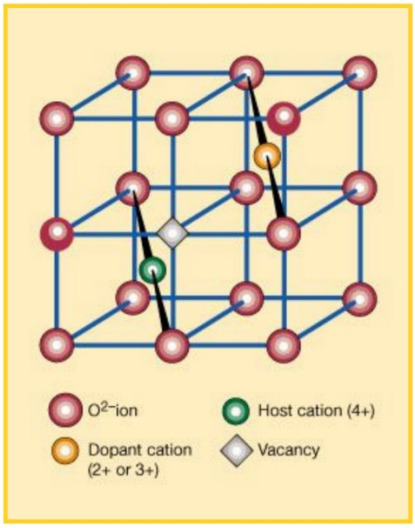

Figure 2.2 The fluorite-cubic structure of doped MO_2 [15].

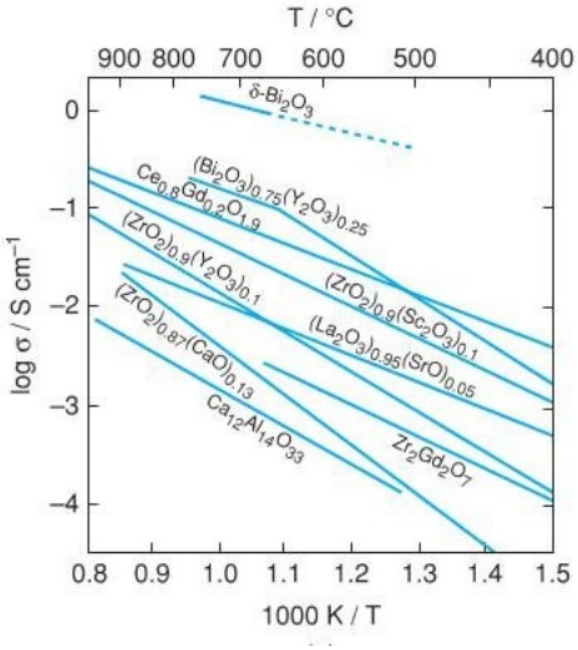

Figure 2.3 Arrhenius plot of common oxide ion conductors [8].

2.1.2 Doped Zirconia

Although several metal oxides and rare-earth oxides have been studied as oxide ionic conductors over recent decades, stabilised-zirconias are still the best-known oxygen ion conductors. However, it has been shown that increasing dopant concentration ($x > 0.2$) causes a reduction in the ionic conductivity. This is related to two possible explanations. First, oxygen

vacancies attract dopant cations to form defect clusters. This occurs because oxygen vacancies have a net two positive charge ($V_o^{\bullet\bullet}$) , while the substituted atoms carry a net negative charge (Y'_{Zr} and Ca''_{Zr}) and therefore these oppositely-charged defects have a natural tendency to attract each other [8, 10, 16] with an energy of association E_{ass}. Second, Hull [17] argued that the reduction in the ionic conductivity with increasing x is dominated by cation-anion vacancy interactions ($V_o^{\bullet\bullet} - Zr - V_o^{\bullet\bullet}$) that correlate with the size of the Y^{3+} ion (1.02 Å). The larger size of the Y^{3+} atom forces oxygen vacancies to be near Zr^{4+} that has an ion radius of 0.84 Å, leading to extensive strain in the lattice, hindering diffusion of the oxygen vacancies.

Electrical conductivity of doped Zirconia

The typical conductivity value of YSZ08 is 10^{-1} – 10^{-2} S/cm at 800 ^{o}C with an activation energy 0.8-1.3 eV which is better than calcium doped zirconia, Figure 2.3. However, some doped zirconias have a higher conductivity than YSZ08 such as $Zr_{0.8}Sc_{0.2}O_{1.9}$, but this material suffers from problems with aging (when ZrO_2- 7 mol% to 11mol% Sc_2O_3 is annealed as a function of time, the ionic conductivity decreases) [8, 10, 16, 18]. Also, Scandium doped zirconia has a problem with stabilization of the cubic phase in the whole temperature range of interest. The ZrO_2-$ScO_{1.5}$ system shows appearance of a rhombohedral phase (the intermediate beta-phase, $Zr_7Sc_2O_{17}$) that does not occur in the ZrO_2-Y_2O_3 system. This cubic to rhombohedral phase transition has a considerable impact on the ionic conductivity of Scandium doped Zirconia [17].

Recently, Yttria-stabilized zirconia has shown that electronic conduction can be induced in the material by application of a small dc bias voltage or increasing Y concentration [2]. Figure 2.4 shows that the resistivity of $Zr_{1-x}Y_xO_{2-x/2}$ (x=0.4, 0.5, 0.6 and 0.7) decreased when changing atmosphere from N_2 to O_2 gas. The decrease in resistivity became larger with compositions that have high yttrium concentration. This indicates that there is electronic conduction in $Zr_{1-x}Y_xO_{2-x/2}$, and it is believed that YSZ08 itself will have electronic conduction when the pressure of O_2 is just above 1 atm [1]. This electronic conduction is going to affect the usefulness of YSZ08 when it is used as electrolyte in various applications such as SOFCs or oxygen sensors.

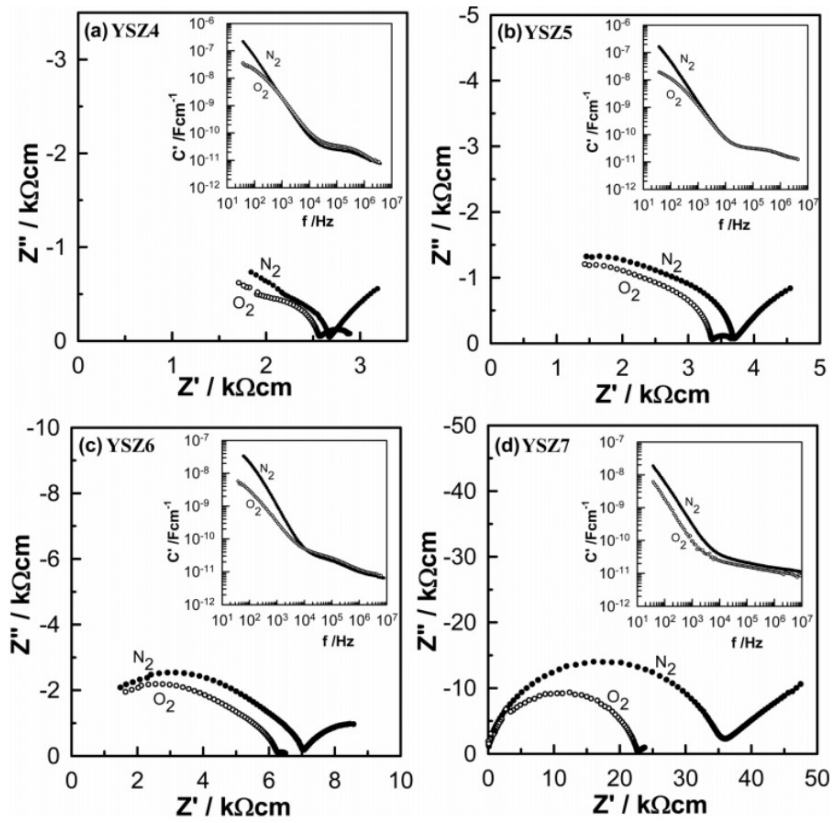

Figure 2.4 Impedance complex plane plots and capacitance spectroscopic plots of YS4, YSZ5, YSZ6 and YSZ7 at 750 °C under different atmosphere [1].

2.1.3 Applications of oxide ion conductors

Solid electrolyte sensors

Solid electrolyte sensors can be used to measure the partial pressure of gases dissolved in liquid. The most sophisticated sensor based upon a solid electrolyte is the oxygen sensor which is composed of a stabilised zirconia electrolyte in the form of tube, as shown in Figure 2.5. Inside the tube is the reference gas and (usually) is air. A porous metal electrode is utilised to coat the tube for catalysing oxygen gas absorption and liberation. In terms of measurements, P''_{O_2} is the oxygen partial pressure of the reference gas and P'_{O_2} is the oxygen partial pressure of the test gas. When measurements are taken, if P'_{O_2} is less than P''_{O_2}, the oxide ions migrate from the internal side to the external side, according to the following equation:

$$4e^- + O_2 \rightarrow 2O^{2-} \qquad 2.6$$

$$2O^{2-} \rightarrow O_2 + 4e^- \qquad 2.7$$

The Nernst equation indicates the relationship between the difference in the partial pressure of oxygen either side of the electrolyte and cell voltage and is expressed as follows:

$$E = \frac{RT}{4F} \log_e \left(\frac{P''_{O_2}}{P'_{O_2}}\right)$$

The difference in voltage between the internal and external electrodes is employed to measure P'_{O_2}.This type of sensor is well-known commercially and used in various applications. Vehicle exhaust gas analysis in combustion engines, for example, use the oxygen concentration cell to improve the efficiency and decrease the content of toxic gases such as CO and NO_x. Another application is to measure the oxygen content of molten iron in the metals industry [8, 19].

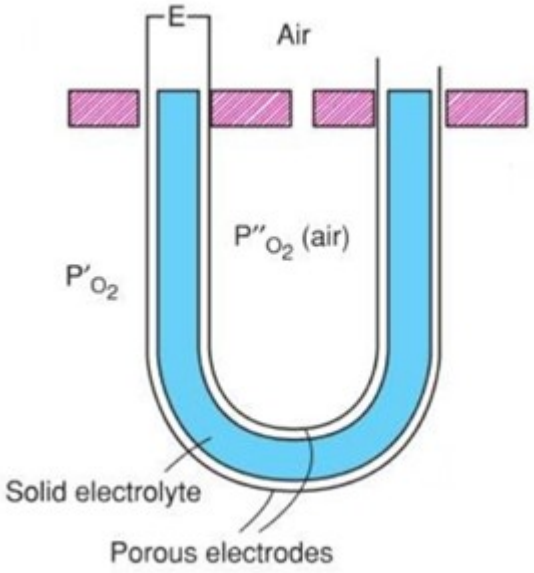

Figure 2.5 Schematic diagram of an oxygen sensor [8].

Solid Oxide Fuel Cell (SOFC)

Solid oxide fuel cells have been widely used in many applications as a power source due to their outstanding advantages, including friendliness for the environment (no NO_x and SO_x emission) and high efficient production of electricity [20]. SOFCs consist of three parts: electrolyte and two electrodes (cathode and anode). The electrolyte part, with yttria-stabilized zirconia as a typical candidate, is sandwiched between Ni/ZrO_2 cermet and Lanthanum Manganite $LaMnO_3$. The basic operation of a SOFC is illustrated in Figure 2.7. When the load is applied to the cell, oxygen is reduced at the cathode part (Air electrode) and oxide ions are produced according to the following equation:

$$4e^- + O_2 \rightarrow 2O^{2-} \qquad 2.8$$

The oxide ions migrate through the electrolyte to the anode (Fuel electrode) and react with H_2 or CO, producing H_2O or CO_2 according to the following equations:

$$CO + O^{2-} \rightarrow CO_2 + 2e^- \qquad 2.9$$

Or

$$H_2 + O^{2-} \rightarrow H_2O + 2e^- \qquad 2.10$$

The SOFC electrolyte has particular requirements needed in order to perform optimally, see Figure 2.6. The electrolyte should be a pure ion conductor which means the amount of electronic and protonic contribution in the total conductivity must be zero or low in order to prevent any leakage of the electrons that lower the performance. By contrast, the electrode materials should be mixed conductors (electronic and ionic).

SOFC has many forms of design (e.g. planar and tubular) but the most advanced design has been accomplished with a Siemens Westinghouse tubular cell [8, 21]. All active cell components in this design are deposited as thin layers and the materials for each component are listed in Table 2.1.

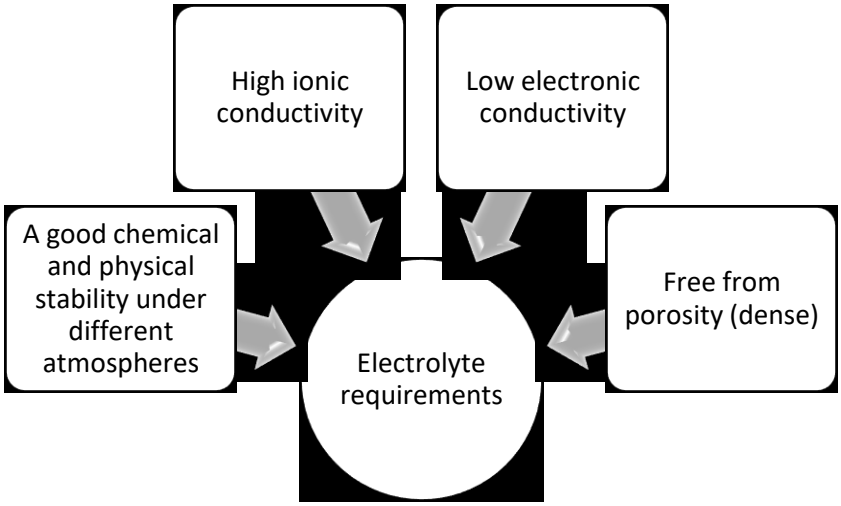

Figure 2.6 Characteristic conditions of the electrolyte.

Table 2.1 Cell components and materials of the Westinghouse Solid Oxide Fuel Cell.

Component	**Material**
Fuel electrode	Ni/ZrO_2 Cermet
Electrolyte	$ZrO_2(Y_2O_3)$ ((YSZ))
Air electrode	$LaMnO_3$
Interconnection	$LaCr(Mg)O_3$

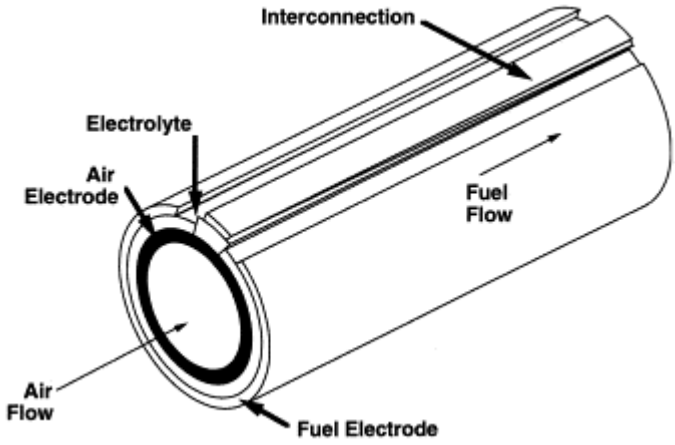

Figure 2.7 Schematic diagram of a tubular SOFC [20].

2.2 Ferroelectricity

Ferroelectric behaviour was discovered in Rochelle salt ($NaKC_4H_4O_6.4H_2O$) by Valasek in 1921. Ferroelectric materials are defined, from a physical point of view, as crystals that exhibit spontaneous polarisation, which can be reoriented by an external field.

There are two sorts of ferroelectric. The first one is the order-disorder type in which the movement of hydrogen atoms is involved such as in the polarisation of KH_2PO_4. The second one is the displacive type that occurs with $BaTiO_3$, in which one type of cation can undergo displacements of ~ 0.1 Å relative to adjacent anions. These displacements cause the dipole and high permittivity that characterise ferroelectrics. Therefore, the crystal structure must be non-centrosymmetric [8, 21]. This type of spontaneous polarisation occurs below a temperature known as the Curie temperature. When the temperature is above the Curie temperature, the linked displacement of adjacent octahedra starts to break down, the material is paraelectric (no ferroelectricity) and its permittivity obeys the Curie-Weiss Law according to the following equation [8, 21, 22]:

$$\varepsilon_r - 1 = \frac{C}{T - T_0}$$

where T_0 is the Curie-Weiss temperature, C is Curie constant and ε_r is the relative permittivity.

There are certain features of ordinary dielectrics that can be used to identify ferroelectric materials. Firstly, extremely high bulk permittivity. Secondly, the probability of storing some electrical polarisation after switching off the applied voltage. Thirdly, a hysteresis loop between polarisation P and electrical field which indicates reversibility on application of a reverse field. When the applied voltage on dielectric materials is increased, the relative polarisation or stored charged increases [8]. With ferroelectrics, the linear dependence of polarization on field is not obtained when the field is subsequently reduced. As a result, a polarisation loop is obtained, Figure 2.8. The saturation polarization (P_s) of ferroelectrics is obtained at high field strength and the remanent polarization(P_r) is the value stored as the field decreases to zero after saturation. In order to reduce the polarization to zero, application of a reverse field (*coercive field* E_c) is needed as shown in Figure 2.8.

Many ferroelectric materials have a distorted perovskite structure. These materials contain cations which are readily displaced off their central position when their size is slightly too small to occupy the octahedral site. Ti^{4+} and Nb^{5+} are typical examples of such ions which

are usually found in ferroelectric materials. The non-centrosymmetric coordination pf anions in MO_6 octahedra is responsible for spontaneous polarisation and a dipole moment.

The tolerance factor of ferroelectric $BaTiO_3$ is 1.01 (>1) causing displacement of the B-site cations in $BaTiO_3$, Figure 2.9. Once an electric field is applied, Ti^{+4} moves, leaving its central position, in one direction and O^{2-} moves in another, thereby producing the net dipole moment in the unit cell. This dipole is also responsible for forming domains in which the dipoles in adjacent unit cells are aligned in a specific direction. When the electric field is removed, the remanent polarisation (P_r) is stored and can be removed by application of the coercive field (E_c). Above 120 °C (its Curie temperature), a phase transformation takes place and the structure changes from tetragonal to cubic, resulting in the disappearance of ferroelectric behaviour, Figure 2.10 [8, 21].

Not all perovskites show evidence of ferroelectric behaviour: whilst $BaTiO_3$ is ferroelectric, $CaTiO_3$ is not. The cause of this difference is associated with radii of the ions involved. In $BaTiO_3$, the larger Ba^{2+} gives an expansion of the unit cell that creates a longer bond between Ti-O. This allows ions to have positional flexibility within the TiO_6 octahedra. In contrast, $CaTiO_3$ has a distorted perovskite structure with a tolerance factor less than one. In $CaTiO_3$, the smaller Ca causes a partial collapse in the unit cell which leads to a rotation/tilting of the TiO_6 octahedra [8, 23].

In order to use ferroelectric oxides in practical application such as capacitors, the relative permittivity (ε') should be high. So, to maximise the ε', it is essential to reduce the Curie temperature as near as possible to room temperature. The Curie temperature of $BaTiO_3$ is reduced by partial substitution of either Ba^{2+} by smaller ions or Ti^{4+} by larger ions. The replacement of Ba^{2+} by Sr^{2+} ,for instance, introduces a contraction in the unit cell and a decrease in Tc [8].

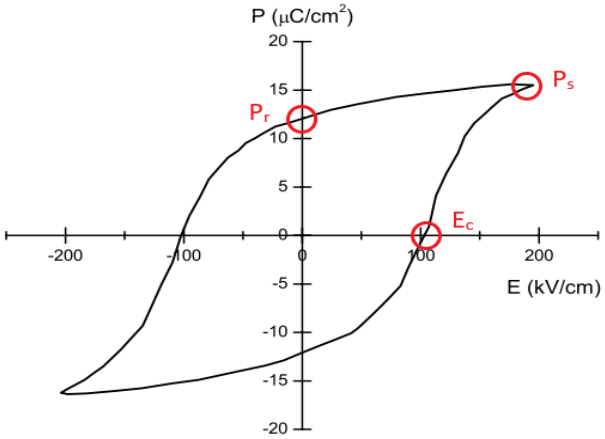

Figure 2.8 A hysteresis loop of a ferroelectric material [24].

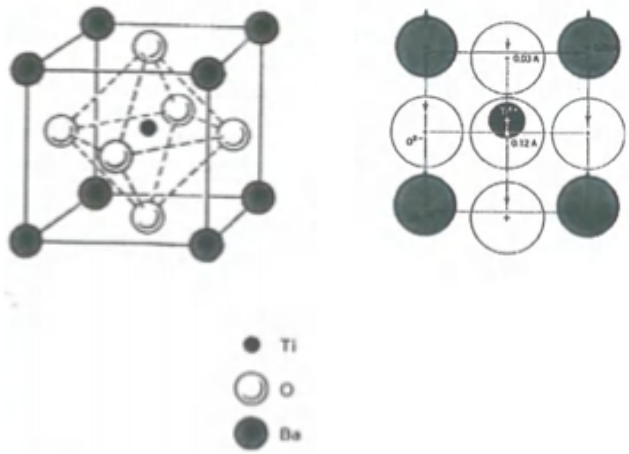

Figure 2.9 The Crystal structure of $BaTiO_3$, oxygen occupies faces, barium occupies the corners and Titanium occupies the centre site [21].

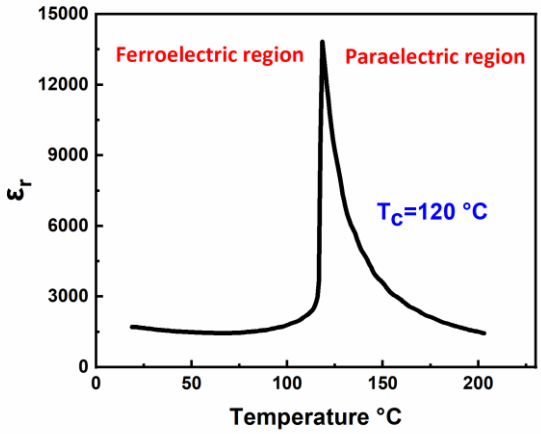

Figure 2.10 Permittivity of $BaTiO_3$ versus temperature.

2.2.1 The ferroelectricity of thin film materials

Thin film ferroelectrics began to be studied and developed in the 1970s. Due to the sophisticated techniques needed to produce high-quality films, and the applications that need materials in the form of films, their development has accelerated rapidly in recent years. Ferroelectric thin films usually, as bulk materials, show properties that are related to their composition and microstructure. However, thin film materials may possess different properties induced by their closeness to the supporting substrate [25]. Also, the preparation process of thin film devices is complicated which can affect their quality, reliability and similarity to bulk ceramics properties. First, thin film devices consist of multiple layers that play a role in the thin film functional properties. Second, the lower deposition temperature of these devices has a big influence of the stability of the structure and the bulk properties [26]. Third, as thin film thicknesses are usually a few micrometres or nanometres, contamination during film preparation may lead to large changes in their electrical and other physical properties [27, 28]. Fourth, adhesion between the substrate and deposited materials is a vital factor in which the formation and structure of films depend on [29]. Fifth, uniformity and thickness of the films have been found to have a significant impact on the performance and reliability of thin film devices [30]. Hence, the quality of the film device depends greatly on several factors in order to obtain the thin film device with the desired properties.

The effect of thin films on the Curie temperature

Film thickness and stress play a crucial role in the properties of ferroelectric materials. The Curie temperature of $BaTiO_3$, for example, has been observed to increase with decreasing film thickness and was attributed to a stress effect. An increase in the Curie temperature and coercive field, reduction in remanent polarization and diffusive nature of the phase transition temperature with increasing compressive stress was reported [31]. The stress effect can be reduced by an appropriate selection of deposition conditions. $BaTiO_3$ films deposited on a Si substrate had low intrinsic stress and showed ferroelectric properties close to those obtained in single crystal $BaTiO_3$ [32]. In another study, $BaTiO_3$ layers deposited between two thin $LaNiO_3$ (LNO) electrodes were found to have a lower Curie temperature than bulk $BaTiO_3$. Also, the Curie temperature is shifted to lower temperature (89 to 64 C) when the thickness of the $BaTiO_3$ film decreased from 1 μm to 35 nm [33] and was attributed to tensile stress in the $BaTiO_3$ layers.

Source of stress

Interaction between the film and substrate can play a significant role in generating mechanical stresses which can be categorized into thermal, intrinsic and extrinsic stresses.
Thermal stresses are caused by the differences between the thermal expansion coefficients of the film and the substrate which cause problems as a result of differences between working and deposition temperature.
Intrinsic stresses are often associated with film growth parameters such as pressure, temperature, reactant conditions and impurities which are significant contributors to form the state of intrinsic stress. Generally, intrinsic stress is formed by the ions and atoms that are not in their lowest energy configuration when they are deposited as a film. So, compressive stresses are generated when the atoms are closer to each other than they would be in equilibrium circumstances, while tensile stresses are generated when atoms are further apart than in the equilibrium state.
Extrinsic stresses are generated by structural changes, leading to dimensional changes. Most films show an increase in density due to structure development, such as crystallization of amorphous phase and densification which can lead to shrinkage and tensile stress in the film [32, 34].

2.3 Resistive-switching behaviour:

Resistive switching, *RS*, is physical behaviour in which a material's electrical resistance changes under the application of external electric field. The switched resistance state is stable and can be maintained for a long time [35]. The change in resistance is different from dielectric breakdown which means it is non-volatile (reversible) and the original state can be recovered on the removal of the electric field [35]. RS is induced by one of four proposed mechanisms: electro-chemical reaction (ion migration and redox), crystal structure changes (thermal activation of amorphous-crystalline transition), ferroelectricity or tunnel magnetoresistance [36]. After being known for 5 centuries, RS behaviour has received much current interest because of its possible applications in the next group of electronic devices. One of the most promising technologies using RS behaviour is resistive-random access memory, *RRAM,* that is considered a strong candidate for a diverse range of storage applications as a result of its high switching speed, low operating applied field, simple

structure and good scalability [35, 37, 38]. Materials that exhibit RS are among transition metal oxides (binary and perovskite type), high-k dielectrics (such as Al_2O_3 and Gd_2O_3), and non-oxides such as organic and chalcogenide materials [35, 39]. Therefore, classification of RS behaviour is different from material to material depending on switching and conductive behaviour.

2.3.1 Types of resistive-switching

After the past years of intensive research on understanding the physics of resistive switching phenomena, RS is categorised by three types: unipolar, bipolar, and threshold switching. In the unipolar type, the switched states of the system are dependent on only the amplitude of applied electric field, the switched states of the bipolar type depend on the amplitude and the polarity of applied electric field. For threshold switching, materials can show multiple states of RS, but have one stable state without application of applied electric field. This type shows no dependence on the polarity of applied field which is similar to unipolar switching. However, division of RS becomes less obvious when it comes to some systems such as TiO_2 that have been reported to have both types of resistive-switching [40, 41].

Unipolar switching

Unipolar switching materials are usually dielectrics such as simple binary transition metal oxides (TMO) i.e ZnO, TiO_2, HfO_2, ZrO_2, Fe_2O_3, and Nb_2O_5 [42, 43]. These materials are good insulators with high resistance values. In this type of RS, the resistance can be switched between a low resistance state (LRS) and high resistance state (HRS) by using the same polarity (unipolar) of applied field. Unipolar switching materials normally do not show RS behaviour. However, to get these materials into the switching region, application of a strong electric field ($V_{forming}$) is required to bring the materials near dielectric breakdown. This step is called as electro-forming process. In the SET stage, the systems show a large decrease in their resistance reaching a LRS that is stable (non-volatile). After that, to switch the system to a HRS, a field with the same polarity has to be applied, Figure 2.11. In this REST stage, the resistance increases dramatically, moving back to HRS (close to the initial state) [35, 37, 42].

The mechanism of unipolar switching is mostly associated with the creation and breakage of conductive filaments, CFs, Figure 2.12. In the original state, the defect concentrations (oxygen vacancies and metal interstitials) are low, and the system is in the HRS, Figure 2.12. When an external bias field is applied, oxygen ions are thermally assisted to

go to the anodic side and oxygen vacancies are generated inside the system. Perpendicular to the electric field, there are two other microscopic forces (Soret and Fick) which play a major role in the mechanism of RS, Figure 2.13. The Soret force depends on the temperature gradient which can cause oxygen ions to move from hotter to cooler areas to reduce its energy. This leads to the attraction of oxygen vacancies to form CFs and hence switch the system into LRS. In contrast, the Fick force, which is dominant in the reset process, is another force which works oppositely to the Soret force. As oxygen vacancies are non-uniformly distributed in the whole system and concentrated more in the CFs, the density gradient has a tendency to force them back, resulting in an increase in the entropy and a reduction in the free energy [35]. This can restore oxygen vacancies to their initial location and bring the system to HRS.

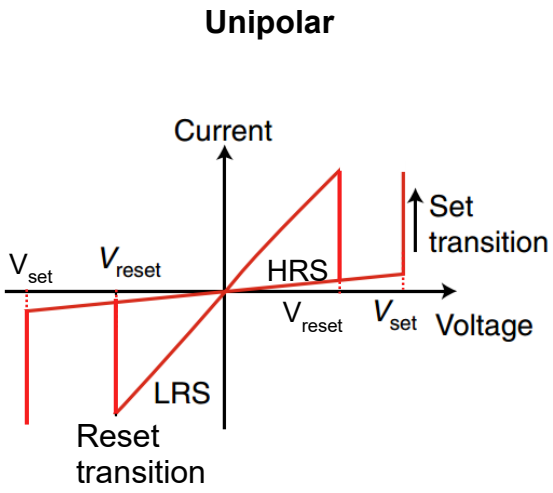

Figure 2.11 Current-voltage curve for unipolar switching in which the set transition from the high resistance state, HRS, to the low resistance state, LRS, occurs at the positive voltage, V_{set}, whereas the switching from the low resistance state, LRS, to the high resistance state, HRS, occurs at lower positive voltage, V_{reset}. $V_{set} > V_{reset}$.

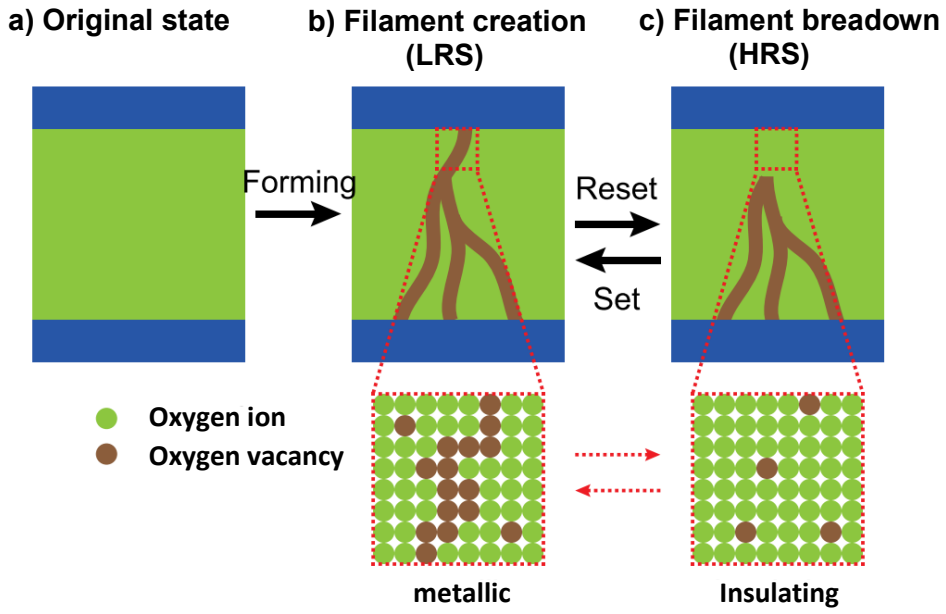

Figure 2.12 Illustrated schematic of unipolar switching mechanism, a) the original system, b) when the conductive filament is created bringing the system to LRS, c) breakage of conductive filaments leading to a switch to HRS. The system is switched between b and c by applying set and reset voltage [35].

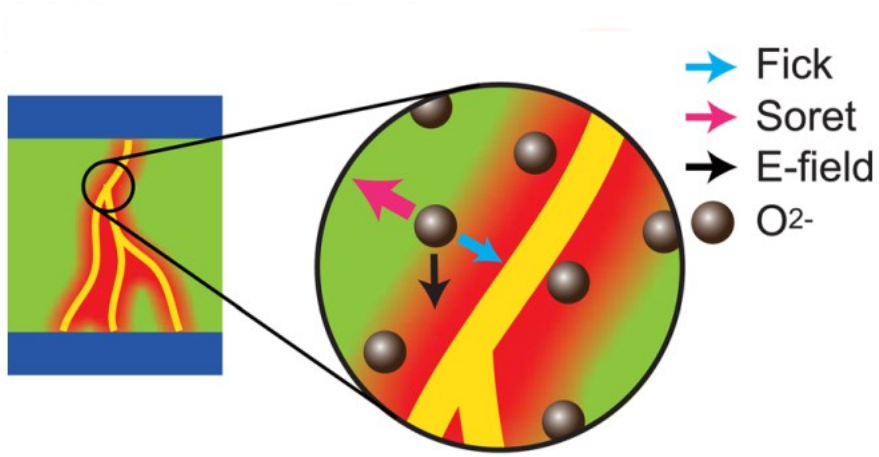

Figure 2.13 Illustrated model to present how electric field, temperature and density gradient affect the movement of oxygen ions [35].

Bipolar switching

Bipolar switching has been reported in various ternary oxides with perovskite structure such as Cr-doped $SrZrO_3$, $Pr_{1-x}Ca_xMnO_3$, and $La_{1-x}Sr_xMnO_3$. In this type of switching, the RS behaviour depends on the voltage polarity in which the switching from HRS into LRS occurs at the positive voltage, while the switching from LRS into HRS occurs at the negative voltage, Figure 2.14. The dependence of voltage polarity indicates the involvement of charged species in the switching mechanism. Electrons and oxygen vacancies are thought to be important elements in a bipolar switching mechanism. In most bipolar switching systems, electro-

forming processes usually are required and creation and breakage of CFs is similar to those reported in a unipolar switching type, Figure 2.15(a, b).

The mechanism of bipolar switching has been explained by three models, namely, growth and shrinkage of the virtual cathode via oxygen vacancy movements, controlling of the Schottky barrier via oxygen vacancy movements and trapping and de-trapping of electrons [35].

Growth and shrinkage of the virtual cathode

Since clustering of oxygen vacancies increases the system's conductance, movement of oxygen vacancies occurs under the voltage polarity –dependence. Oxygen vacancies can be created in the forming process as described in the unipolar switching section, or alternatively by doping in single phase oxide materials such as Y-ZrO_2 and Ca-$BiFeO_3$. Under the application of an electric field, positively charged oxygen vacancies migrate towards the negative electrode forming a region with a large cluster of oxygen vacancies. This region presented in Figure 2.15d, is the virtual cathode. Although this large cluster of oxygen vacancies is not clearly illustrated in the literature, this region is likely to be related to CFs. These CFs region extends to the positive electrode resulting in reduction in size of the gap between the virtual cathode and the positive electrode to a few nanometres.

When the negative field is applied, the virtual cathode is attracted to the anode forming CFs and the system switches to the LRS. When the positive field is applied, the virtual cathode is attracted to the cathode breaking the CFs and the system switches to the HRS [35, 44].

Controlling the Schottky barrier via oxygen vacancies

An electrode with a large work function such as Pt, Au and Nb-$SrTiO_3$ can produce a Schottky barrier at the interface between film and electrode. The height of interfacial barrier is inversely proportional to the concentration of oxygen vacancies. Therefore, any change in the oxygen vacancy concentration leads to change in the barrier height. When the negative field is applied at the anode, oxygen vacancies are attracted to the electrode reducing the interfacial barrier and this will switch the system to the LRS. In contrast, when a positive field is applied at the anode, mobile oxygen vacancies go away from the electrode increasing the interfacial barrier and this will induce the system to switch from LRS to HRS [35, 45].

Trapping and de-trapping of electrons

A few reports have suggested that control of a Schottky barrier can be achieved via trapping and de-trapping of electrons rather than oxygen vacancies. The suggestion states that a Schottky barrier can be obtained through the trapping and detrapping of injected electrons between oxides and a metal electrode interface. When a negative field is applied to the electrode, electrons are thought to be injected to the oxides and then trapped at defect sites neutralizing the oxygen vacancies. This leads to an increase in width of the Schottky barrier resulting in the system switching to the HRS. When a positive field is applied to the electrode, the trapped electrons are released which leads to recover the charge of the defects. As a result, the Schottky barrier width is narrowed bringing the system to the LRS [35, 46].

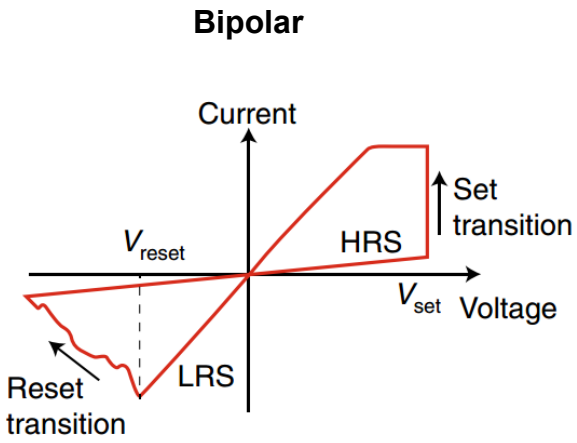

Figure 2.14 Current-voltage curve for bipolar switching in which the set transition from the high resistance state, HRS, to the low resistance state, LRS, occurs at the positive voltage, V_{set}, whereas the switching from the low resistance state, LRS, to the high resistance state, HRS, occurs at the negative voltage, V_{reset} [47].

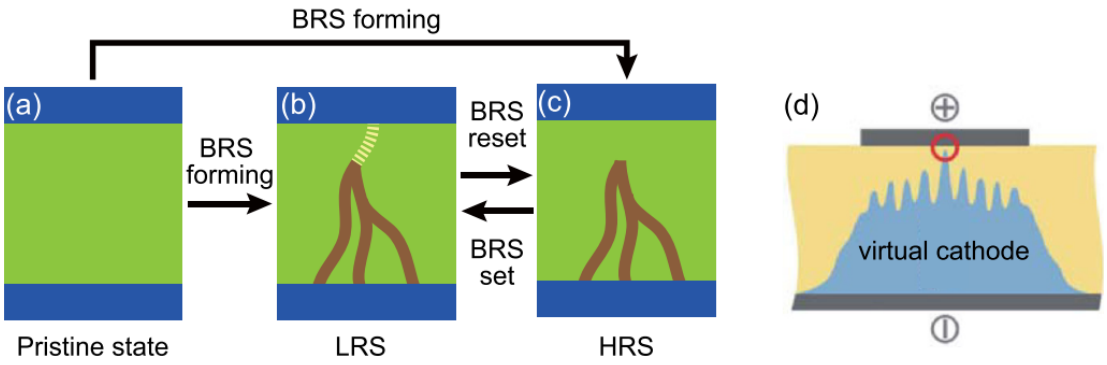

Figure 2.15 Illustrated schematic of bipolar switching mechanism, a) the original system, b) when the conductive filament is created bringing the system to LRS, c) breakage of conductive filaments leading to a switch to HRS. Different to unipolar switching, the system can enter either the LRS or HRS through a forming process and the system is switched between b and c by application of the opposite external field. d) A large accumulation of conductive filaments, called the virtual cathode, extending towards to the anode. When the virtual cathode touches the anode, the system enters the LRS [35].

Threshold switching

Threshold switching is a phenomenon which has one stable state without exposure to external bias voltage. Threshold switching systems show a transition from HRS into LRS with application of V_{set}. At the set stage, the LRS is stable over a particular range of applied voltages, but when the applied voltage reduces below this range, the resistance returns to the original state (HRS), Figure 2.16. Materials, that have been reported to have a threshold switching, are acceptor-doped $ATiO_3$ (A=Ba, Ca, and Sr) as well as Ca-doped $BiFeO_3$ [5, 48-50]. The mechanism of this type of switching is not well-understood, but it is clear that filamentary conduction is different from unipolar and bipolar switching, since these types of RS are highly dependent on a reset voltage with different or same polarity required to return to HRS.

Recently, Ca-doped $BiFeO_3$ was reported to be the first bulk material to show RS [5]. As a function of applied field, the total conductivity (bulk and grain boundary) of Ca-doped $BiFeO_3$ increased slightly with increasing applied field until it reached an onset field at which the conductivity increased sharply by ~ three orders of magnitude and then achieved almost constant values even with increasing applied field. On decreasing the applied voltage, the high conductivity state was maintained, with larger hysteresis, until a sudden return to the original conductivity occurred at a transition field [Transition voltage (E_t) is the field at which the sample conductivity returns to its original state], Figure 2.17 (a, b). RS behaviour in Ca-doped $BiFeO_3$ occurred at room temperature and is not influenced by the electrode type or different pO_2.

The sharp increase in the conductivity of Ca-doped BF comes from the large increase in carrier concentration (holes). It is not associated with a ferroelectric effect because the ferroelectricity of BF based on the rhombohedral distorted perovskite structure with a tolerance factor of 0.88, causing the oxygen octahedra to tilt to fit into the cell and the FeO_6 octahedra to rotate antiphase [51, 52], but $Ca_xBi_{1-x}FeO_3$ with x=0.2-0.6 has a cubic structure (centrosymmetric), therefore eliminating the ferroelectric behaviour [53, 54].

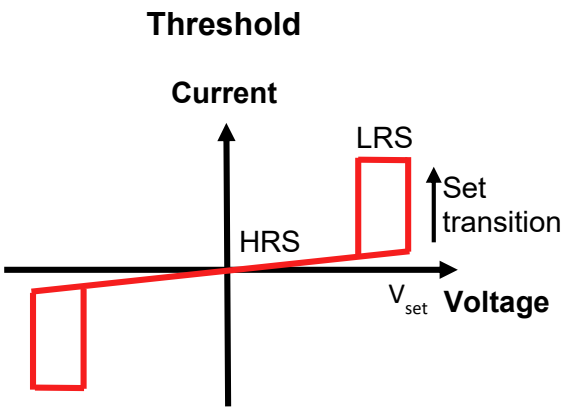

Figure 2.16 Current-voltage curve for threshold switching in which the set transition from the high resistance state, HRS, to the low resistance state, LRS, occurs at the positive voltage, V_{set}, wheare the switching from the low resistance state, LRS, to the high resistance state, HRS, occurs at lower positive voltage, V_{reset}.

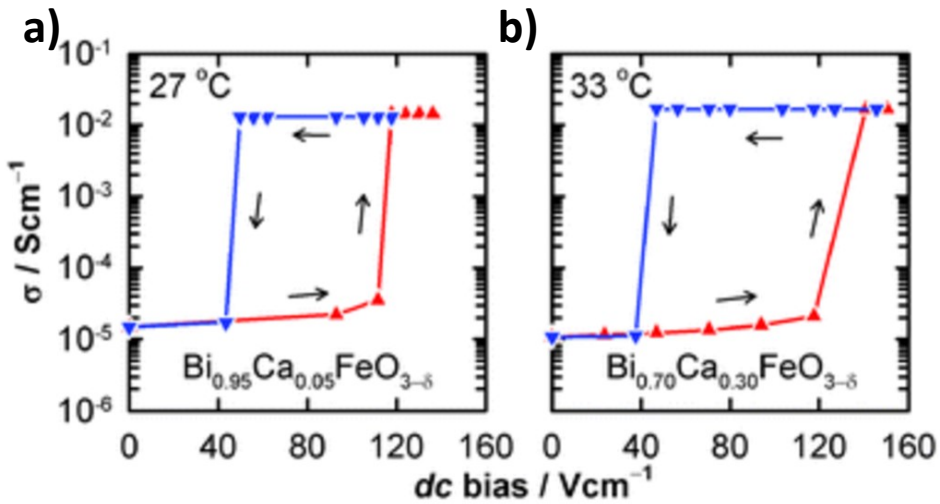

Figure 2.17 The total conductivity against applied field for a) $Ca_{0.05}Bi_{0.95}FeO_{3-\delta}$ b) $Ca_{0.3}Bi_{0.7}FeO_{3-\delta}$ [5].

2.4 The effect of dc bias on the conductivity

The effect of a small dc bias on the electrical properties of materials is not a common area of investigation in the chemistry and physics of solids, but in recent years it has come more frequently to attention in many emerging areas. During typical impedance spectroscopy measurements, the applied ac voltage is usually 10 to 100 mV, which does not change the sample, but when applying a dc voltage, the sample may change.

Several examples have been found in which the electrical conductivity of a material alters (decreases or increases) as a result of a small dc bias application. This effect is usually recoverable on the removal of the dc bias. In some materials, the effects occur at room temperature, as with Ca-doped $BiFeO_3$ (discussed above), but in yttria-stabilized zirconia (YSZ) and a range of acceptor-doped titanates, the effects occur at a high temperature. No effect is usually observed in un-doped materials.

In $Zr_{1-x}Y_xO_{2-x/2}$, a reversible increase in bulk and grain boundary conductivity appeared with increasing applied dc voltage (1 to 15 V) at high temperatures [2]. Along with this enhancement in conductivity, the spike at the sample–electrode interface collapsed, meaning that there is electronic conduction in YSZ during the small dc bias application, Figure 2.18. Another example showing voltage-dependent electronic conductivity is $BaTi_{1-x}\ Mg_xO_{3-x}$ in which the conductivity increased by 1–2 orders of magnitude as a response to a small dc bias application (1–50 V/cm) [48]. The temperature and the magnitude of applied voltage played a big role in the magnitude of change in conductivity and time to reach a steady state, Figure 2.19.

The general mechanism for the effect of applied dc voltage on the electrical conductivity appears to be that electrons are removed from the sample and trapped at the surface [55]. On the application of dc bias, the equilibria between oxygen species are modified at the sample–anode interface according to the following:

$$O_2(g) \leftrightarrow O_2(ads) \overset{e-}{\leftrightarrow} O_2^- \overset{e-}{\leftrightarrow} O_2^{2-} \,/\, 2O^- \overset{e-}{\leftrightarrow} 2O^{2-}(surface) \leftrightarrow 2O^{2-}(bulk) \quad 2.11$$

Because the charge carriers in p-type conductivity are holes and there are no cations that can be easily ionized, it is believed that the enhancement of the conductivity is correlated with the ionization of underbonded oxygen (located near the surface and dopant cation) [2, 48]. The ionised electron goes to the sample–anode interface leading to the formation of

ionised oxygen species (peroxide or superoxide ions and the produced holes remain as lattice O^- ions, i.e. $O_O^{\bullet}$:

$$O_O^x \rightarrow O_O^{\bullet} + e^- \qquad 2.12$$

As a consequence, when the applied field is increased, the number of holes increases, leading to an increase in the charge carrier concentration. This enhances the p-type conductivity of these materials.

$$O_2 \rightarrow 2O^{2-} + 4h \qquad 2.13$$

In contrast, the charge carriers of n-type materials are electrons and with a dc bias application, electrons are removed from the sample interior and trapped at the sample–anode interface by participating in equilibria shown in equation 2.1.4a. Hence, the concentration of the charge carrier is reduced (equation 2.1.4d), which produces a decrease in n-type conductivity.

$$4e + O_2 \rightarrow 2O^{2-} \qquad 2.14$$

After removal of the dc bias application, the electronic conductivities of both p-type and n-type materials are fully recoverable to the original state.

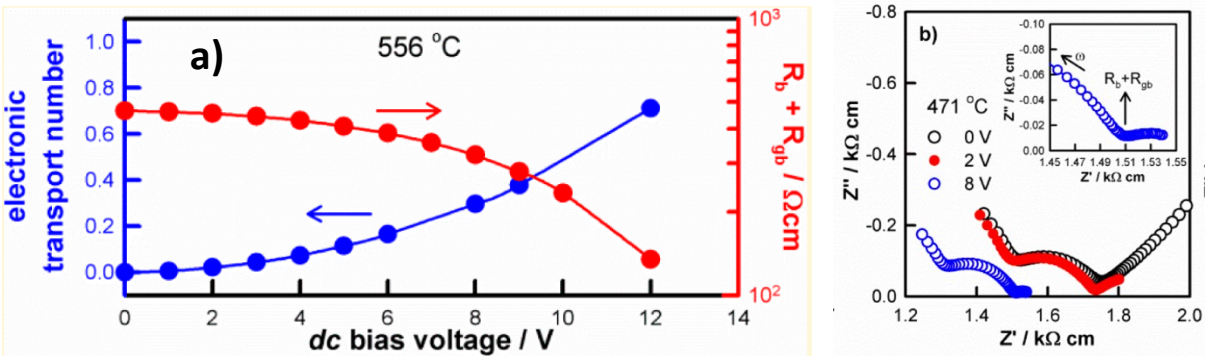

Figure 2.18 Impedance data for YSZ08 a). Resistance and electronic transport number as a function of applied dc bias voltage b). Impedance complex plane plot at 471 °C before and after applying a voltage [2].

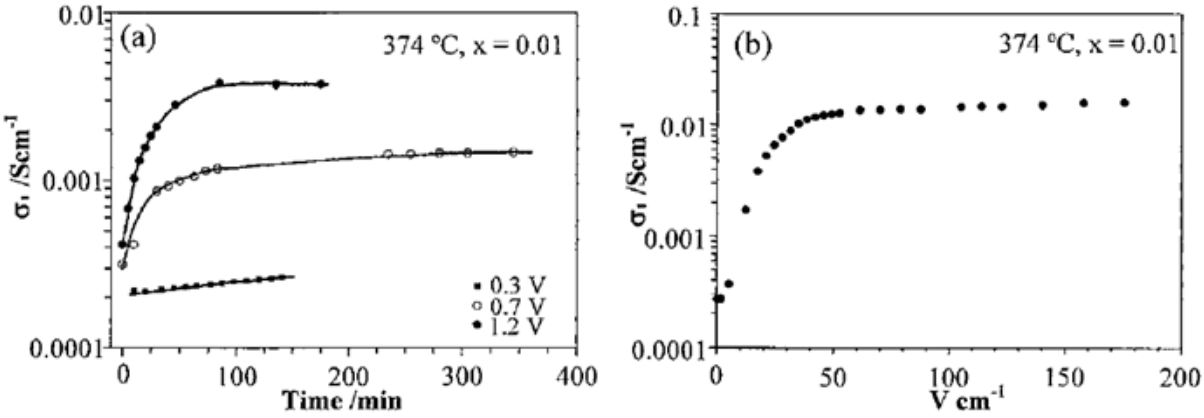

Figure 2.19 Bulk conductivity of $BaTi_{1-x}Mg_xO_{3-x}$ (x=0.01) as a function of a). time and b). voltage of 0.3, 0.7 and 1.2 V at 374 °C [48].

2.5 Hafnium oxide (HfO_2):

Hafnium (Hf) was discovered in 1869. Its chemical properties remained a mystery until 1922, when Coster and Hevesy verified their prediction that Hf might be similar to zirconium in terms of chemistry. They used Bohr's theories of atomic structure and spectroscopic examinations of both elements to demonstrate that hafnium is identical to zirconium in that they have two outer shell electrons in their elemental state, (Hf [Xe] $4f^{14}$ $5d^2$ $6s^2$) (Zr [Kr] $4d^2$ $5s^2$). This means that hafnium has similar chemical behaviour to zirconium despite their differences in atomic weight and density [56, 57].

Hafnium oxide (HfO_2) has a number of a good properties for use in the following applications: for memory devices and for fuel cells. These properties include high melting point, high bulk modulus, high chemical stability and high neutron absorption [58]. Hafnium oxide also a has high dielectric constant (30), high enthalpy of formation (271 kcal/mole) and a large band gap (5.68 eV) [59, 60]] in thin film materials. Doped Hafnia is an oxide ion conducting material, similar in terms of structure and polymorphism to ZrO_2 [61].

2.5.1 Structure of hafnium oxide:

In bulk ceramics, hafnium oxide has three main polymorphs: cubic, tetragonal and monoclinic which are listed in Table 2.2 and shown in Figure 2.26. At room temperature, hafnium oxide has a monoclinic crystal structure with a=5.1156 Å, b=5.7122 Å, c=5.2948 Å, and β=99°. The structure can be considered as a distorted cubic structure [62]. Hafnia undergoes

transformation from the monoclinic to tetragonal phase along with a change in lattice constants at 1920 °C. The tetragonal lattice parameters are *a*=*b*=5.14 Å, *c*=5.25 Å. Finally, at higher temperature, the formation of a cubic fluorite structure has been reported to occur at around 2700-2750 °C [62]. These three phases of hafnia are presented in Figure 2.26. In the cubic fluorite crystal structure, hafnium occupies the corners and faces and oxygen occupies all tetrahedral sites.

Table 2.2 The three crystal systems of HfO_2 [8, 63, 64].

Crystal system	Unit cell shape	Essential symmetry	Allowed lattice
Cubic	$a = b = c$, $\alpha = \beta = \gamma = 90°$	Four threefold axes	P, F, I
Tetragonal	$a = b \neq c$, $\alpha = \beta = \gamma = 90°$	One fourfold axis	P, I
Monoclinic	$a \neq b \neq c$, $\alpha = \gamma = 90°$, $\beta \neq 90°$	One twofold axis or mirror plane	P

2.5.2 Doped hafnia

Hafnium oxide has been doped by different elements to enhance certain properties. Ionic conductivity is one of these properties that can be enhanced through doping and allows hafnium oxide to be a good oxide ion conductor for electrolyte materials in various applications. Ferroelectricity also is obtained in thin films of doped hafnium oxide. The thin layer of doped hafnium oxide has become an attractive material for memory applications since they have a remanent polarisation of ~10-45 $\mu C/cm^2$, a coercive field of ~ 1-2 MV/cm [65, 66], and good memory characteristics such as fast switching speed, low power consumption and a good CMOS operation compatibility [67]. These features of ferroelectric doped HfO_2 can compete with the most common perovskite ferroelectrics such as $Pb(Zr_xTi_{1-x})O_3$ (PZT) that has a remanent polarization of 20-40 $\mu C/cm^2$, and a coercive field of ~50 kV/cm. It should be noted that PZT has some drawbacks in terms of compatibility in CMOS,

processing control and scalability [68]. In contrast doped HfO_2 shows CMOS-compatibility with a high scalability that allows HfO_2 thin films to be used in many memory applications including nanoscale ferroelectric devices [66, 69].

Oxide ion conductivity of doped hafnia

Hafnia solid solutions are less well-studied because of their similarity to Zirconia as mentioned previously. Hafnium oxide has a relatively high cost which excludes it from consideration for many practical applications [70]. Hafnia has a monoclinic structure, but is assumed to a have a cubic fluorite structure when doped with aliovalent ions (e.g., Y^{3+}, Sc^{3+}, Ca^{2+}, $Mg^{2+}$and the rare-earth elements) [70, 71].

In hafnia, the cation site is the only possible position of doping. Trubelja et al. [61] studied the ionic conductivity of hafnium oxide doped with rare earth elements (R^{3+}). They reported that the ionic conductivity of (R^{3+})-doped hafnia decreased with an increase in the activation energy when the radius of dopant ions increased except for holmium-doped hafnia, showing a lower conductivity than hafnium oxide doped with yttrium (see Figure 2.20 and Figure 2.21) [70]. The lattice parameters of Ho^{3+} and Y^{3+}-doped hafnia are 0.5128 nm and 0.5126 nm, respectively. So, the relative radius of the Ho^{3+} ion in fluorite cubic structure is slightly larger than Y^{3+} ionic radius. This could be the reason why HfO_2-Ho_2O_3 has a lower level of conductivity than HfO_2-Y_2O_3 [70]. The ionic conductivity of HfO_2-Sc_2O_3 was the highest among other systems at a dopant concentration of 14 mol%, see Figure 2.22 (A). The dopant concentration of 10 mol% was shown to have the optimum ionic conductivity in the systems HfO_2-Yb_2O_3, HfO_2-Sm_2O_3 and HfO_2-Y_2O_3. A higher concentration of dopants can cause deep vacancy trapping that reduces the ionic conductivity. According to the literature when doped HfO_2 and ZrO_2 systems are compared, the ionic conductivity of doped hafnia is found to be 1.5 to 2.3 times lower than doped zirconia systems, as shown in Figure 2.23.

In another study, Johansen and Cleary [72] measured the electrical conductivity of $Hf_{1-x}Ca_xO_{2-X}$ between 800 and 2000 °C. The differences in conductivity are small in the range x=0.08, to 0.17, but the maximum conductivity was reported at ~12 mol% of CaO-doped hafnia.

Schielts [73] studied the Ionic conductivity of fluorite-phase HfO_2, that is doped with 6 to 20 mol% of Y_2O_3. Yttria-stabilized hafnia of 8 mol% Y_2O_3 had higher conductivity than other compositions. In addition, all compositions of $Hf_{1-x}Y_xO_{2-x/2}$ showed oxide ion

conductivity at high temperatures [73]. Despite HfO_2- 6 mol% Y_2O_3, the total conductivity of all compositions of yttria-stabilized hafnia decreased and the activation energies increased as the Y_2O_3 content increased (see Figure 2.24 and Figure 2.25). This decrease in the conductivity is attributed to the aggregation of oxygen vacancies with dopant cations or cations as described in the effect of Y^{3+} concentration on the conductivity of YSZ section [8, 16, 74].

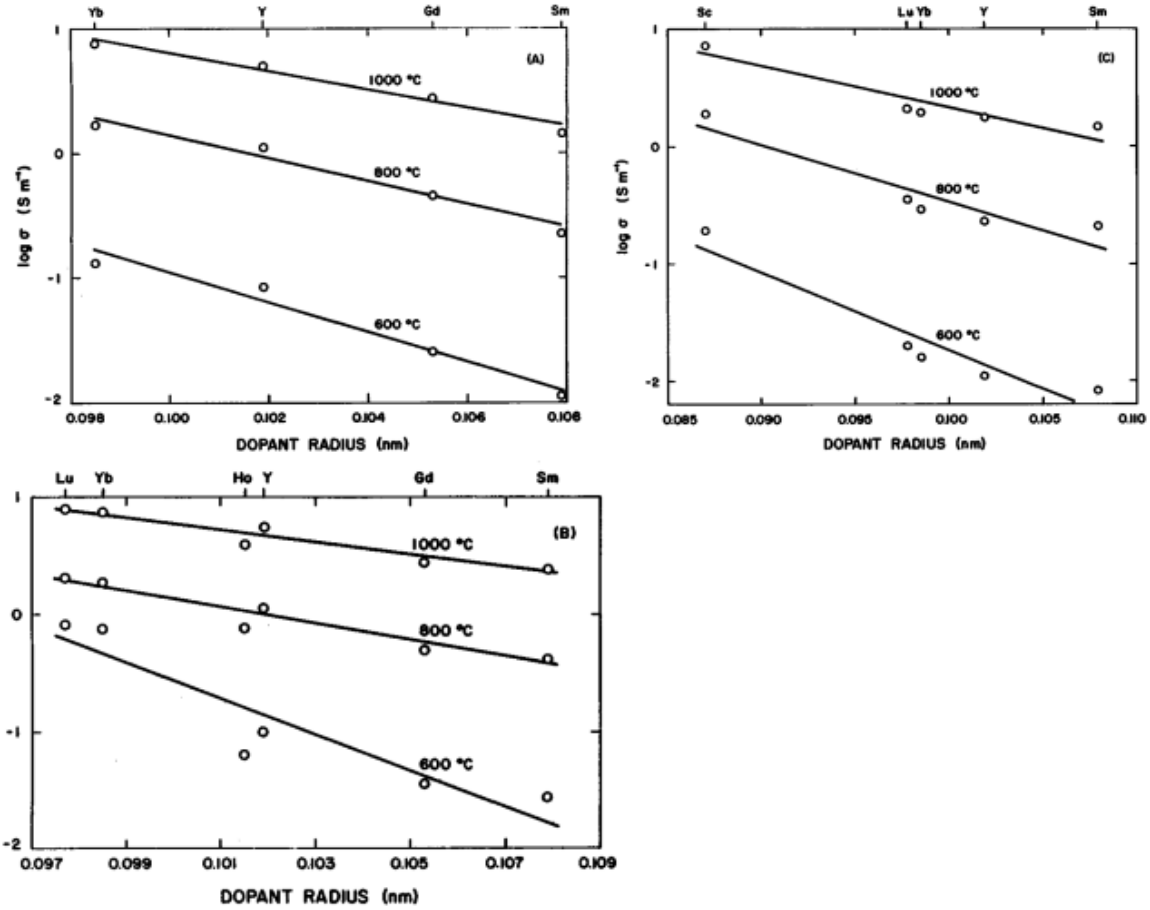

Figure 2.20 The ionic conductivity of R^{3+} ions doped into hafnium oxide as a function of dopant ionic radius [61].

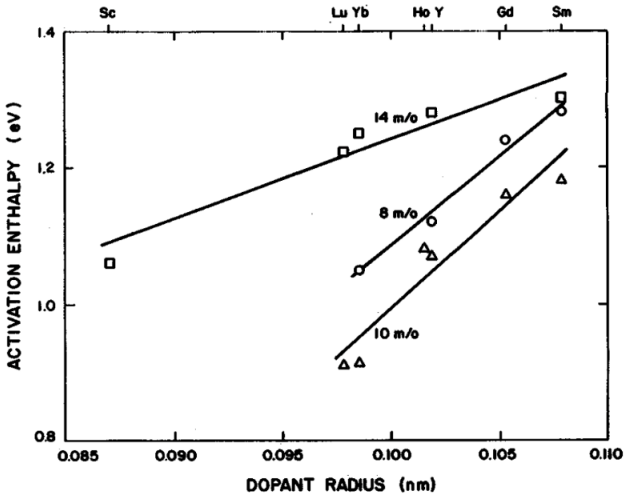

Figure 2.21 The activation energy of hafnia doped with R^{3+} ions as a function of dopant ionic radius. The percentages of dopant concentration are 8, 10, and 14 mol% [61].

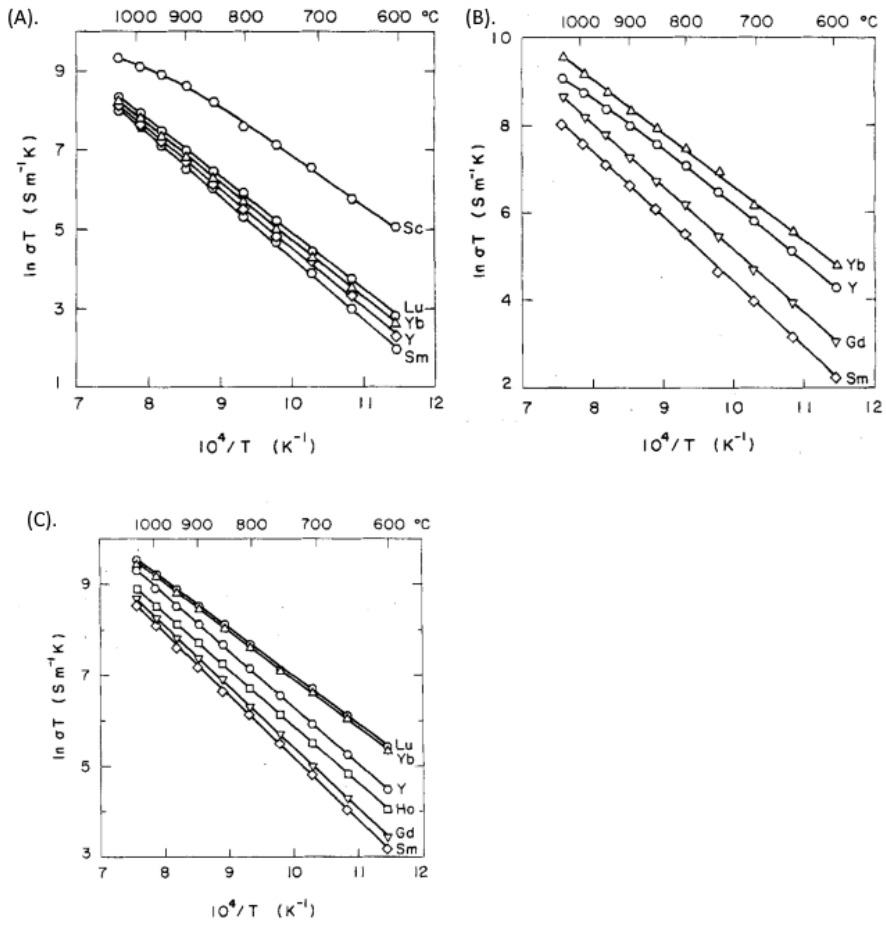

Figure 2.22 The Ionic conductivity of hafnia doped with R^{3+} ions as a function of temperature. The percentage of dopant concentration are: (A) 14, (B) 8, and (C) 10 mol% [61].

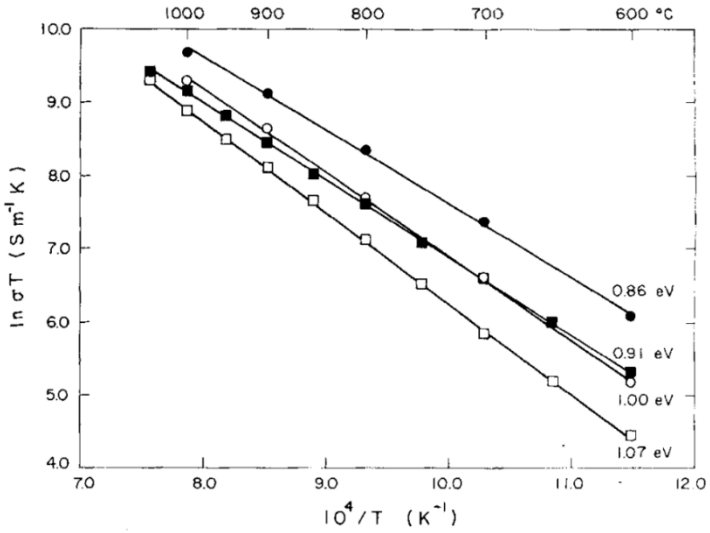

Figure 2.23 Arrhenius plot of doped HfO_2 and ZrO_2: $Zr0_2$-10 mol% Yb_2O_3 (solid circle), ZrO_2-10 mol% Y_2O_3 (open circle), Hf02-10 mol% Yb_20_3 (solid square), HfO_2-10 mol% Y_20_3 (open square) [61].

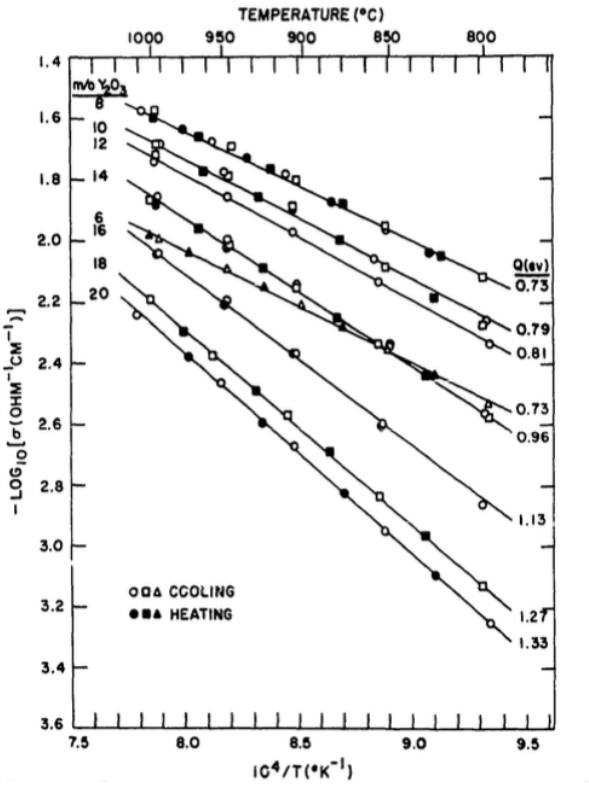

Figure 2.24 The total conductivity of yttria-stabilised hafnia for different compositions [73].

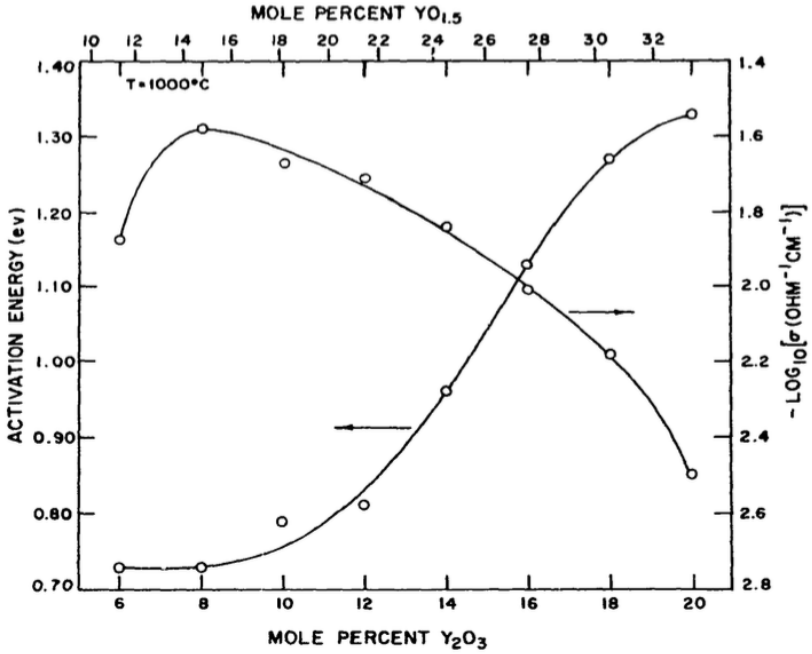

Figure 2.25 The activation energy and conductivity value of $Hf_{1-x}Y_xO_{2-x/2}$ at 1000 °C [73].

Ferroelectric behaviour of hafnium oxide thin films

Fluorite structure materials such as doped HfO_2 have remarkably changed the developmental status of ferroelectric semiconductor devices e.g. ferroelectric capacitors. In 2011 and in

NaMLab, Böscke et al. [4] were the first to report ferroelectric behaviour in Si doped HfO_2 thin films. They succeeded to stabilize an orthorhombic phase of doped hafnia under the effect of mechanical stress with a good a remanent polarization of 10 $\mu C/cm^2$. Subsequently, several elements have been doped into HfO_2 by different preparation methods, Table 2.3, to understand the material behaviour.

The monoclinic, tetragonal and cubic fluorite structure of pure and doped hafnia have been well studied, they are centrosymmetric and do not show any ferroelectric behaviour, Figure 2.26. However, Ferroelectricity is clearly associated with the polar (non-centrosymmetric) orthorhombic phase that has been formed in doped hafnia thin films, Figure 2.26. The orthorhombic phase is metastable at the boundary between tetragonal and monoclinic phases and is formed by distortion of the tetragonal phase via the effect of various factors i.e. dopants, annealing treatment, deposition method, growth temperature and strain impact. These factors play a critical role in lowering the kinetic barrier of the T-M transition, resulting in stabilization of the orthorhombic phase in doped hafnia thin films [75, 76].

Ferroelectric $Hf_{1-x}Zr_xO_2$ thin films

There are many ferroelectric hafnia systems, but HfO_2-ZrO_2 solid solutions, prepared by atomic layer deposition, ALD, is the system that has been intensively studied. This is because $Hf_{1-x}Zr_xO_2$ solid solutions show ferroelectricity in a wide range of chemical composition (x=0.3-0.8) with a large remanent polarization at x=0.5, Figure 2.27b [75, 77]. As in many doped-hafnia thin films, materials are generally deposited at low temperature and then crystallise at high temperature. $Hf_{1-x}Zr_xO_2$ ferroelectric was the preferable choice because it shows stable ferroelectric properties at lower crystallisation temperature under N_2 gas. Also, $Hf_{0.5}Zr_{0.5}O_2$ thin films show robust ferroelectricity at very low thickness (< 10 nm) which is compatible for applications such as ferroelectric random-access memory.

The right oxygen concentration of $Hf_{0.5}Zr_{0.5}O_2$ is important to optimize device performance. Mittmann et al. [78] reported the impact of changing ozone dose time during ALD deposition and they showed that oxygen concentration greatly changes the ferroelectric properties of $Hf_{0.5}Zr_{0.5}O_2$. With increasing ozone dose time, the phase transition of $Hf_{0.5}Zr_{0.5}O_2$ can occur from paraelectric tetragonal to ferroelectric orthorhombic and from ferroelectric orthorhombic to paraelectric monoclinic structures [78]. It was found that the remanent polarization of $Hf_{0.5}Zr_{0.5}O_2$ increased and reached the optimum at 1 second of ozone dose

time, Figure 2.27.

Table 2.3 The composition, crystal structure and preparation method of ferroelectric doped HfO_2 films.

Film Composition	Crystal structure	Deposition technique	Reference
9-20 cation% -La:HfO_2 4.4 cation% of Al:HfO_2 $Hf_{0.5}Zr_{0.5}O_2$	Orthorhombic phase	Atomic layer deposition (ALD)	[77, 79, 80]
$0.07YO_{1.5}$-$0.93HfO_2$ 4.4 cation% of Si:HfO_2	Orthorhombic phase	Pulsed laser deposition (PLD)	[76, 81-83]
$Hf_{0.5}Zr_{0.5}O_2$	Orthorhombic phase	Metal-organic chemical vapour deposition (MOCVD)	[84-86]
$Hf_{0.5}Zr_{0.5}O_2$ 1.5 cation% of Y:HfO_2	Orthorhombic phase	Sputtering	[87, 88]
$Hf_{0.5}Zr_{0.5}O_2$ 5.2 cation% of Y:HfO_2	Orthorhombic phase Cubic phase	Chemical solution deposition (CSD)	[89, 90]

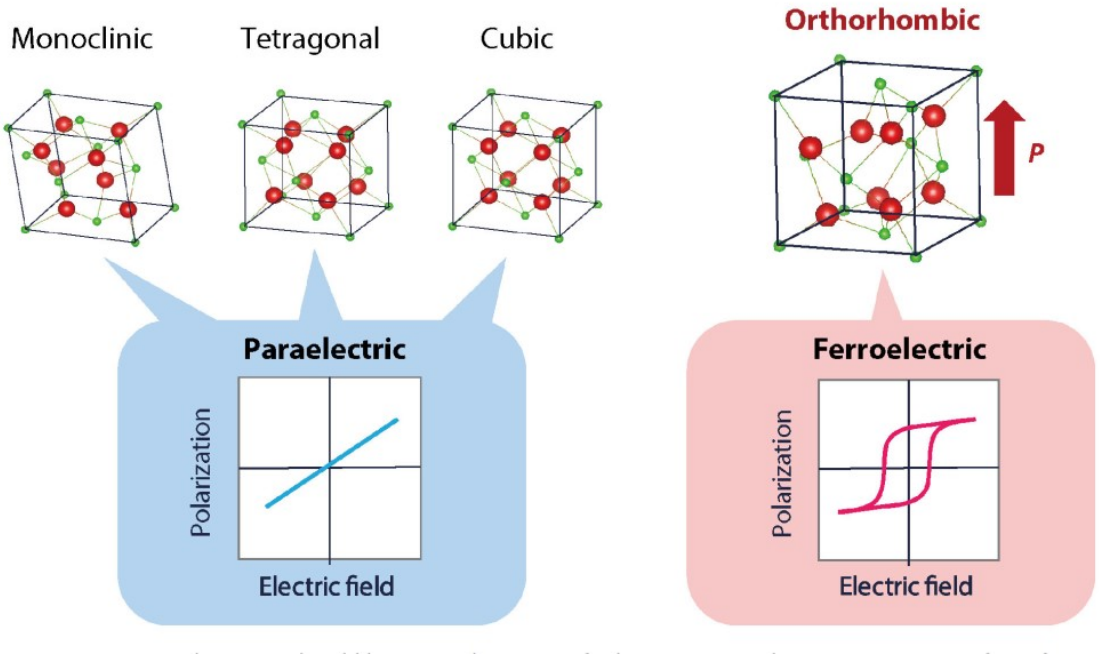

Figure 2.26 Structures of the four HfO_2 polymorphs (The red circles represent hafnium and the green circles represent oxygen). Ferroelectricity only exists in a metastable orthorhombic phase [26].

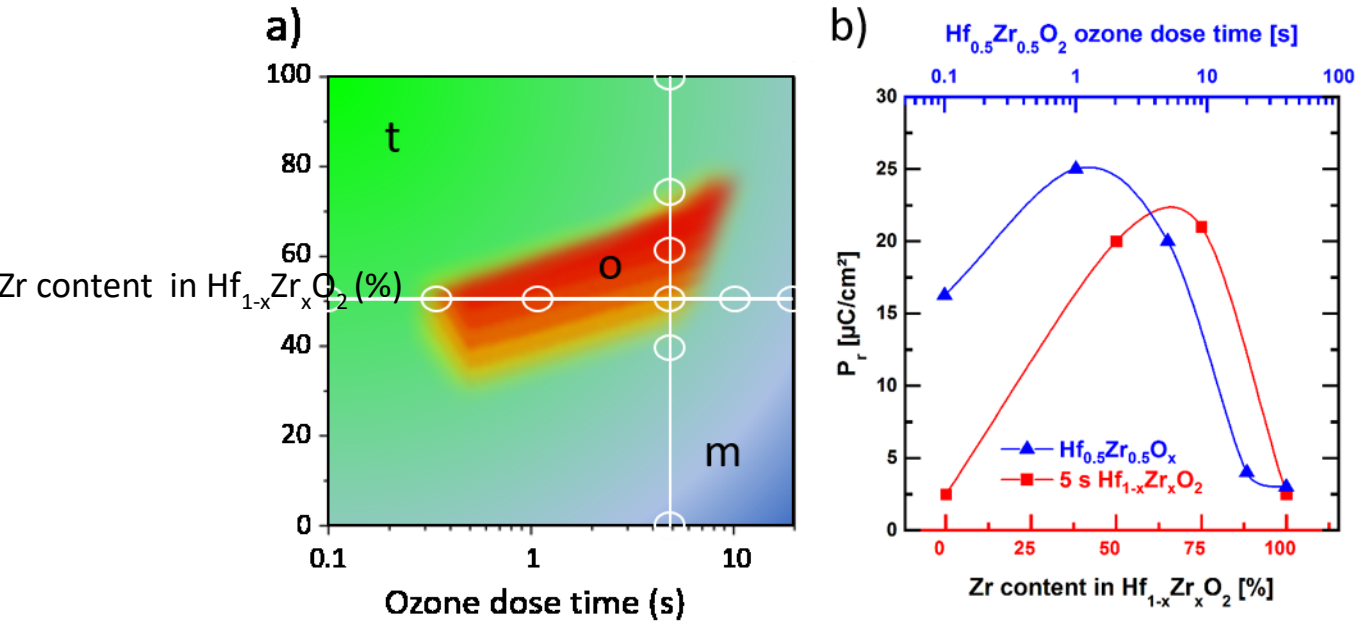

Figure 2.27 a) Illustrated diagram of structural phases of HfO_2 as a function of Zr content and exposure of ozone dose time. The green region represents samples with tetragonal (t) phase, red region represent samples with high orthorhombic (o) phase portion, and blue region represents samples with monoclinic (m) phase. b) Remanent polarization of two samples, blue triangle shows remanent polarization of $Hf_{0.5}Zr_{0.5}O_2$ against the effect of ozone dose time, red square shows remanent polarization of $Hf_{1-x}Zr_xO_2$ with 5 s O_3 dose time as a function of increasing Zr content [78, 91].

Questions remaining about Ferroelectric doped HfO_2

I. Wake up and fatigue effect

Beside the advantages of hafnia ferroelectric thin films, there are some critical issues (wake up and fatigue effect) that need to be understood in order to improve the performance of HfO_2 devices.

The first issue is related to the enhancement of remanent polarization and formation of P-E hysteresis loops of thin films of doped hafnia as a result of increasing number of cycles, Figure 2.28 and Figure 2.29. There are two possible mechanisms of this wake up effect. First, a high number of oxygen vacancies can be located near the electrodes, leading to asymmetric distribution. During the application of electric field cycles, oxygen vacancies can diffuse homogenously in the bulk region of HfO_2-ferroelectic thin films. This homogenous distribution of oxygen vacancies can enhance the ferroelectric properties (an increase in P_r and formation of hysteresis loop) of HfO_2 thin films. Second, another mechanism is simply associated with a field-cycling induced structural transition from a non-ferroelectric phase to a ferroelectric (o) phase [65, 90, 92].

The second issue is the limited lifetime of ferroelectric hafnia during the field-cycling process. The observed fatigue is expected to be attributed to aggregation of defects such as oxygen vacancies. These defects can form a conductive pathway between top and bottom electrodes, resulting in reduction of remanent polarization and then loss of the ferroelectric properties. Another possible reason for fatigue is related to the structural phase transition from ferroelectric (o) to non-ferroelectric (m) phase as a response to field-cycling of doped hafnia thin films [65, 78, 92]. This clearly can be the following step after the wake up effect, Figure 2.28.

II. Permittivity

Permittivity is an essential characteristic of ferroelectric materials. It basically shows how much the material is able to store electric charge. The three common polymorphs of HfO_2 (monoclinic, tetragonal and cubic) have permittivity values of 16, 70, and 29, respectively. Interestingly, the ferroelectric (orthorhombic) phase of HfO_2 thin films show a permittivity of ~30 ,Table 2.4, which is much lower than that of conventional ferroelectrics such as $BaTiO_3$ or PZT. The permittivity of ferroelectrics is modifiable, but usually is high, particularly close to the phase transition point such as $BaTiO_3$ or PZT. By temperature-dependent X-ray diffraction experiments, the Curie temperature (T_c) of ferroelectric doped HfO_2 is ~460 °C.

Therefore, there are many questions about the reason why ferroelectric hafnias thin films have lower permittivity: does the permittivity increase with the application of electric field, what is the permittivity of ferroelectric hafnia thin films at T_c? These questions need to be answered in order to advance the use of doped hafnia thin films as a proper ferroelectric material.

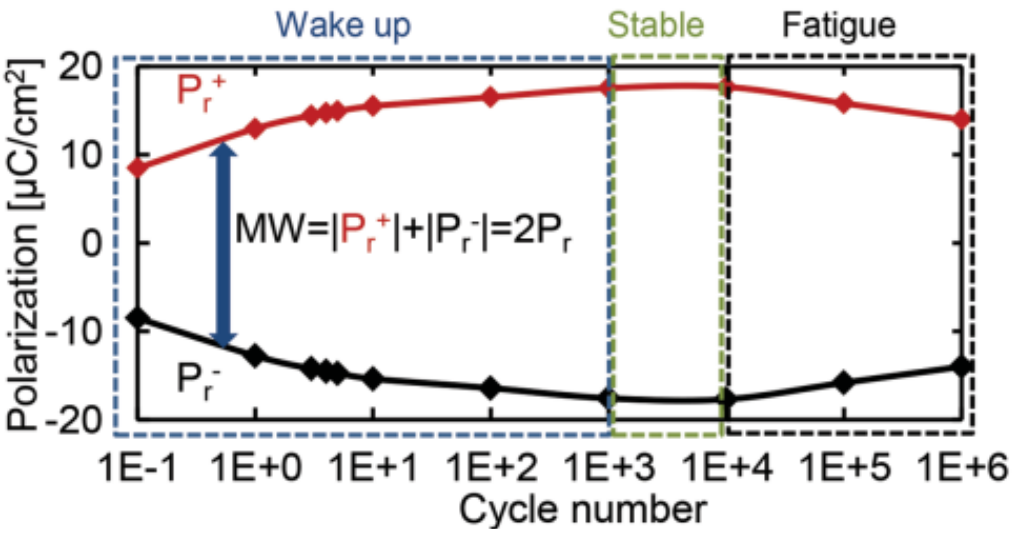

Figure 2.28 The remanent polarization response of Sr:HfO_2 over the number of applied field cycles [92].

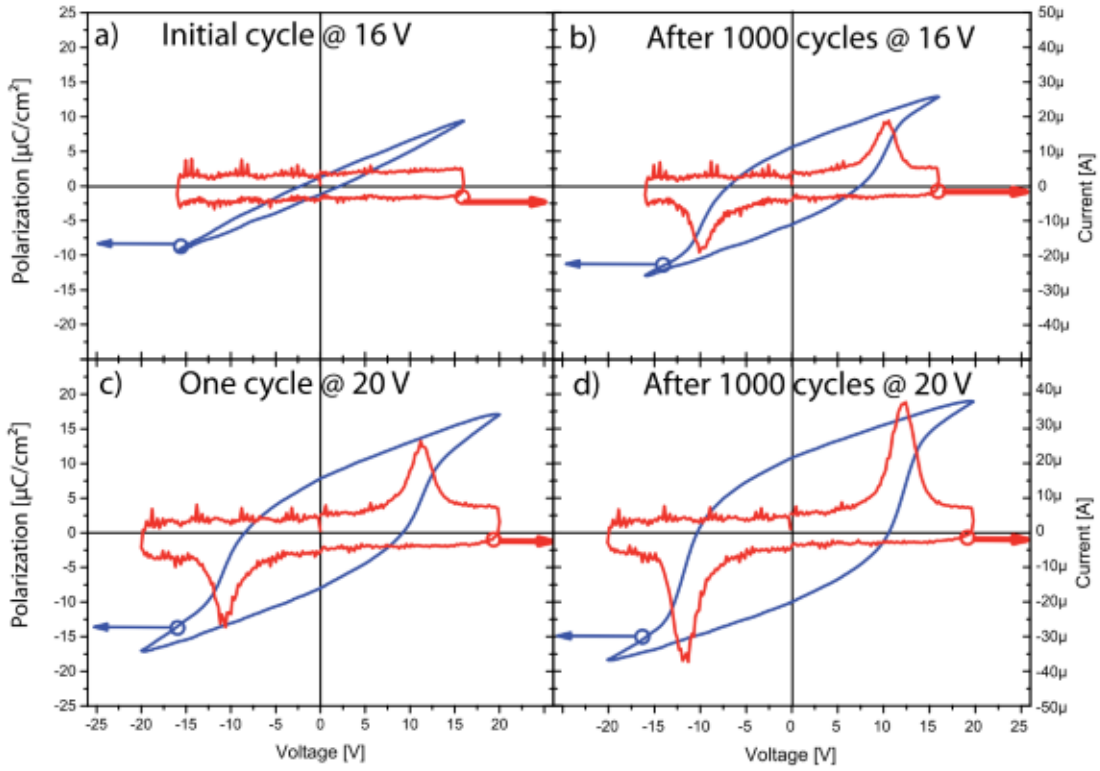

Figure 2.29 The wake up (cycles) effects on HfO_2:Y (5.2 Cat.% of yttrium) with a thickness=56 nm [90].

Table 2.4 Permittivity values of ferroelectric doped HfO_2 films.

Composition	Dielectric permittivity
M-HfO_2 [93].	16
T-HfO_2 [93].	70
C-HfO_2 [93].	29
Ferr-HfO_2 [94].	30
$Hf_{0.14}Zr_{0.86}O_2$ [95].	31.8

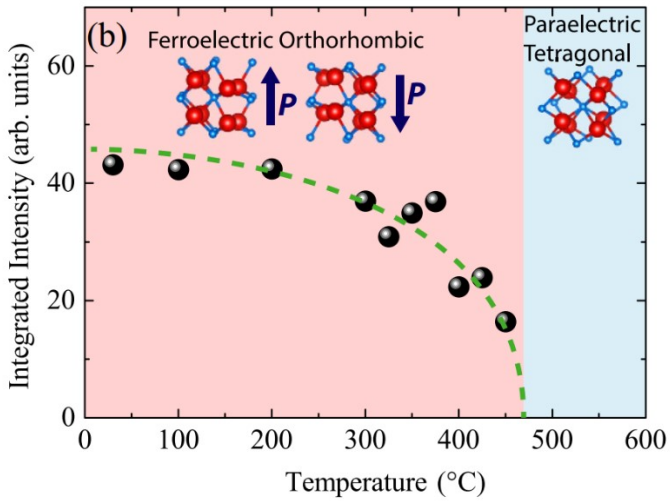

Figure 2.30 Integrated intensity of X-ray diffraction peak of Y-doped HfO_2 as a function of temperature [26].

2.6 References

1. Jovaní, M., H.c. Beltrán-Mir, E. Cordoncillo, and A.R. West, *Atmosphere-and Voltage-Dependent Electronic Conductivity of Oxide-Ion-Conducting $Zr_{1-x}Y_xO_{2-x/2}$ Ceramics.* Inorganic chemistry, 2017. **56**(12): p. 7081-7088.
2. Masó, N. and A.R. West, *Electronic conductivity in yttria-stabilized zirconia under a small dc bias.* Chemistry of Materials, 2015. **27**(5): p. 1552-1558.
3. Vendrell, X. and A.R. West, *Induced p-type semiconductivity in yttria-stabilized zirconia.* Journal of the American Ceramic Society, 2019. **102**(10): p. 6100-6106.
4. Böscke, T., J. Müller, D. Bräuhaus, U. Schröder, and U. Böttger, *Ferroelectricity in hafnium oxide thin films.* Applied physics letters, 2011. **99**(10): p. 102903.
5. Masó, N., H. Beltrán, M. Prades, E. Cordoncillo, and A.R. West, *Field-enhanced bulk conductivity and resistive-switching in Ca-doped BiFeO 3 ceramics.* Physical Chemistry Chemical Physics, 2014. **16**(36): p. 19408-19416.
6. Steele, B.C. and A. Heinzel, *Materials for fuel-cell technologies*, in *Materials For Sustainable Energy: A Collection of Peer-Reviewed Research and Review Articles from Nature Publishing Group*. 2011, World Scientific. p. 224-231.
7. Wachsman, E.D. and K.T. Lee, *Lowering the temperature of solid oxide fuel cells.* Science, 2011. **334**(6058): p. 935-939.
8. West, A.R., *Solid state chemistry and its applications*. 2014: John Wiley & Sons.

9. Koteswararao, P., M.B. Suresh, B. Wanic, P.B. Rao, and P. Varalakshimi, *Review on Ceramics for Solid Oxide Fuel Cells.* 2017.
10. Hagenmuller, P. and W. Van Gool, *Solid electrolytes: general principles, characterization, materials, applications*. 2015: Elsevier.
11. Etsell, T. and S.N. Flengas, *Electrical properties of solid oxide electrolytes.* Chemical Reviews, 1970. **70**(3): p. 339-376.
12. Takahashi, T. and H. Iwahara, *Ionic conduction in perovskite-type oxide solid solution and its application to the solid electrolyte fuel cell.* Energy Conversion, 1971. **11**(3): p. 105-111.
13. Kim, J.-H. and H.-I. Yoo, *Partial electronic conductivity and electrolytic domain of* $La_{0.9}Sr_{0.1}Ga_{0.8}Mg_{0.2}O_{3-\delta}$. Solid State Ionics, 2001. **140**(1-2): p. 105-113.
14. Benenson, R., W. Roth, W. Gibson, B. Daudin, M. Dubus, C.C. Jones, and H. Guggenheim, *Investigation of the phase transition in lead fluoride by proton channeling.* Physical Review B, 1991. **44**(13): p. 6663.
15. Goodenough, J.B., *Ceramic technology: Oxide-ion conductors by design.* Nature, 2000. **404**(6780): p. 821.
16. Kharton, V., F. Marques, and A. Atkinson, *Transport properties of solid oxide electrolyte ceramics: a brief review.* Solid State Ionics, 2004. **174**(1-4): p. 135-149.
17. Norberg, S.T., S. Hull, I. Ahmed, S.G. Eriksson, D. Marrocchelli, P.A. Madden, P. Li, and J.T. Irvine, *Structural Disorder in Doped Zirconias, Part I: The* $Zr_{0.8}Sc_{0.2-x}Y_xO_{1.9}$ *(*$0.0 \leq x \leq 0.2$*) System.* Chemistry of Materials, 2011. **23**(6): p. 1356-1364.
18. Badwal, S., F. Ciacchi, and D. Milosevic, *Scandia–zirconia electrolytes for intermediate temperature solid oxide fuel cell operation.* Solid State Ionics, 2000. **136**: p. 91-99.
19. Yao, Z., *Solid State Electrochemistry Peter G. Bruce.* Materials and Manufacturing Processes, 1998. **13**(3): p. 475-476.
20. Singhal, S.C., *Advances in solid oxide fuel cell technology.* Solid State Ionics, 2000. **135**(1): p. 305-313.
21. Gao, W. and N.M. Sammes, *An introduction to electronic and ionic materials*. 1999: World Scientific Publishing Company.
22. Damjanovic, D., *Ferroelectric, dielectric and piezoelectric properties of ferroelectric thin films and ceramics.* Reports on Progress in Physics, 1998. **61**(9): p. 1267.
23. Tilley, R.J., *Understanding solids: the science of materials*. 2004: John Wiley & Sons.

24. Scott, J., *Ferroelectrics go bananas.* Journal of Physics: Condensed Matter, 2007. **20**(2): p. 021001.
25. Dawber, M., K. Rabe, and J. Scott, *Physics of thin-film ferroelectric oxides.* Reviews of modern physics, 2005. **77**(4): p. 1083.
26. Shimizu, T., *Ferroelectricity in HfO2 and related ferroelectrics.* Journal of the Ceramic Society of Japan, 2018. **126**(9): p. 667-674.
27. Acosta, E., *Thin films/properties and applications*, in *Thin Films*. 2021, IntechOpen.
28. Şimşek, B., Ö.B. Ceran, and O.N. Şara, *Difficulties in thin film synthesis.* Handbook of Nanomaterials and Nanocomposites for Energy and Environmental Applications, 2021: p. 251-273.
29. Chapman, B., *Thin-film adhesion.* Journal of Vacuum Science and Technology, 1974. **11**(1): p. 106-113.
30. Elers, K.E., T. Blomberg, M. Peussa, B. Aitchison, S. Haukka, and S. Marcus, *Film uniformity in atomic layer deposition.* Chemical Vapor Deposition, 2006. **12**(1): p. 13-24.
31. Desu, S., *Stress induced modifications in ferroelectric films.* physica status solidi (a), 1994. **141**(1): p. 119-133.
32. Desu, S.B., *Influence of stresses on the properties of ferroelectric $BaTiO_3$ thin films.* Journal of The Electrochemical Society, 1993. **140**(10): p. 2981-2987.
33. Huang, G. and S. Berger, *Combined effect of thickness and stress on ferroelectric behavior of thin $BaTiO_3$ films.* Journal of Applied Physics, 2003. **93**(5): p. 2855-2860.
34. Bartasyte, A., *Stress effects and phase transitions in $PbTiO_3$ thin films deposited by MOCVD*. 2007, Institut National Polytechnique de Grenoble.
35. Lee, J.S., S. Lee, and T.W. Noh, *Resistive switching phenomena: A review of statistical physics approaches.* Applied Physics Reviews, 2015. **2**(3): p. 031303.
36. Wang, Z., H. Wu, G.W. Burr, C.S. Hwang, K.L. Wang, Q. Xia, and J.J. Yang, *Resistive switching materials for information processing.* Nature Reviews Materials, 2020. **5**(3): p. 173-195.
37. Sawa, A., *Resistive switching in transition metal oxides.* Materials today, 2008. **11**(6): p. 28-36.

38. Kumar, D., R. Aluguri, U. Chand, and T.-Y. Tseng, *Metal oxide resistive switching memory: materials, properties and switching mechanisms.* Ceramics International, 2017. **43**: p. S547-S556.

39. Jeong, D.S., R. Thomas, R. Katiyar, J. Scott, H. Kohlstedt, A. Petraru, and C.S. Hwang, *Emerging memories: resistive switching mechanisms and current status.* Reports on Progress in Physics, 2012. **75**(7): p. 076502.

40. Jeong, D.S., H. Schroeder, and R. Waser, *Coexistence of bipolar and unipolar resistive switching behaviors in a Pt⁄TiO₂⁄Pt stack.* Electrochemical and solid-state letters, 2007. **10**(8): p. G51.

41. Do, Y.H., J.S. Kwak, J.P. Hong, H. Im, and B.H. Park, *Nonvolatile unipolar and bipolar resistive switching characteristics in Co-doped TiO_2 thin films with different compliance currents.* J. Korean Phys. Soc, 2009. **55**(2009): p. 1009-1012.

42. Waser, R. and M. Aono, *Nanoionics-based resistive switching memories.* Nature Materials, 2007. **6**(11): p. 833-840.

43. Kim, K.M., D.S. Jeong, and C.S. Hwang, *Nanofilamentary resistive switching in binary oxide system; a review on the present status and outlook.* Nanotechnology, 2011. **22**(25): p. 254002.

44. Waser, R., R. Dittmann, G. Staikov, and K. Szot, *Redox-based resistive switching memories–nanoionic mechanisms, prospects, and challenges.* Advanced materials, 2009. **21**(25-26): p. 2632-2663.

45. Yang, J.J., J. Borghetti, D. Murphy, D.R. Stewart, and R.S. Williams, *A family of electronically reconfigurable nanodevices.* Advanced materials, 2009. **21**(37): p. 3754-3758.

46. Fujii, T., M. Kawasaki, A. Sawa, Y. Kawazoe, H. Akoh, and Y. Tokura, *Electrical properties and colossal electroresistance of heteroepitaxial $SrRuO_3$⁄ $SrTi_{1-x}Nb_xO_3$ ($0.0002 \leqslant x \leqslant 0.02$) Schottky junctions.* Physical Review B, 2007. **75**(16): p. 165101.

47. Ielmini, D. and H.-S.P. Wong, *In-memory computing with resistive switching devices.* Nature electronics, 2018. **1**(6): p. 333-343.

48. Prades, M., N. Masó, H. Beltrán, E. Cordoncillo, and A.R. West, *Field enhanced bulk conductivity of $BaTiO_3$: Mg ceramics.* Journal of Materials Chemistry, 2010. **20**(25): p. 5335-5344.

49. Zhang, Q.-L., N. Masó, Y. Liu, H. Yang, and A.R. West, *Voltage-dependent low-field resistivity of $CaTiO_3$: Zn ceramics.* Journal of Materials Chemistry, 2011. **21**(34): p. 12894-12900.

50. Rubi, D., F. Gomez-Marlasca, P. Bonville, D. Colson, and P. Levy, *Resistive switching in ceramic multiferroic $Bi_{0.9}Ca_{0.1}FeO_3$.* Physica B: Condensed Matter, 2012. **407**(16): p. 3144-3146.

51. Arnold, D.C., *Composition-driven structural phase transitions in rare-earth-doped BiFeO 3 ceramics: A review.* IEEE transactions on ultrasonics, ferroelectrics, and frequency control, 2015. **62**(1): p. 62-82.

52. Catalan, G. and J.F. Scott, *Physics and applications of bismuth ferrite.* Advanced materials, 2009. **21**(24): p. 2463-2485.

53. Chen, W.-t., A.J. Williams, L. Ortega-San-Martin, M. Li, D.C. Sinclair, W. Zhou, and J.P. Attfield, *Robust antiferromagnetism and structural disorder in $Bi_xCa_{1-x}FeO_3$ perovskites.* Chemistry of Materials, 2009. **21**(10): p. 2085-2093.

54. Maso, N. and A.R. West, *Electrical properties of Ca-doped $BiFeO_3$ ceramics: from p-type semiconduction to oxide-ion conduction.* Chemistry of Materials, 2012. **24**(11): p. 2127-2132.

55. Liu, Y. and A.R. West, *Voltage-dependent resistance of undoped rutile, TiO_2, ceramics.* Applied physics letters, 2013. **103**(26): p. 263508.

56. Curtis C, E., M. Doney L, and R. Johnson J, *Some Properties of Hafnium Oxide, Hafnium Silicate, Calcium Hafnate, and Hafnium Carbide.* Journal of the American Ceramic Society, 2006. **37**(10): p. 458-465.

57. Schwarzenbach, D., *Early days of x-ray crystallography.* Crystallography Reviews, 2014. **20**(2): p. 155-156.

58. Zhao, X. and D. Vanderbilt, *First-principles study of structural, vibrational, and lattice dielectric properties of hafnium oxide.* Physical Review B, 2002. **65**(23): p. 233106.

59. Lee, B.H., L. Kang, R. Nieh, W.-J. Qi, and J.C. Lee, *Thermal stability and electrical characteristics of ultrathin hafnium oxide gate dielectric reoxidized with rapid thermal annealing.* Applied Physics Letters, 2000. **76**(14): p. 1926-1928.

60. Balog, M., M. Schieber, M. Michman, and S. Patai, *Chemical vapor deposition and characterization of HfO_2 films from organo-hafnium compounds.* Thin Solid Films, 1977. **41**(3): p. 247-259.

61. Trubelja, M.F. and V.S. Stubican, *Ionic conductivity in the hafnia-R_2O_3 systems.* Solid State Ionics, 1991. **49**: p. 89-97.
62. STACY, D.W. and D.R. WILDER, *The Yttria-Hafnia System.* Journal of the American Ceramic Society, 1975. **58**(7-8): p. 285-288.
63. West, A.R., *Solid State Chemistry and its Applications*. 2013: John Wiley & Sons Ltd.
64. Smart, L., *Solid state chemistry : an introduction*, ed. E. Moore. 1992, London: London : Chapman and Hall, 1992.
65. Park, M.H., Y.H. Lee, T. Mikolajick, U. Schroeder, and C.S. Hwang, *Review and perspective on ferroelectric HfO 2-based thin films for memory applications.* MRS Communications, 2018. **8**(3): p. 795-808.
66. Müller, J., P. Polakowski, S. Mueller, and T. Mikolajick, *Ferroelectric hafnium oxide based materials and devices: Assessment of current status and future prospects.* ECS Journal of Solid State Science and Technology, 2015. **4**(5): p. N30-N35.
67. Max, B., M. Pešić, S. Slesazeck, and T. Mikolajick, *Interplay between ferroelectric and resistive switching in doped crystalline HfO_2.* Journal of Applied Physics, 2018. **123**(13): p. 134102.
68. Koo, J.-M., B.-S. Seo, S. Kim, S. Shin, J.-H. Lee, H. Baik, J.-H. Lee, J.H. Lee, B.-J. Bae, and J.-E. Lim. *Fabrication of 3D trench PZT capacitors for 256Mbit FRAM device application*. in *Electron Devices Meeting, 2005. IEDM Technical Digest. IEEE International*. 2005: IEEE.
69. Polakowski, P., S. Riedel, W. Weinreich, M. Rudolf, J. Sundqvist, K. Seidel, and J. Muller. *Ferroelectric deep trench capacitors based on Al: HfO_2 for 3D nonvolatile memory applications*. in *Memory Workshop (IMW), 2014 IEEE 6th International*. 2014: IEEE.
70. Trubelja, M.F. and V.S. Stubican, *Ionic Conductivity of the Fluorite-Type Hafnia–R_2O_3 Solid Solutions.* Journal of the American Ceramic Society, 1991. **74**(10): p. 2489-2494.
71. Kharton, V.V., F.M.B. Marques, and A. Atkinson, *Transport properties of solid oxide electrolyte ceramics: a brief review.* Solid State Ionics, 2004. **174**(1): p. 135-149.
72. Johansen, H. and J. Cleary, *High-Temperature Electrical Conductivity in the Systems CaO-ZrO_2 and CaO-HfO_2.* Journal of The Electrochemical Society, 1964. **111**(1): p. 100-103.
73. Schieltz, J.D., *Electrolytic behavior of yttria and yttria stabilized hafnia.* 1970.

74. Carter, R. and W.L. Roth, *Conductivity and structure in calcia-stabilized zirconia.* Electrochemical Force Measurements in High Temperature Systems, 1968: p. 125-144.

75. Shibayama, S., T. Nishimura, S. Migita, and A. Toriumi, *Thermodynamic control of ferroelectric-phase formation in $Hf_xZr_{1-x}O_2$ and ZrO_2.* Journal of Applied Physics, 2018. **124**(18): p. 184101.

76. Shimizu, T., K. Katayama, and H. Funakubo, *Stability of the orthorhombic phase in (111)-oriented $YO_{1.5}$-substituted HfO_2 films.* Journal of the Ceramic Society of Japan, 2018. **126**(5): p. 269-275.

77. Muller, J., T.S. Boscke, U. Schroder, S. Mueller, D. Brauhaus, U. Bottger, L. Frey, and T. Mikolajick, *Ferroelectricity in simple binary ZrO_2 and HfO_2.* Nano letters, 2012. **12**(8): p. 4318-4323.

78. Mittmann, T., M. Materano, S.-C. Chang, I. Karpov, T. Mikolajick, and U. Schroeder. *Impact of oxygen vacancy content in ferroelectric HZO films on the device performance*. in *2020 IEEE International Electron Devices Meeting (IEDM)*. 2020: IEEE.

79. Schroeder, U., C. Richter, M.H. Park, T. Schenk, M. Pesic, M. Hoffmann, F.P. Fengler, D. Pohl, B. Rellinghaus, and C. Zhou, *Lanthanum-doped hafnium oxide: a robust ferroelectric material.* Inorganic chemistry, 2018. **57**(5): p. 2752-2765.

80. Mueller, S., J. Mueller, A. Singh, S. Riedel, J. Sundqvist, U. Schroeder, and T. Mikolajick, *Incipient ferroelectricity in Al-doped HfO_2 thin films.* Advanced Functional Materials, 2012. **22**(11): p. 2412-2417.

81. Shimizu, T., K. Katayama, and H. Funakubo, *Epitaxial growth of $YO_{1.5}$ doped HfO_2 films on (100) YSZ substrates with various concentrations.* Ferroelectrics, 2017. **512**(1): p. 105-110.

82. Shimizu, T., K. Katayama, T. Kiguchi, A. Akama, T.J. Konno, O. Sakata, and H. Funakubo, *The demonstration of significant ferroelectricity in epitaxial Y-doped HfO_2 film.* Scientific Reports, 2016. **6**(1): p. 1-8.

83. Li, T., M. Ye, Z. Sun, N. Zhang, W. Zhang, S. Inguva, C. Xie, L. Chen, Y. Wang, and S. Ke, *Origin of ferroelectricity in epitaxial Si-doped HfO_2 films.* ACS applied materials & interfaces, 2019. **11**(4): p. 4139-4144.

84. Shimizu, T., T. Yokouchi, T. Oikawa, T. Shiraishi, T. Kiguchi, A. Akama, T.J. Konno, A. Gruverman, and H. Funakubo, *Contribution of oxygen vacancies to the ferroelectric behavior of $Hf_{0.5}Zr_{0.5}O_2$ thin films.* Applied physics letters, 2015. **106**(11): p. 112904.

85. Hyuk Park, M., H. Joon Kim, Y. Jin Kim, T. Moon, and C. Seong Hwang, *The effects of crystallographic orientation and strain of thin $Hf_{0.5}Zr_{0.5}O_2$ film on its ferroelectricity.* Applied physics letters, 2014. **104**(7): p. 072901.

86. Shiraishi, T., K. Katayama, T. Yokouchi, T. Shimizu, T. Oikawa, O. Sakata, H. Uchida, Y. Imai, T. Kiguchi, and T.J. Konno, *Effect of the film thickness on the crystal structure and ferroelectric properties of $(Hf_{0.5}Zr_{0.5})O_2$ thin films deposited on various substrates.* Materials Science in Semiconductor Processing, 2017. **70**: p. 239-245.

87. Lee, Y.H., H.J. Kim, T. Moon, K. Do Kim, S.D. Hyun, H.W. Park, Y.B. Lee, M.H. Park, and C.S. Hwang, *Preparation and characterization of ferroelectric $Hf_{0.5}Zr_{0.5}O_2$ thin films grown by reactive sputtering.* Nanotechnology, 2017. **28**(30): p. 305703.

88. Zhang, Y., J. Xu, C.-K. Choi, Z.-X. Fang, P. Li, L. Yuan, and L. Chen, *Investigation of temperature-dependent ferroelectric properties of Y-doped HfO_2 thin film prepared by medium-frequency reactive magnetron co-sputtering.* Vacuum, 2020. **179**: p. 109506.

89. Starschich, S., T. Schenk, U. Schroeder, and U. Boettger, *Ferroelectric and piezoelectric properties of $Hf_{1-x}Zr_xO_2$ and pure ZrO_2 films.* Applied physics letters, 2017. **110**(18): p. 182905.

90. Starschich, S., D. Griesche, T. Schneller, R. Waser, and U. Böttger, *Chemical solution deposition of ferroelectric yttrium-doped hafnium oxide films on platinum electrodes.* Applied physics letters, 2014. **104**(20): p. 202903.

91. Schroeder, U., T. Mittmann, M. Materano, P.D. Lomenzo, P. Edgington, Y.H. Lee, M. Alotaibi, A.R. West, T. Mikolajick, and A. Kersch, *Temperature-Dependent Phase Transitions in $Hf_xZr_{1-x}O_2$ Mixed Oxides: Indications of a Proper Ferroelectric Material.* Advanced Electronic Materials, 2022: p. 2200265.

92. Pešić, M., F.P.G. Fengler, L. Larcher, A. Padovani, T. Schenk, E.D. Grimley, X. Sang, J.M. LeBeau, S. Slesazeck, and U. Schroeder, *Physical mechanisms behind the field-cycling behavior of HfO_2-based ferroelectric capacitors.* Advanced Functional Materials, 2016. **26**(25): p. 4601-4612.

93. Schroeder, U., C.S. Hwang, and H. Funakubo, *Ferroelectricity in Doped Hafnium Oxide: Materials, Properties and Devices*. 2019: Woodhead Publishing.

94. Kim, K., M. Park, H. Kim, Y. Kim, T. Moon, Y. Lee, S. Hyun, T. Gwon, and C. Hwang, *Ferroelectricity in undoped-HfO_2 thin films induced by deposition temperature control*

during atomic layer deposition. Journal of Materials Chemistry C, 2016. **4**(28): p. 6864-6872.

95. Wang, J., D. Zhou, W. Dong, Z. Li, N. Sun, X. Hou, and F. Liu, *Effect of the Hf content on the microstructure and ferroelectric properties of $Hf_xZr_{1-x}O_2$ thin films using an all-inorganic aqueous precursor solution.* Nanoscale, 2021. **13**(38): p. 16216-16225.

Chapter 3 Characterisation techniques

3.1 X-ray Diffraction (XRD)

X-ray diffraction, XRD, is a common technique in inorganic chemistry used for both determining the phases present in samples and calculating lattice parameters of pure phases and solid solution series. The interaction of X-ray radiation with crystal lattices occurs according to Bragg's law:

$$2d\sin\theta = n\lambda \qquad (3.1)$$

where λ is the wavelength of the incident beam, n the is order of reflection, θ is the Bragg angle, and d is the distance of inter-planar separation. Constructive interference occurs when reflected beams are in phase, as shown in Figure 3.1.

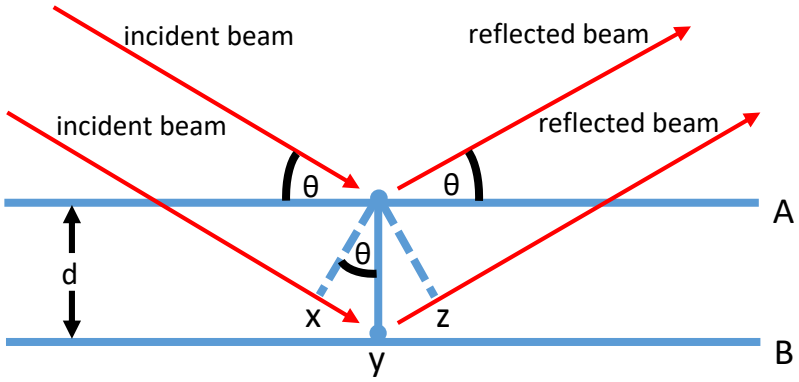

Figure 3.1 Bragg's law derivation

In order to carry out phase analysis of samples, XRD was studied on crushed sintered pellets after the final stage of ceramic processing. In this project, two XRD diffractometers were employed for phase examination: a Bruker D2 Phaser with Cu Kα (λ= 1.541 Å) for phase identification and a Stoe Stadi P Diffractometer, Cu $K\alpha_1$ (λ= 1.5406 Å) for accurate lattice parameter measurements over the range 20°<2θ<90° with Si internal standard to calibrate

the peak positions. Data were analysed using Win X^{Pow} software (ver.2.04, STOE&Cie GmbH, Hilpertstr., Germany).

3.2 Determination of ceramic densities

In order to measure the relative density of pellets for each composition, the experimental density, $\rho_{exp,}$ of sintered pellets was measured and divided by the theoretical density, ρ_{th}, according to the following formula:

$$\rho_{exp} = \frac{\text{Mass of pellet}}{\text{Volume of pellet}} = \frac{M}{\pi r^2 h} \quad (3.2)$$

$$\rho_{th} = \frac{\text{Mass of unit cell}}{\text{Volume of unit cell}} = \frac{\text{molcular weight} \times Z}{V_{cell} \times 10^{-24} \times N_a} \quad (3.3)$$

where

h → pellet thickness (cm)

r → radius (cm)

V_{cell} → unit cell volume ($Å^3$)

N_a → Avogadro number ($6.022 \times 10^{23}\ mole^{-1}$)

Z → formula units per unit cell (Z = 4 for the face centred cubic crystal structure of HfO_2)

$$\rho_{re} = (\rho_{exp}/\rho_{th}) \text{ X } 100 \quad (3.4)$$

In the experimental density measurements, the dimensions of the sintered pellet (the diameter and thickness) were measured by a micrometer, whereas in the theoretical density calculation, the unit cell volume was taken from the lattice parameter obtained from XRD data.

3.3 Scanning electron microscopy (SEM)

So as to produce SEM images and EDX for each composition, sintered samples were firstly ground using 400, 800, and 1200 grit sandpaper. Further polishing was performed using AutoMet^{TM} grinder-polisher as shown in Table 3.1. The polished samples were etched thermally by heating to 80 % of their sintering temperature for 30 minutes. After that, samples were placed in a SEM sample holder and carbon-coated to prevent charging during operation.

Sintered sample microstructures were examined using field-emission scanning electron microscopy (FEI inspect F50) for SEM imaging and energy-dispersion analysis of X-rays (SEM/EDX) for chemical analysis.

Table 3.1 Metallographic polishing specifications.

Step	Polishing paper	Time (min)	Force (N)	Rotational speed (rpm)
1	6 µm	10	10	150
2	3 µm	10	10	150
3	1 µm	10	10	150
4	0.04 colloidal SiO_2	20	10	150

3.4 Impedance spectroscopy (IS)

Electrical properties of ceramic oxides rely upon the properties of either their individual grains or interfaces such as surfaces and grain boundaries. Impedance spectroscopy is an effective tool for analysing the electrical properties and making a clear separation of the impact of different electro-active regions of ceramic materials [1, 2]. In this project, impedance measurements were taken as a function of three variables, temperature, oxygen partial pressure and dc bias.

For impedance measurements, electrodes were coated from Au or Pt paste on opposite pellet faces and dried at 850 and 900 ^{o}C for 2 hours, respectively. Pellets were loaded into a jig, as shown in Figure 3.2 and 3.7, and placed in a tube furnace. Impedance measurements were conducted using a Modulab XM Solartron analyser (Solartron Analytical Ltd, Farnborough, UK) in air with a frequency range 0.1 Hz-1000 kHz. A Solartron SI 1260 impedance analyser (Solartron Analytical Ltd, Farnborough, UK) with a frequency range 0.1 Hz-1000 kHz was employed for measurements under variable oxygen partial pressure. A Precision Impedance Analyser was also used with a frequency range 40 Hz—110 MHz for impedance measurements under the application of dc bias. The ac voltage that was applied for all samples was nominally 100 mV.

Impedance data were recorded, separately, on open circuit to correct for parallel capacitance of the conductivity jig and on closed circuit, to correct for series inductance of the equipment. Data were corrected for overall sample geometry and electrode contact area.

This allowed resistances and capacitances to be recorded in resistivity and permittivity units of Ωcm and Fcm^{-1}, respectively. IS data were analysed by Zview software

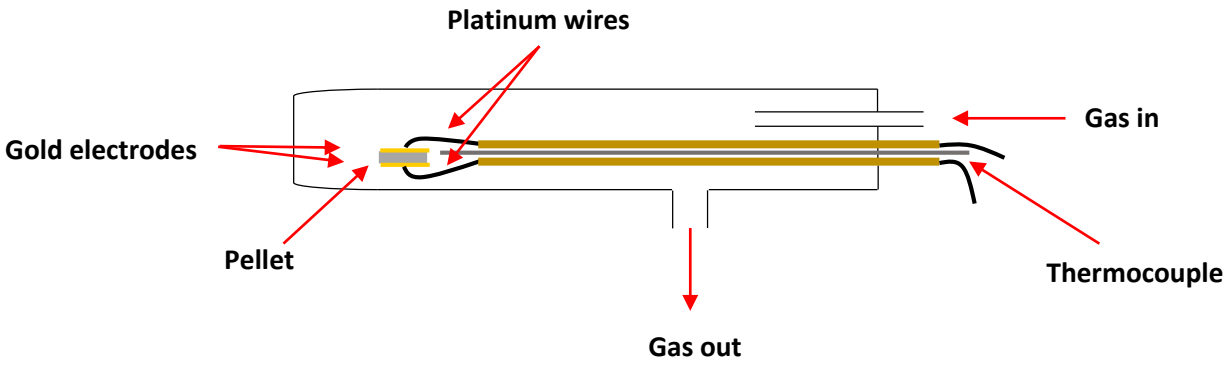

Figure 3.2 Spaghetti jig (A Spaghetti jig is an Alumina tube with 4 bore holes. Two holes are used for a thermocouple and the other two for Pt wires that are used as electrodes and to hold the sample to make IS measurements).

A comprehensive analysis of IS data is usually presented by four types of plots: complex plane plot (Z*), spectroscopic plots of capacitance (C'), admittance (Y'), and Z''/M''. These are interrelated via the following equations:

$$Z^* = (Y^*)^{-1} \qquad (3.5)$$

$$M^* = j\omega C_0 Z^* \qquad (3.6)$$

$$\varepsilon^* = (M^*)^{-1} \qquad (3.7)$$

where is C_0 is the capacitance of the conductivity cell that the sample being measured in, j = $\sqrt{-1}$ and ω = angular frequency $2\pi f$. Every formula of these equations has a real and imaginary component, e.g.:

$$Z^* = Z' - jZ'' \qquad (3.8)$$

Following these interrelated equations, data can be presented either as complex plane plots such as Z'' *vs* Z' i.e. both real and imaginary components are plotted on a linear scale or as spectroscopic plot such as Z'', M'' *vs* $\log f$ i.e. the real or imaginary component on a linear scale is plotted versus frequency on a logarithmic scale.

A methodology for interpreting impedance results physically and obtaining accurate data is to find the most appropriate equivalent circuit that simulates the experimental data. Each effective region (for example grain, grain boundary and surface layer) in electro-ceramics can be characterised, ideally, by a parallel R-C element that consists of its resistance (R) and

capacitance (C), as shown in Figure 3.4a. Different regions have different time constant, τ, given by the magnitude of their R and C product:

$$\tau = RC \qquad (3.9)$$

Due to non-ideality of ac response of many ceramic materials, it is difficult to model them by a circuit of only ideal parallel resistive and capacitive elements. The need for extra elements such as a constant phase element (CPE) is important to obtain an accurate modelling of IS data, Figure 3.4b. CPE provides variable resistors and capacitors which have the ability to overcome departures from an ideal frequency-independent R-C circuit [3].

A CPE is used to fit a power law dependence on frequency of the R-C elements of the admittance, as illustrated in Figure 3.5b. A circuit consisting of parallel R-CPE-C shows an accurate modelling of the bulk impedance of many ionic/electronic hopping conductors [4-10]. The admittance of a CPE is given by the following equation:

$$Y^*_{CPE} = A\omega^n + jB\omega^n = Y' + jY'' \quad (3.10)$$

where n and A are parameters that are independent of frequency, but are usually dependent on temperature. The values of n and A have been associated with possible extrinsic and intrinsic processes of electro-effective components such as bulk conduction or/and sample-electrode interface processes [3]. At the simplest level, n takes values in the range between 1 and 0. The CPE is purely capacitive when n=1 and is purely resistive when n=0. A high frequency dispersion seen in admittance plot, Figure 3.5 b, is defined by the following equation:

$$Y' = {}^{1}/_{R} + A\omega^n \cos\left({}^{n\pi}/_{2}\right) \qquad (3.11)$$

The impedance response of sample-electrode interfaces can provide significant information about the type of charge carrier present in a material. For oxide ion conductors, as an example, there is a redox reaction between oxygen molecules and O^{2-} ions at the sample-electrode interface. During the *ac* impedance measurements, O^{2-} from the interior of the sample is discharged as oxygen gas at the anode where the electrons are liberated and go through the external circuit. In contrast, at the cathode, O_2 gas is adsorbed on the surface of the sample and dissociation of O_2 molecules to O^{2-} ions occurs leading to a diffusion of

O^{2-} ions inside the sample interior. These redox reactions at the two electrode-sample interfaces are represented by the charge transfer impedance.

At low frequency, there is usually difficulty for oxide ions to cross the sample-electrode interface. Hence, at the lowest frequencies in impedance data an extra impedance called "Warburg impedance" is usually shown that represents the diffusion of oxygen molecules towards and away from sample-electrode interface. The Warburg impedance appears as a spike in Z* plots with an inclined angle of 45 ° and modelling by CPE element that takes an ideal n value of 0.5, as represented in Figure 3.5a. The typical impedance response of a material that has an oxide ion conducting mechanism with bulk, grain boundary and Warburg spike is shown in Figure 3.5a.

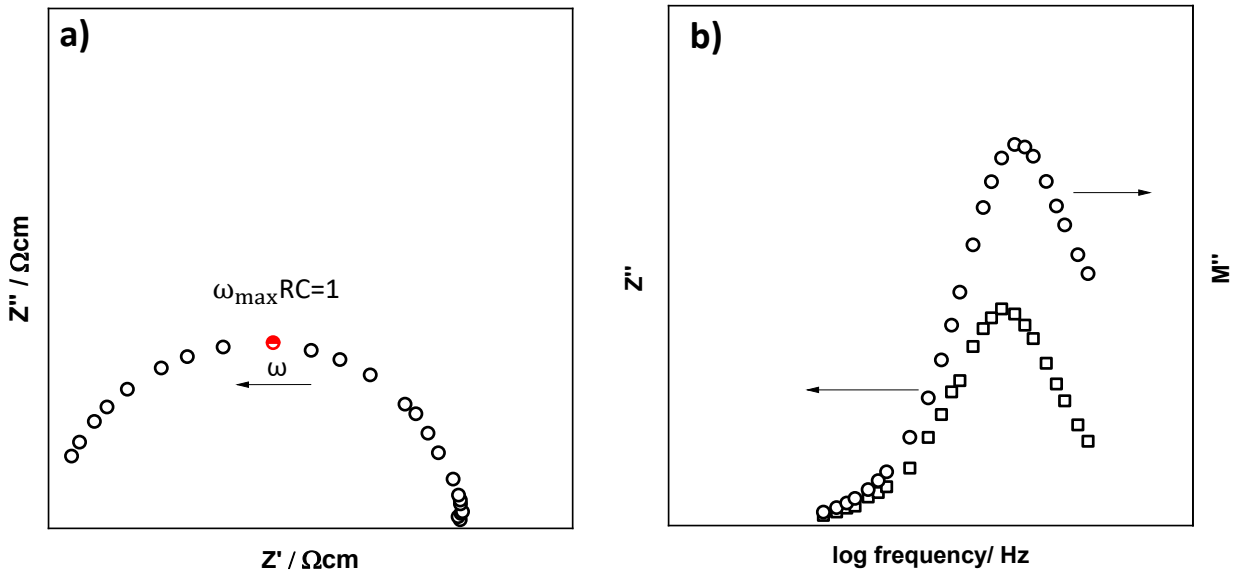

Figure 3.3 a) Typical Z* plot and b) Z''/M'' spectroscopic plots versus log (f) showing a single semi-circular arc for parallel R-CPE-C elements.

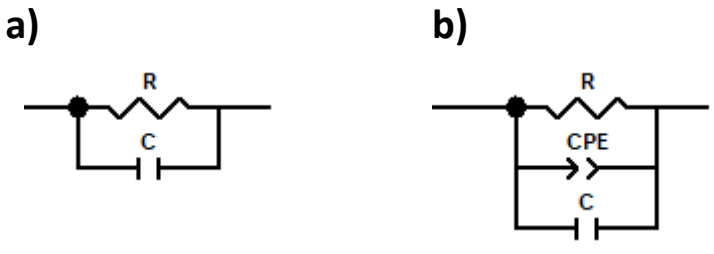

Figure 3.4 Parallel a) R-C element b) R-CPE-C element

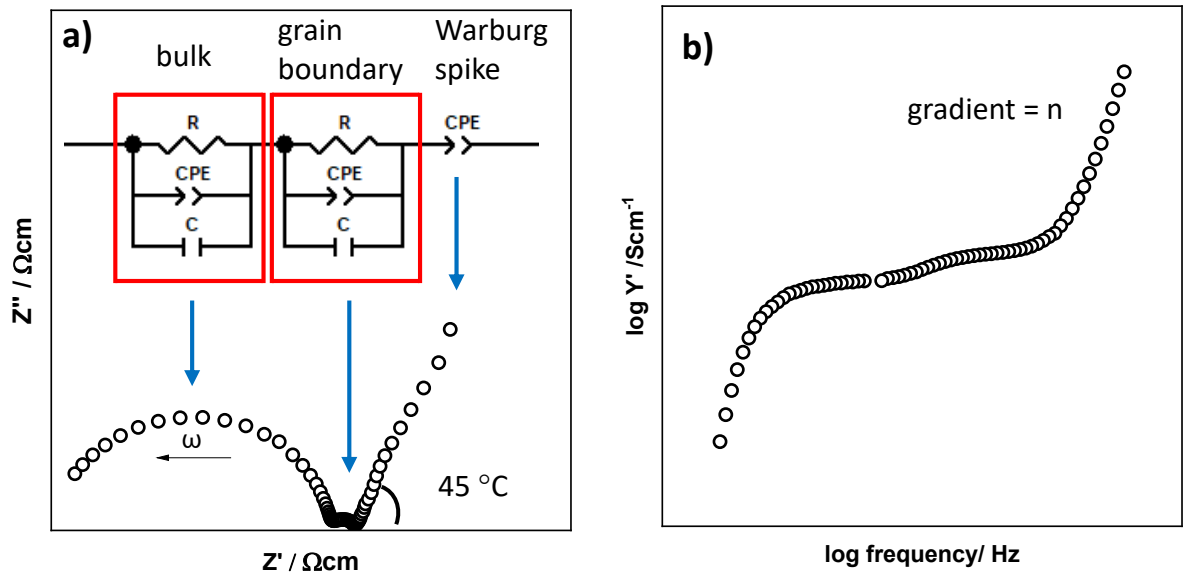

Figure 3.5 A typical a) complex plane plot b) admittance plot for oxide ion conductors showing bulk, grain boundary and Warburg spike impedance components.

The brickwork layer model shown in Figure 3,6 is often used to represent the ideal crystalline solid and illustrating grain, *bulk*, and its thickness, t_b, grain boundary and its thickness, t_{gb}, and electrode-sample interface and its thickness, t_e. For identifying the bulk, grain boundary and other regions in an impedance data set, each region of a ceramic material always has distinguishable capacitance values. The responsible region with its possible capacitance is summarised in Table 3.2, according to the following capacitance equation:

$$C = \varepsilon_r \varepsilon_0 (A/t) \qquad (3.12)$$

where C is the capacitance, ε_r is the relative permittivity, ε_0 is the free space permittivity, A is the sample surface area, and t is the sample's thickness. The capacitance value of each region depends on its thickness according to following equation:

$$\frac{C_b}{C_{gb}} = \frac{t_b}{t_{gb}} \qquad (3.13)$$

Prior to analysing and interpreting impedance data, it is important to assume that the capacitance value of grain, *bulk*, is much lower than that of grain boundary because the bulk region is a much thicker layer. Since bulk regions fill most of the space in sintered ceramics, the correction of impedance data is usually employed for overall sample geometry which gives an accurate capacitance value for only the bulk.

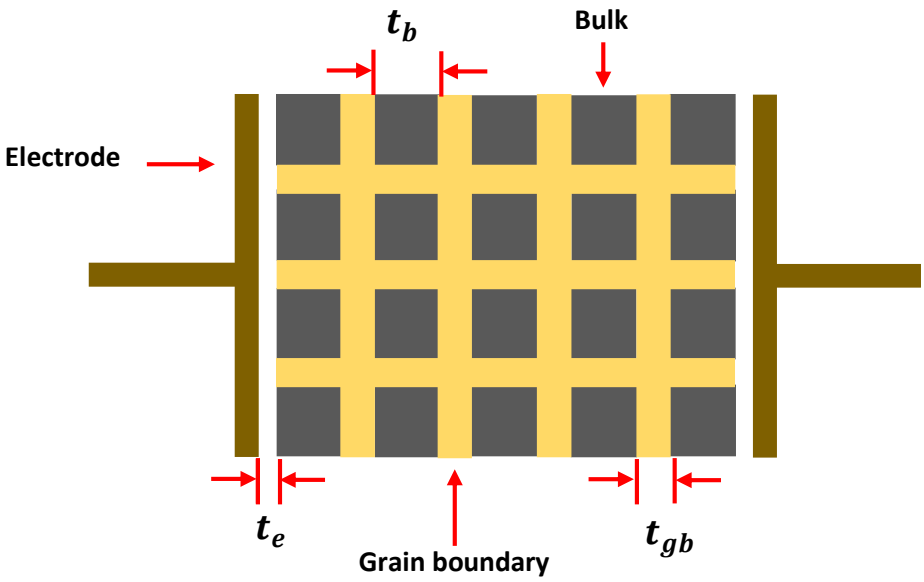

Figure 3.6 An illustrated schematic for the Brickwork layer model indicating the bulk, grain boundary and electrode-sample interface.

Table 3.2 Possible phenomenon and its capacitance value [1, 2].

Responsible area	**Capacitance (Fcm^{-1})**
Electrode-sample interface	10^{-5} to 10^{-7}
Surface layer (depletion layer)	10^{-7} to 10^{-9}
Electrochemical reaction	10^{-4} or higher
Second phase, constriction capacitance	10^{-11}
Grain boundary	10^{-8} to 10^{-11}
Bulk ferroelectric	10^{-9} to 10^{-10}
Bulk	10^{-12}

3.5 Fixed frequency capacitance measurements: Inductance-capacitance-resistance (LCR) meter

Fixed frequency measurements were performed in air as a function of temperature using a LCR meter (Model 4284A, Hewlett Packard GmbH, Böblingen, Germany). A sample was placed between two platinum wires in a compression-contact jig, see Figure 3.7, and measured at 5 fixed frequencies 1, 10, 100, 250 kHz and 1 MHz. Capacitance was measured every minute from room temperature to the target temperature with a heating rate 1 °C/min. The relative permittivity was calculated via using the following formula:

$$\varepsilon_r = \frac{C}{\varepsilon_0} \times \frac{t}{A} \qquad (3.14)$$

where ε_r is the relative permittivity, ε_0 the permittivity of free space, C is the measured capacitance, t is the thickness and A is the surface area of the sample.

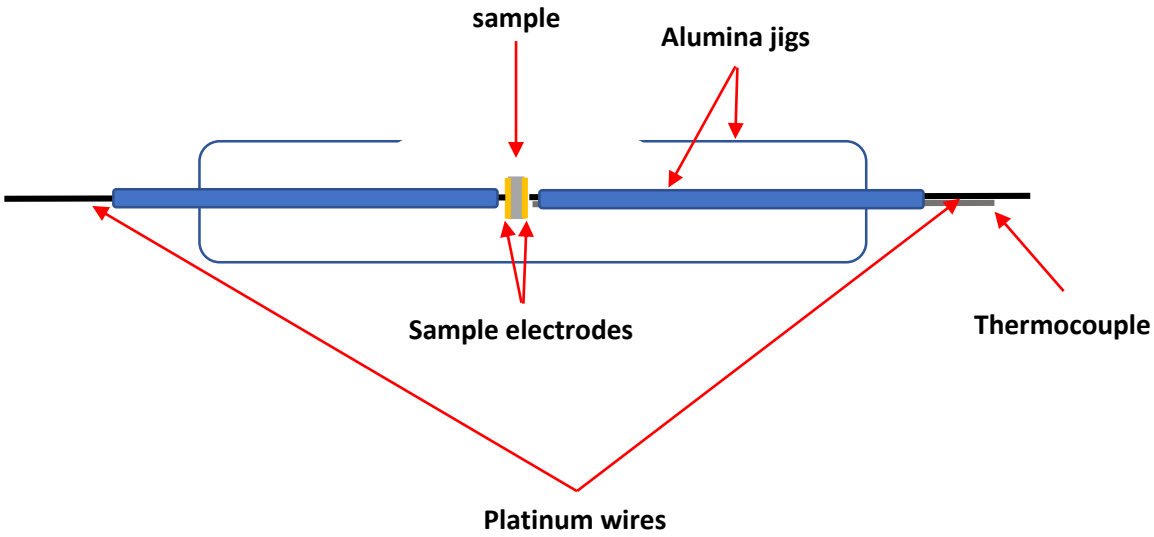

Figure 3.7 Compression jig.

3.6 Oxygen transport number measurements

Oxygen ion transport number measurements made use of a ProboStat system (NorECs Norwegian Electro Ceramics AS, Oslo, Norway). Dense ceramics were coated with Pt paste (dried at 900 °C for 2 h) electrodes on opposite faces and sealed to one end of a YSZ tube by a commercial glass frit (KeraGlass ST K02), as illustrated in Figure 3.8. Pairs of Pt wires were connected to the outer and inner sample faces, and the outer and inner YSZ tube surfaces;

voltages were measured using a Keithley 182 sensitive digital voltmeter (Keithley, Ohio, USA). During measurements, lab air was used as the outer tube atmosphere and flowing N_2 gas (99.998% purity) as the inner tube atmosphere to generate a pO_2 gradient.

The voltage between each pair of electrodes is given by:

$$E = t_{ion} \frac{kT}{4e} \ln\left(\frac{P_{O_2}^{out}}{P_{O_2}^{in}}\right) \qquad (3.15)$$

$$t_{ion} = \frac{\sigma_{O^{2-}}}{\sigma_{total}} \qquad (3.16)$$

where T is temperature, k is Boltzmann's constant, e is electronic charge, t_{ion} is the ion transport number and $\sigma_{O^{2-}}$ and σ_{total} are the oxide ion and total conductivities of the material between the electrodes.

For any set of measurements, the test sample and YSZ tube were at the same temperature and in the same pO_2 gradient; t_{ion} of the test sample was obtained from:

$$t_{ion,sample} = \frac{E_{sample}}{E_{YSZ}} t_{ion,YSZ} \qquad (3.17)$$

YSZ is considered to be a pure oxide conductor (i.e. $t_{ion,YSZ} = 1$) at high temperatures (> 600 ^oC), and thus the oxygen ion transport number of the test sample was produced via (3.13). Measurements were made at 600, 700, and 800 °C and the experimental set-up was equilibrated for 24 h at each temperature before measurements were taken.

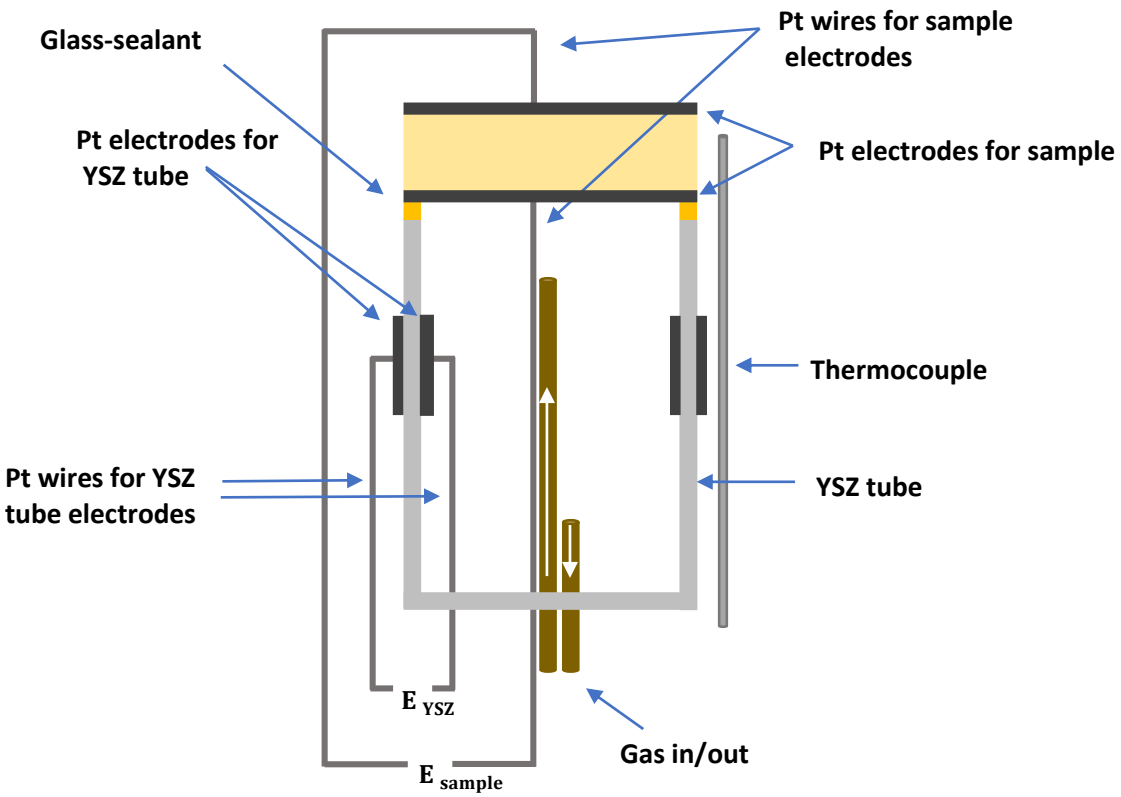

Figure 3.8 Schematic diagram of the set-up used for oxygen ion transport number measurements.

3.7 References

1. Sinclair, D.C., *Characterisation of electro-materials using ac impedance spectroscopy.* Boletín de la Sociedad Española de Cerámica y Vidrio, 1995. **34**(2): p. 55-65.
2. Irvine, J.T., D.C. Sinclair, and A.R. West, *Electroceramics: characterization by impedance spectroscopy.* Advanced materials, 1990. **2**(3): p. 132-138.
3. Hernandez, M.A. and A.R. West, *Dipolar relaxation and impedance of an yttria-stabilised zirconia ceramic electrolyte.* Journal of Materials Chemistry A, 2016. **4**(4): p. 1298-1305.
4. Hernández, M.A., N. Masó, and A.R. West, *On the correct choice of equivalent circuit for fitting bulk impedance data of ionic/electronic conductors.* Applied physics letters, 2016. **108**(15): p. 152901.
5. Perejón, A., N. Masó, A.R. West, P.E. Sánchez-Jiménez, R. Poyato, J.M. Criado, and L.A. Pérez-Maqueda, *Electrical properties of stoichiometric $BiFeO_3$ prepared by mechanosynthesis with either conventional or spark plasma sintering.* Journal of the American Ceramic Society, 2013. **96**(4): p. 1220-1227.
6. Bruce, P.G., A. West, and D. Almond, *A new analysis of ac conductivity data in single crystal β-alumina.* Solid State Ionics, 1982. **7**(1): p. 57-60.
7. Osman, R.A. and A.R. West, *Electrical characterization and equivalent circuit analysis of $(Bi_{1.5}Zn_{0.5})(Nb_{0.5}Ti_{1.5})O_7$ Pyrochlore, a relaxor ceramic.* Journal of Applied Physics, 2011. **109**(7): p. 074106.
8. Bruce, P.G. and A. West, *The A-C Conductivity of Polycrystalline LISICON, $Li_{2+2x}Zn_{1-x}GeO_4$, and a Model for Intergranular Constriction Resistances.* Journal of The Electrochemical Society, 1983. **130**(3): p. 662.
9. Masó, N., X. Yue, T. Goto, and A.R. West, *Frequency-dependent electrical properties of ferroelectric $BaTi_2O_5$ single crystal.* Journal of Applied Physics, 2011. **109**(2): p. 024107.
10. Abram, E., D. Sinclair, and A. West, *A strategy for analysis and modelling of impedance spectroscopy data of electroceramics: doped lanthanum gallate.* Journal of Electroceramics, 2003. 10(3): p. 165-177.

Chapter 4: Electrical properties of yttria-stabilised hafnia ceramics

4.1 Introduction

Yttria-stabilised zirconia, YSZ, and other materials with fluorite-related crystal structures, are oxide ion conductors with principal application as the ceramic electrolyte in electrochemical devices such as: SOFCs that are used in power generation; electrolysers for production of H_2 by water electrolysis; oxygen gas sensors. These applications require an ionic transport number of unity in order to avoid loss of performance in cell operation and power supplies and to give accurate voltage data when they are used for sensor and transport number measurements [1-4].

The high levels of oxide ion conductivity are obtained by doping the parent oxide, ZrO_2 with acceptor (lower valence) dopants such as Y^{3+} or Ca^{2+}; charge balance is achieved by oxygen vacancy creation. The resulting compositions are presented in two possible ways, as either a general formula or using oxide molar ratios. The YSZ composition with highest oxide conductivity is 92 mol% ZrO_2.8 % Y_2O_3, often referred to as YSZ08, which corresponds to x=0.148 in the general formula $Zr_{1-x}Y_xO_{2-x/2}$. Materials such as YSZ08 have a very wide electrolytic domain of oxide ion conductivity which extends to atmospheres with oxygen partial pressure, pO_2 as low as 10^{-20} atm before *n*-type conductivity associated with oxygen loss becomes significant [4-6].

Fluorite-structured doped CeO_2 materials are also good oxide ion conductors but, because of easy reduction of Ce^{4+} to Ce^{3+} which introduces mixed conductivity, they do not have the same independence of pO_2 as ZrO_2-based materials and are of less use as solid electrolytes [7]. HfO_2-based materials are also good oxide ion conductors that are stable to reduction but have been less studied (see literature review of doped hafnia in section 2.5.2).

For application as a solid electrolyte, there is much interest in the pO_2 range over which any electronic conductivity is negligibly small. A transition from the electrolytic domain to a region of dominant *p*-type electronic conductivity should occur for fluorite-structured materials at high pO_2 but is less-well characterised than the transition to *n*-type behaviour at low pO_2, Figure 2.1. Probably this is because of the difficulty in obtaining ready access to pO_2 values that span many orders of magnitude above atmospheric pressure. Recently, for YSZ

materials, *p*-type behaviour has been studied in two ways. First, application of a *dc* bias at the same time as impedance measurements were conducted showed a voltage-dependent conductivity which was enhanced to the extent that, for instance, the electronic transport number of YSZ08 had a value of 0.71 at 556 °C with 12 V applied voltage [8]. Second, YSZ compositions with much higher x values showed a reduction in oxide ion conductivity but at the same time, *p*-type electronic conductivity was observed that was dependent on both pO_2 and *dc* bias [9].

The *p*-type conductivity in these materials is thermally activated and therefore, the holes are localised rather than delocalised in a conduction band. In many cases, the question of the location of holes in oxide electroceramics is either not addressed or is attributed to the presence of unavoidable impurities such as Fe which could oxidise to the Fe^{4+} state by hole creation. Another possibility is that the holes are located on oxygen. In particular, oxide ions that are in an under-bonded environment associated with either acceptor dopants or sample surfaces and interfaces, are surrounded by an effective amount of positive charge that is less than the value of 2+ required for local electroneutrality [8-11] and are therefore possible locations for holes.

The purpose of this chapter is to investigate the electrical properties of yttria-stabilised hafnia ceramics. High levels of oxide ion conduction were anticipated, but it was of particular interest to assess whether, and under what conditions, electronic conduction may also occur. It was presumed that YSH materials would be strongly resistant to reduction and not give *n*-type semi-conduction under standard atmospheric conditions as shown by their suggested use as potentiometric oxygen sensors for liquid sodium, [12] but as yet, there is very little information in the literature about the conditions under which *p*-type semi-conduction may occur. For solid electrolyte applications, the width of the electrolytic window, Figure 2.1, is of fundamental importance, not only at the low pO_2 end associated with the onset of oxygen loss and associated *n*-type semi-conduction, but also at the high pO_2 end associated with oxidation reactions leading to *p*-type semi-conduction.

4.2 Experimental

Three compositions of $Hf_{1-x}Y_xO_{2-x/2}$ with x=0.15, 0.30 and 0.45, were prepared by conventional solid state synthesis utilizing HfO_2 (98%, Sigma- Aldrich) and Y_2O_3 (99.99%, Alfa Aesar) that

were dried before weighing at 1000 and 900 °C, respectively. All samples were hand-mixed in a conventional mortar and pestle with acetone, dried and reacted in alumina crucibles in air at 1300 °C for 10 h. The powders were reground and pressed into pellets, 10 mm diameter, in a uniaxial press at 125 MPa for 2 min. Pellets of x=0.15 were sintered at 1750 °C for 16 h with heating rate 5 °C min^{-1} followed by cooling in the furnace to room temperature; pellets of x=0.30, 0.45 were sintered similarly, but at 1650 °C for 4 days because at higher temperatures than this, they started to react with the alumina boat and melt; they were therefore heated at lower temperature for a long time in order to have a single phase product, Table 4.1. The relative density of pellets, calculated from their dimensions and mass, were 0.93, 0.89 and 0.85 respectively, Table 4.2.

Table 4.1 The status of YSH pellets of general formula $Hf_{1-x}Y_xO_{2-x/2}$ (x=0.15, 0.30 and 0.45) after sintering at different temperatures.

Temperature (°C)	x=0.15	X=0.30	X=0.45
1750	Dense	Partially melted	Completely melted
1700	____	Partially melted	Partially melted
1650	____	Dense	Dense

Table 4.2 Compositions x in $Hf_{1-x}Y_xO_{2-x/2}$ and mol% Y_2O_3, and data for lattice parameter (a), volume (V), measured (D_m), theoretical (D_t) and relative (D_{rel}) densities.

x, mol% Y_2O_3	a (Å)	V (Å^3)	D_t (g/cm^3)	D_m (g/cm^3)	D_{rel} (%)
0.15, 8.1	5.1151(1)	133.83(1)	9.55	8.89	93
0.30, 17.6	5.1468(4)	136.33(3)	8.83	7.84	89
0.45, 29.0	5.1857(7)	139.45(6)	7.94	6.74	85

The reaction products were analyzed at room temperature by X-ray powder diffraction (XRD) on crushed pellets using a Bruker D2 Phaser for phase identification and a Stoe Stadi P Diffractometer, Cu $K\alpha_1$ radiation for lattice parameter determination over the range $20°<2\theta<90°$ with Si internal standard. A combination of field-emission scanning electron microscopy (FEI inspect F50) and energy-dispersion analysis of X-ray (SEM/EDX) were employed to examine the microstructure of sintered samples. Samples were polished and thermally etched at 80 % of their sintering temperature for 30 min before coating with 10 nm of carbon.

Au paste electrodes were coated on opposite pellet faces and dried at 900 °C for 2 h. Impedance spectroscopy (IS) measurements in air over the temperature range 250 - 800 °C and frequency range 0.01 Hz – 1 MHz used a Modulab XM Solartron analyzer and in N_2 or O_2 used a Solartron SI 1260 impedance analyzer (Solartron Analytical Ltd, Farnborough, UK). pO_2 values of the atmospheres used were 1 atm (O_2), 0.21 atm (air) and ~0.01-0.001 atm (N_2). The *ac* voltage for all measurements was 100 mV and IS data were analysed using Zview software. Data were corrected separately for overall sample geometry and electrode contact area. This allowed resistances and capacitances to be recorded in resistivity and permittivity units of Ωcm and Fcm^{-1}, respectively, but additional corrections for grain boundary geometry were not made.

4.3 Results

Phase purity and ceramic microstructure

XRD data for x=0.15 are shown in Figure 4.3(a); similar data were obtained for the other compositions and showed that all were phase-pure by XRD. Data were indexed on a face centred cubic unit cell; the lattice parameter, a, increased approximately linearly with x, (b), consistent with expectations from the literature [13, 14]. SEM results, Figure 4.4(a-c), showed a significant difference between x=0.15 and x=0.30, 0.45. The size of grains decreased and the amount of porosity increased in 0.30, 0.45. These differences are attributed to their lower sintering temperature. Grain sizes are ~30-50 µm in 0.15, ~10-30 µm in 0.30 and 5-30 µm in 0.45. EDS mappings of all compositions indicate homogenous distribution of Hf and Y, Figure 4.4(e-i).

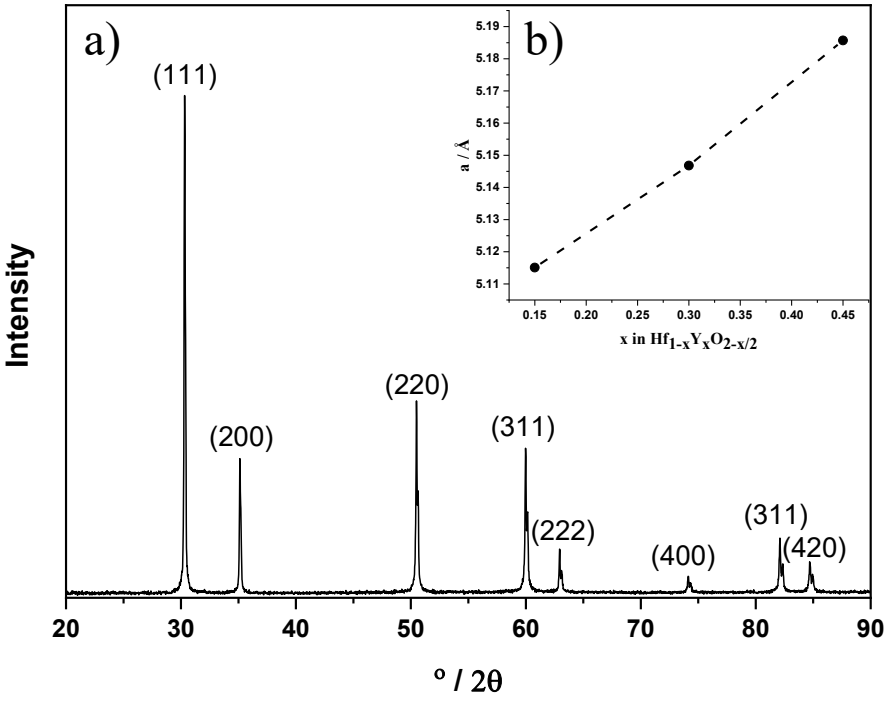

Figure 4.3 a) XRD patterns of $Hf_{1-x}Y_xO_{2-x/2}$ x= 0.15, b) lattice parameter versus x.

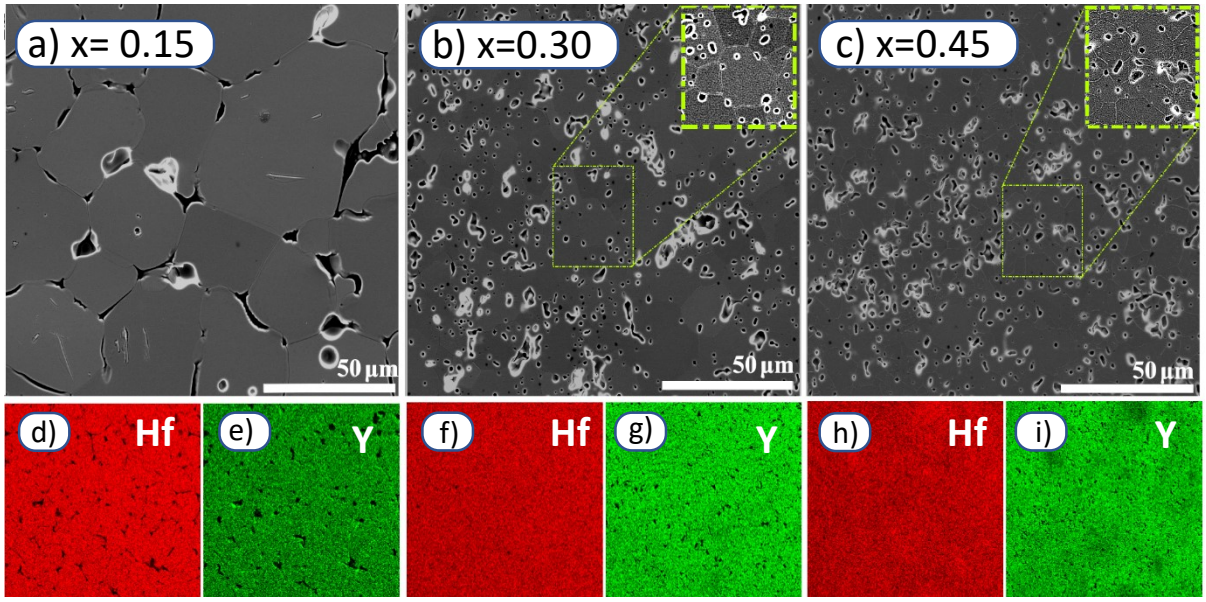

Figure 4.4 Secondary electron images and EDX maps of polished, thermally etched (a,d,e) x=0.15, (b,f,g) x=0.30 and (c,h,i) x=0.45.

Impedance spectroscopy data

A typical set of impedance data, measured in air at 376 °C and plotted in different formats, is shown in Figure 4.5 for a pellet of x=0.15. A selection of datasets for all three compositions

and at different temperatures in the range 275-740 °C, is shown in Supplementary Figures 4.S1-6.

The impedance complex plane plot, Z*, Figure 4.5(a), shows two approximately semicircular arcs at high frequencies and a curved inclined spike at low frequencies. A similar response was observed with all compositions at lower temperatures, Figs 4.S1, 3 and 5. The Z''/M'' spectroscopic plots, (b) show peaks at high frequency in Z'' and M'' and a small peak at intermediate frequencies in Z''. The high frequency peaks are approximately Debye-like with full width at half maximum, FWHM, close to the value for a Debye peak of 1.14 decades, and peak maxima at similar frequencies, both of which indicate a good degree of electrical homogeneity in the bulk response.

C' data, (c), show evidence of a high-frequency plateau, C_1, of value ~ 2 pFcm^{-1}, which corresponds to a permittivity, ε', value of 22.6 calculated from:

$$\varepsilon' = C_1/\varepsilon_0 \qquad (4.1)$$

and attributed to the bulk response; the permittivity of free space (ε_0) is 8.854 x 10^{-14} Fcm^{-1}.

The C' values increase with decreasing frequency, (c), with some evidence for a poorly-resolved intermediate plateau, C_2, at~6 pFcm^{-1}, corresponding to a permittivity of ~ 70. This value is much smaller than expected for a typical grain boundary or surface layer impedance. A similar capacitance has been seen in samples of both yttria- and calcia-stabilised zirconia [15, 16] and attributed to the presence of dipoles created by oxygen vacancy-yttrium/calcium dopant pairs. These dipoles do not contribute to the long range conductivity but are in evidence in the impedance data at high *ac* frequencies.

A poorly-resolved, low frequency C' plateau, C_3, is seen at 0.1 nFcm^{-1} which corresponds to the small, intermediate frequency arc in Z*, (a) and is attributed to a grain boundary impedance. At still lower frequencies, the highest values of C', ≥ 1 μFcm^{-1}, (c) correspond to the low frequency spike in (a) and are attributed to the electrode-sample interface at which, oxide ion blocking forms a double-layer capacitance. The curvature of the spike at lowest frequencies (a) indicates that the capacitance is not completely blocking, however, but is in parallel with a resistance that represents a combination of a small amount of electronic conduction through the sample and/or redox processes involved in charge transfer of oxygen across the electrode-sample interfaces. At higher temperatures, especially for x=0.15, Figure 4.S2, C' data show a poorly-resolved plateau around 10 μFcm^{-1} but continue to rise to ≥200

μFcm^{-1} at 0.1 Hz. In addition, low frequency Z^* plots, Figures 4.S1(d, e) show the emergence of a second arc in the low frequency part of the impedance response which indicates a more complex nature of the sample-electrode interface impedances and probably includes a Warburg diffusion impedance associated with diffusion of O_2 molecules through the metal electrode and towards/away from the interfaces.

Y' data show two overlapping plateaux at intermediate frequency of which the lower frequency plateau corresponds to the total conductivity Figure 4.5(d). At high frequencies, the onset of a power law dispersion is seen and is attributed to Jonscher Power Law behaviour which is a common feature of materials that are ionic and/or electronic hopping conductors.

Impedance data of x=0.30 and 0.45 were similar to those of x=0.15, but with two key differences, especially at higher temperatures where the low frequency impedance effects are seen more clearly, Figures 4.6, 4.S3 and 4.S5. First, the low frequency spike turned into a small arc for the composition of highest Y^{3+} content, x=0.45. This effect was much more noticeable than the changes in curvature seen with x=0.15. Second, with increasing Y^{3+} content, capacitance data, Figure 4.6(d), show a noticeable reduction in value at low frequencies, indicating that charge transfer at the double-layer interface is no longer predominant. This effect is interpreted as demonstrating the onset of electronic conduction with increasing Y^{3+} content in YSH and is similar to results reported for YSZ ceramics of high Y content [9].

From impedance data such as those shown in Figures 4.5 and 4.6 values for bulk, grain boundary and total conductivities were extracted and are shown as Arrhenius plots in Figure 4.7. In all three cases, the grain boundary resistance is much smaller than the bulk resistance and therefore the total conductivities in (a) approximate to the bulk conductivities. x=0.15 shows a higher conductivity, by ~ 1 order of magnitude, than 0.30, 0.45. The Arrhenius plots for bulk and total conductivities of 0.15 are non-linear (a), which is typical behaviour of yttria-stabilized zirconia, shown for YSZ08 in (a) for comparison [17]. The total conductivity decreases with x, as has been reported in the literature [13] and is attributed to oxide ions, especially for the lower x compositions. However, the similarity in Arrhenius plots of 0.30 and 0.45, (a), may be because the ionic conductivity decreases but electronic conductivity increases with x and the two effects largely cancel to give similar overall conductivities.

The grain boundary conductivities appear to be approximately one order of magnitude higher than the bulk conductivities for all three YSH compositions, (b,c). However, in order to

obtain true conductivities, they should be corrected for grain boundary geometry as follows. The correction of the grain boundary conductivities, σ_{gb}, can be done by:

$$\sigma_{gb} = \frac{1}{R_{gb}} \frac{C_b}{C_{gb}} \frac{d}{A} \quad (4.2)$$

where A, d, C_b and C_{gb} are the area, thickness, bulk capacitance and grain boundary capacitance. We can use values of plateau capacitances in plots such as Figure 4.S2, 4 and 6 to estimate grain boundary thicknesses. The capacitance values of plateau of x=0.15 that are attributed to grain boundaries are about two decades larger than bulk capacitances. Since the grain boundary conductivities are about one decade larger than the bulk conductivities, the net effect is that grain boundary conductivity is about one decade smaller than bulk conductivity, Figure 4.7d. For x = 0.30 and 0.45, the capacitance values of the plateau of x=0.30 and 0.45 that are attributed to grain boundaries are about ~one decade larger than bulk capacitances, so grain boundary conductivities are similar to those of bulk conductivities, Figure 4.7d. However, because the grain boundaries are thin, the bulk conductivities dominate the overall sample conductivities, as shown in the Arrhenius plot in Figures 4.7(a, b). We note that, for all three compositions, the grain boundary activation energy, E_{gb} is significantly greater than that of the bulk, E_b. The differences in resistivity of the two regions are not simply due to either differences in mobile carrier concentration, or to a constriction resistance model of the grain boundary resistance, [18, 19] therefore, but involve either a difference in mobility or a contribution from mobile carrier creation. This may be a consequence of small structural or compositional differences between grain interiors and grain boundaries, although there is no evidence of cation segregation from the EDX maps, Figure 4.4.

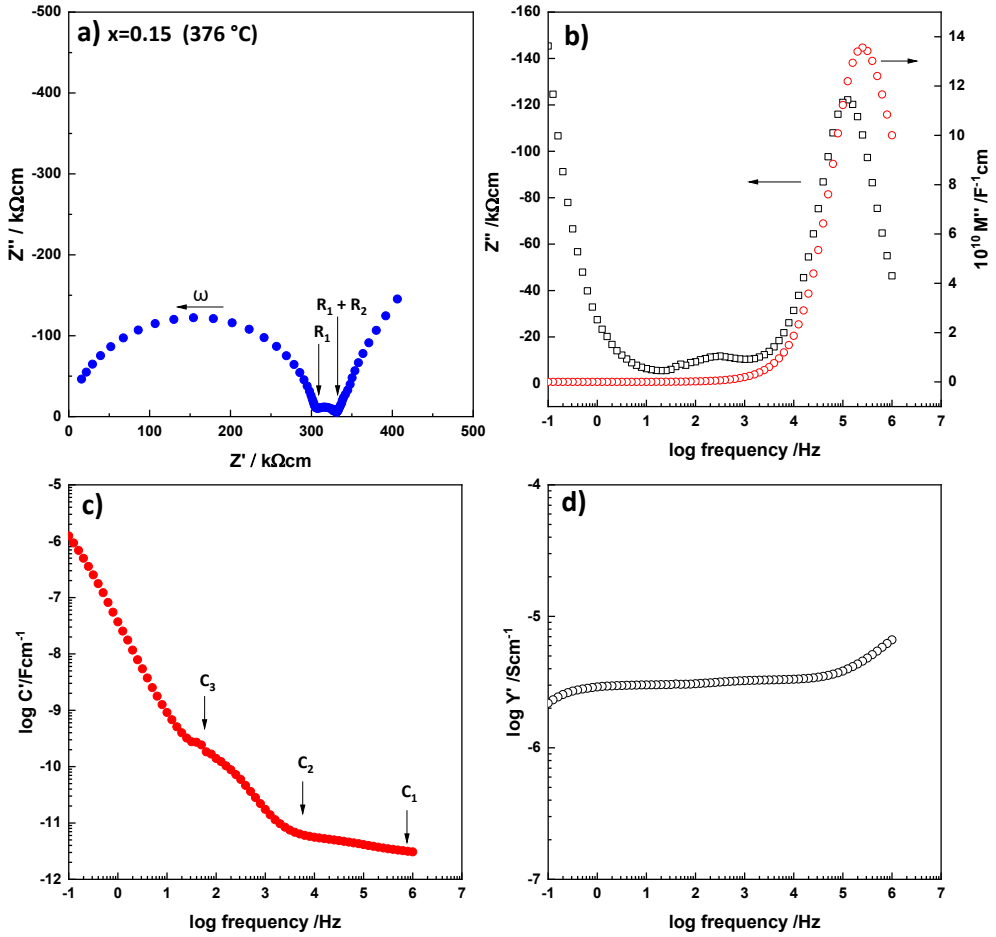

Figure 4.5 a) complex plane plot (Z*) and spectroscopic plots of b) Z''/ M'', c) C' and d) Y' of x=0.15 in air at 376 °C.

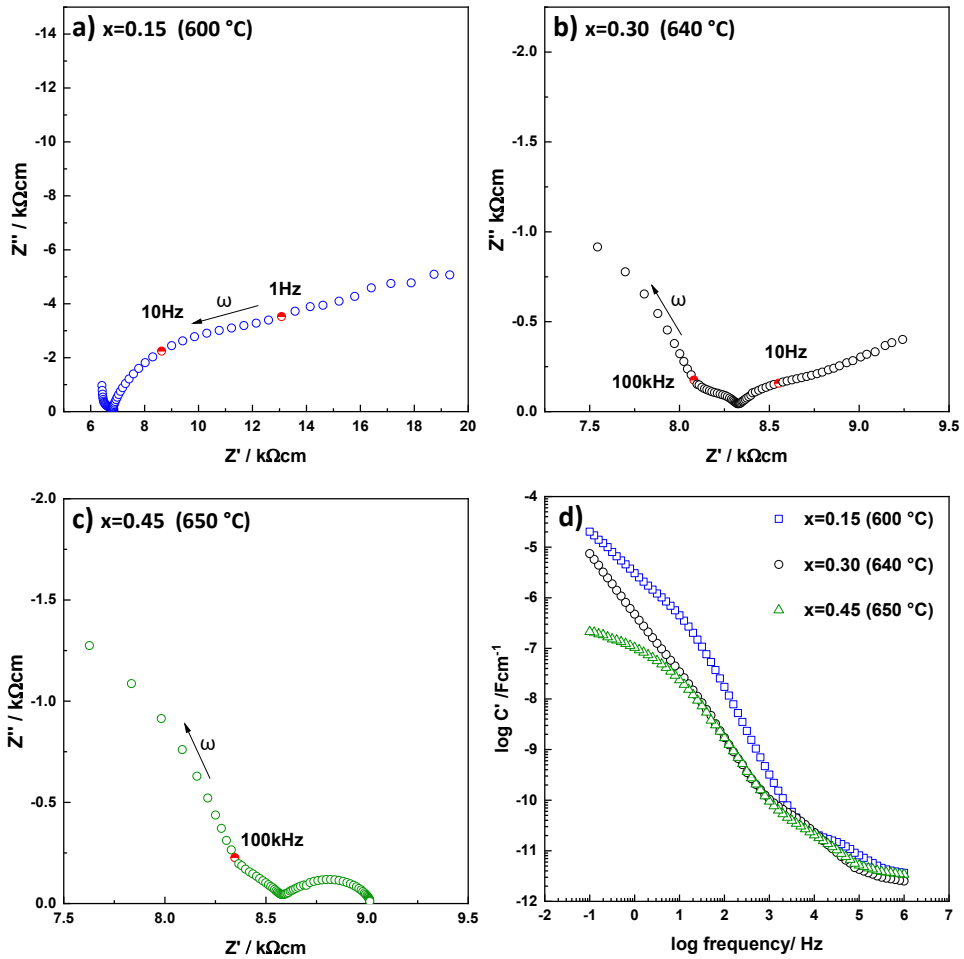

Figure 4.6 Complex plane plots (Z*) for a) x=0.15, b) x=0,30, c) x=0.45 and d) C' spectroscopic plots, measured in air.

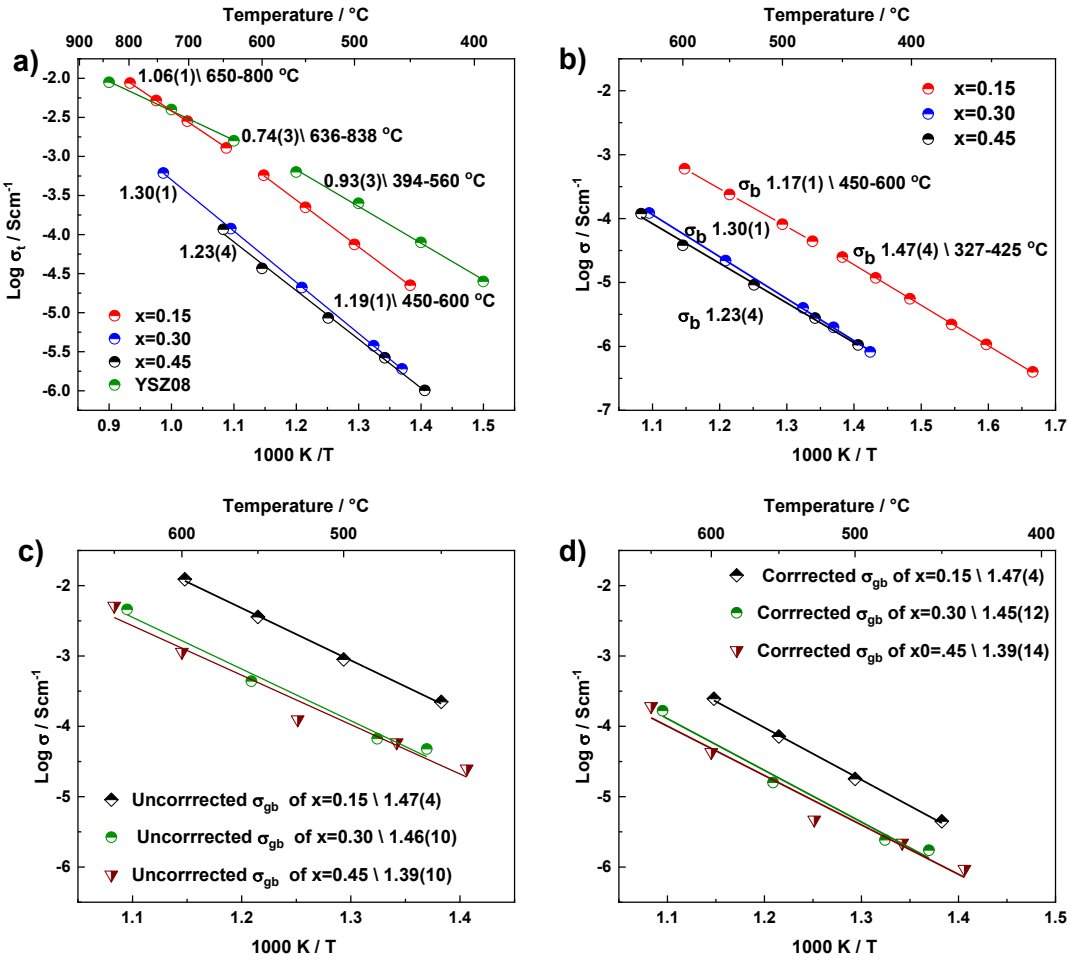

Figure 4.7 a) Arrhenius plots of total conductivity of x=0.15, 0.3 and 0.45 sintered at 1650-1750°C. Activation energies in eV are shown beside each data set. Data for YSZ08 sintered at 1550 °C for 2 h are included for comparison [17]. b,c) Arrhenius plots of bulk and grain boundary conductivities. Note; the gb data are not corrected for gb geometry. d) Arrhenius plots of corrected grain boundary conductivities for all compositions.

The effect of pO_2 on impedance data is shown in Figures 4.8 and 4.9. For all three compositions, it is clear that the bulk resistance is lower in O_2 than in N_2. This indicates that there is an electronic component of the overall conductivity since the level of oxide ion conductivity should be insensitive to pO_2. Further, the reduction in resistance with increasing pO_2 is indicative of *p*-type behaviour since holes are created by absorption and dissociation of oxygen molecules, given ideally as:

$$1/2O_2 + V_O^{\bullet\bullet} \rightarrow O_O^X + 2h^{\bullet} \qquad (4.3)$$

The electrode contact resistances decrease greatly with increasing pO_2, as shown by the decrease in size of the low frequency impedance arc, which reflects the involvement of oxygen molecules in reactions at the sample-electrode interfaces.

In order to obtain accurate resistance values, including for the grain boundary resistance, circuit fitting was carried out as follows. The chosen equivalent circuit that represents the complete range of impedance data is shown in Figures 4.8 and 4.9. It is the same as that proposed by recent accurate modelling of impedance data for YSZ and calcia-stabilized zirconia, CSZ [15, 16]. Assessment of the validity of the chosen circuit was performed in different ways: a) visual examination of experimental and fitted data, utilizing the presentation of data in various impedance formalisms, b) comparison of the fit residuals between experimental and calculated data, c) examination of the values of the fitted data and their temperature-dependence to determine whether they give realistic values for the electrical property characteristics of the sample.

The proposed circuit, Figure 4.8 (b,d), is composed of four components. First, a parallel combination of R_1, CPE_1 and C_1 to represent the bulk conductivity response which is also in parallel with C_0 and R_0 connected in series to model the dipole contribution to the *ac* conductivity. Second, a parallel combination of R_2 and CPE_2 that is attributed to the grain boundary impedance. The third and fourth components contain two parallel combinations, R_3-CPE_3 and R_4-CPE_4, connected in series to represent the sample-electrode impedance.

It was found that this circuit was a 'master circuit', parts of which fitted all the impedance data over a wide range of temperature. Since only a limited range of experimental frequencies was available, (0.1-10^6 Hz), the master circuit was not needed, or able, to fit all the data at every temperature. Nevertheless, each component in the circuit could be evaluated and component parameters provided for a range of temperatures. Fits are shown Figures 4.8, 4.9, S4.7-10. The residuals indicate good quality of fits, Figures 4.S7-10(d,h). In some cases, the fits are less good at high and low frequencies; this is attributed to the limited amount of data available at these temperatures to obtain accurate fits, as well as inaccuracies in experimental data at the frequency extremes. Fitted resistance values at two temperatures in both N_2 and O_2 are given in Tables 4.2 and 4.3; complete data sets are given in Tables 4.S1 and 4.S2.

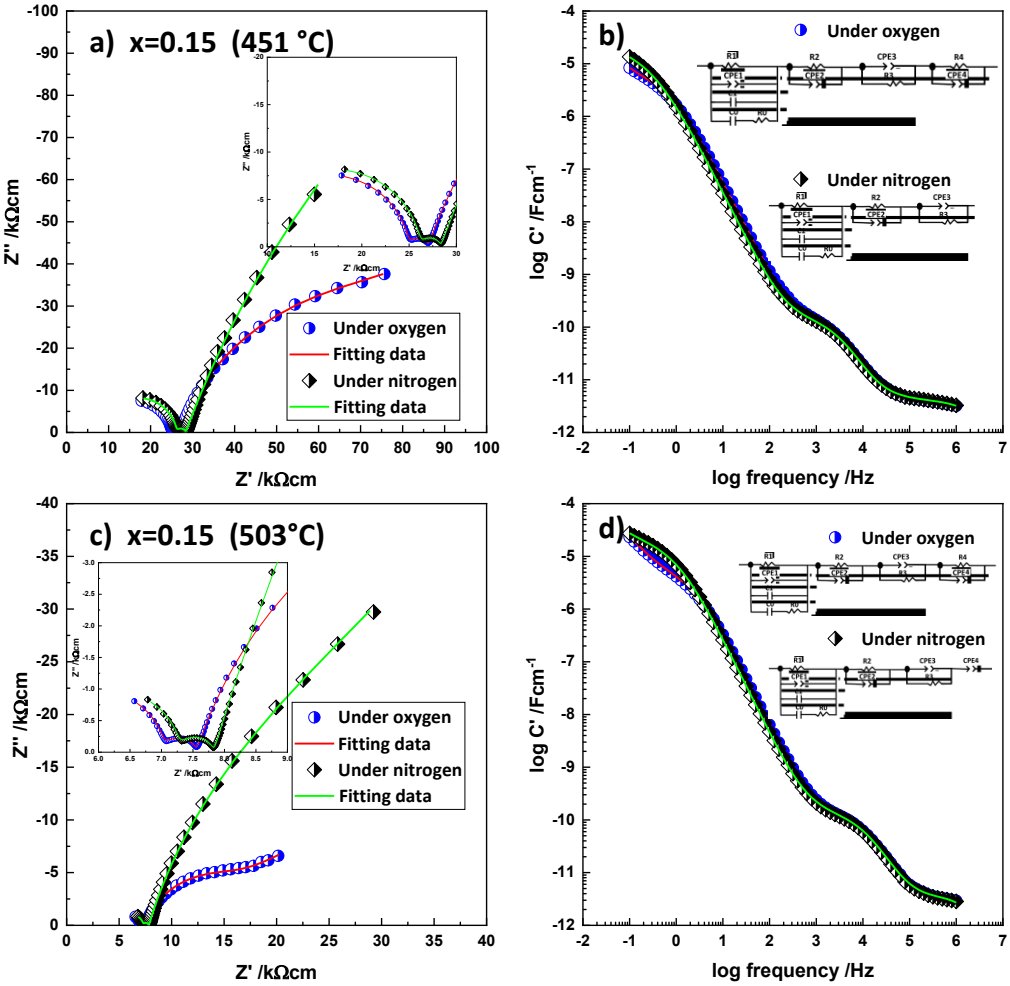

Figure 4.8 (a, c) Impedance complex plane plots, (b, d) C' spectroscopic plots of x=0.15 measured in dry N_2 and O_2 at 451 and 503 °C, respectively. Experimental data points and fits to the circuits are shown.

Table 4.2 Resistance values of x=0.15 in dry N_2 and O_2 at two temperatures.

	x=0.15 (451 °C /N_2)	x=0.15 (451 °C /O_2)	x=0.15 (503 °C /N_2)	x=0.15 (503 °C /O_2)
R_1 (kΩcm)	26.29(5)	25.09(2)	7.291(8)	7.046(6)
R_2 (kΩcm)	2.04(5)	1.96(2)	0.539(9)	0.506(7)
R_3 (kΩcm)	450(2)	77.8(4)	30(10)	8.27(6)
R_4 (kΩcm)	-------	63(13)	-------	31(2)

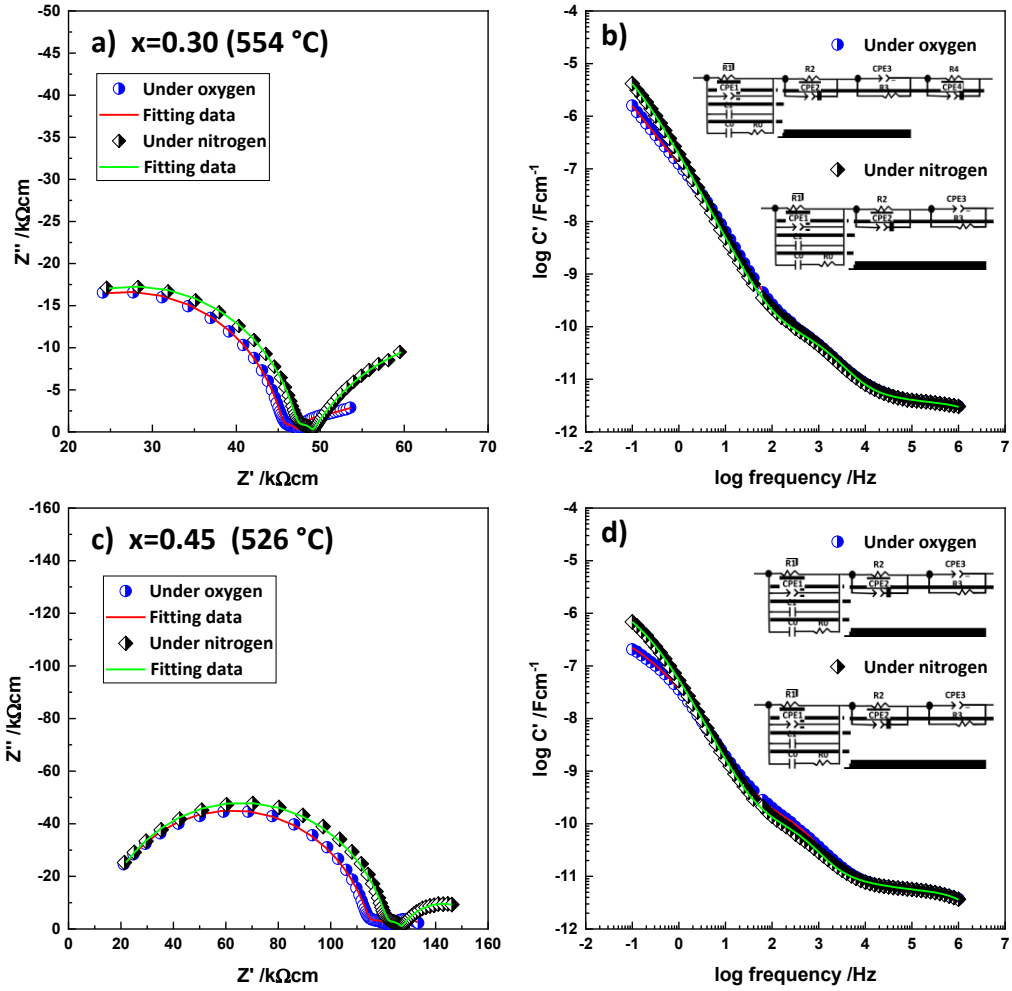

Figure 4.9 (a, c) Impedance complex plane plots, (b, d) C' spectroscopic plots for x=0.30, x=0.45 measured in dry N_2 and O_2 at 554 and 526 °C, respectively showing experimental data and fits.

Table 4.3 Resistance values of x=0.30, x=0.45 in dry N_2 and O_2 at two temperatures.

	x=0.30 (554 °C /N_2)	x=0.30 (554 °C /O_2)	x=0.45 (526 °C /N_2)	x=0.45 (526 °C /O_2)
R_1 (kΩcm)	47.40(3)	45.67(3)	122.2(1)	115.4(1)
R_2 (kΩcm)	1.65(3)	1.47(4)	4.6(2)	6.2(2)
R_3 (kΩcm)	40(1)	1.5(1)	32(1)	14.2(6)
R_4 (kΩcm)	-------	18(2)	-------	-------

Transport number measurements

Results of oxygen transport number measurements are shown for three temperatures in Table 4.4. The value of t_i is slightly less than unity for x=0.15, decreases with x at 800 °C, consistent with the pO_2 dependence of the conductivity data shown in Figures 4.8, 4.9 and Tables 4.2, 4.3 and is attributed to the onset of p-type electronic conduction. x=0.15 is therefore at the cross-over between the electrolytic and p-type domains under atmospheric conditions. Both R_1 and R_2 decrease with increasing pO_2, Table 4.2, and therefore, the conductivity Arrhenius plots for x=0.15, Figure 4.7, represent a combination of oxide ion and electronic conductivities. Similar effects are seen with x=0.30, 0.45; the low frequency impedance data also show increasing evidence of electronic conductivity, especially for x=0.45. We are unable to comment on the relative activation energies of oxide ion and electronic conduction. As far as we can tell, the two mechanisms of ionic and electronic conduction are entirely independent of each other. Transport measurements are likely to be influenced by ceramic microstructure, which may affect the amount of atmospheric oxygen that can be exchanged with the samples, as well as the different resistances that contribute to the overall electrical properties. We regard the data in Table 4.4 as indicative rather than quantitative, therefore.

Table 4.4 Oxygen ion transport number, t_i, for x=0.15, 0.30 and 0.45 from EMF measurements using N_2/air at the two electrodes

composition	t_{ion} (600 °C)	t_{ion} (700 °C)	t_{ion} (800 °C)
x=0.15	0.86	0.94	0.99
x=0.30	0.79	0.78	0.92
x=0.45	0.93	0.88	0.85

4.4 Discussion

YSH materials with a fluorite structure are majority oxide ion conductors with a small amount of *p*-type conductivity that is very dependent on atmosphere. Of the three compositions studied here, the oxide ion conductivity is greatest for x=0.15, similar to that reported previously [13]. The decrease in oxide ion conductivity at higher Y^{3+} contents is similar to that seen with YSZ compositions, which is attributed to increased trapping of the mobile oxide ion carriers in defect complexes [6, 9, 20, 21].

The onset of *p*-type conductivity with increasing Y^{3+} content is also similar to that seen with YSZ compositions [9]. The location of the holes in both systems is almost certainly on oxygen since the possibility of impurities such as Fe being present in both systems and to an extent that depends on Y^{3+} content, is most improbable. In addition, location of holes on Y or Hf, to take them above their usual charge states of Y^{3+} and Hf^{4+}, is most unlikely.

As proposed previously, [8, 9] holes appear to be located on under-bonded oxide ions that are surrounded by insufficient positive charge to fully stabilize the O^{2-} ion in the crystal lattice. Such under-bonded oxide ions in the bulk region are associated with the acceptor dopants, in this case Y^{3+}, which substitutes for Hf^{4+}. Charge compensation for the acceptor dopants involves creation of oxygen vacancies and these are able to absorb oxygen molecules from the surrounding atmosphere, thereby providing the mechanism for hole creation, equation (4.3). Additionally, at sample surfaces and interfaces such as grain boundaries, oxide ions may be under-bonded due to an incomplete coordination arrangement of surrounding cations. Some of the oxide ions, in both bulk and grain boundary regions, may ionise spontaneously giving rise to hole conductivity. They may also ionise easily in response to an increase in pO_2 [9] ,equation (4.3), or, as described in other systems, to the application of a *dc* bias [8, 22, 23].

These results raise an interesting question as to the intrinsic stoichiometry of materials such as YSH and YSZ since their oxygen content is variable, albeit by a small amount, depending on the atmospheric conditions. Oxygen non-stoichiometry in transition metal oxides is of course, commonplace and is associated with mixed oxidation states of the metal component. In the present case, by contrast, oxygen is the element that potentially, has a mixed oxidation state. These materials exhibit hopping, *p*-type semiconductivity and the only realistic location of holes is on oxygen since the cations that are present are already in their highest valence states, ie Hf^{4+}, Zr^{4+} and Y^{3+}; in addition, the holes are not delocalised in a band structure. The possibility of redox-active oxygen in oxides has not been considered seriously by most within the electroceramics and chemistry communities until the recent discoveries of battery charge / discharge mechanisms in certain Na and Li transition metal oxide cathodes for which the observed capacities could not be attributed to the transition metal component alone. Nowadays, there are many examples cited of anion redox activity in battery systems [24, 25].

The present materials have O^{2-} ions as their principal anions but a small amount of O^{-} ions can be created by reaction with atmospheric oxygen leading to oxygen redox activity. The

unavoidable conclusion, therefore, is that oxygen in oxides should not be regarded always as an inert packing anion but, in certain circumstances, it can be redox active. The classic ionic oxide Al_2O_3, provides a recent example of *p*-type conductivity that was also attributed to redox-active oxygen [26].

4.5 Conclusions

The *ac* impedance results of $Hf_{1-x}Y_xO_{2-x/2}$ (YSH, x= 0.15, 0.30 and 0.45) demonstrate clear evidence of oxide ion conduction with an inclined Warburg spike at low frequency and a capacitance value of $\geq 10^{-6}$ F/cm. Composition x=0.15 had a conductivity that was ~ 1 order of magnitude higher than that of x=0.30 and 0.45. The materials are foremost, oxide ion conductors but with increasing pO_2, become *p*-type mixed conductors. The increase in conductivity with increasing pO_2 is reversible and is attributed to oxygen absorption in the vacancies that are created by charge compensation on substituting Hf^{4+} by Y^{3+} together with the creation of holes on under-bonded oxide ions. The *p*-type semiconductivity is in parallel with the pre-existing oxide ion conduction. The YSH materials at high temperatures in air are, therefore, located just beyond the high pO_2 limits of the electrolytic domain. They represent the second known example of this effect in the family of stable, fluorite-based oxide ion conductors in which hole location on oxygen is responsible for the *p*-type behaviour and represent a practical limit on the possible application of such materials as solid electrolytes. The possibility of cross-over between electrolytic and *p*-type domains is well-recognised in the literature on oxides, but its origin, and especially the location of holes, has been discussed rarely, in contrast to the widely-studied onset of *n*-type behaviour that is observed at low pO_2 and associated with oxygen loss.

4.6 References

1. Hagenmuller, P. and W. Van Gool, *Solid electrolytes: general principles, characterization, materials, applications*. 2015: Elsevier.
2. Etsell, T. and S.N. Flengas, *Electrical properties of solid oxide electrolytes.* Chemical Reviews, 1970. **70**(3): p. 339-376.
3. Singhal, S.C. and K. Kendall, *High-temperature solid oxide fuel cells: fundamentals, design and applications*. 2003: Elsevier.
4. Tuller, H., *Ionic conduction and applications.* Springer Handbook of Electronic and Photonic Materials, 2017: p. 1-1.
5. West, A.R., *Solid state chemistry and its applications*. 2014: John Wiley & Sons.
6. Norberg, S.T., S. Hull, I. Ahmed, S.G. Eriksson, D. Marrocchelli, P.A. Madden, P. Li, and J.T. Irvine, *Structural Disorder in Doped Zirconias, Part I: The $Zr_{0.8}Sc_{0.2-x}Y_xO_{1.9}$ ($0.0 \leq x \leq 0.2$) System.* Chemistry of Materials, 2011. **23**(6): p. 1356-1364.
7. Kharton, V., F. Marques, and A. Atkinson, *Transport properties of solid oxide electrolyte ceramics: a brief review.* Solid State Ionics, 2004. **174**(1-4): p. 135-149.
8. Masó, N. and A.R. West, *Electronic conductivity in yttria-stabilized zirconia under a small dc bias.* Chemistry of Materials, 2015. **27**(5): p. 1552-1558.
9. Jovaní, M., H.c. Beltrán-Mir, E. Cordoncillo, and A.R. West, *Atmosphere-and Voltage-Dependent Electronic Conductivity of Oxide-Ion-Conducting $Zr_{1-x}Y_xO_{2-x/2}$ Ceramics.* Inorganic chemistry, 2017. **56**(12): p. 7081-7088.
10. Guo, M., N. Masó, Y. Liu, and A.R. West, *Electrical Properties and Oxygen Stoichiometry of $Ba_{1-x}Sr_xTiO_{3-\delta}$ Ceramics.* Inorganic chemistry, 2018. **57**(1): p. 64-71.
11. Masó, N., H. Beltrán, M. Prades, E. Cordoncillo, and A.R. West, *Field-enhanced bulk conductivity and resistive-switching in Ca-doped $BiFeO_3$ ceramics.* Physical Chemistry Chemical Physics, 2014. **16**(36): p. 19408-19416.
12. Courouau, J.-L., J. Fouletier, and M. Steil, *HfO_2-based electrolyte potentiometric oxygen sensors for liquid sodium.* Electrochimica Acta, 2020. **331**: p. 135269.
13. Schieltz, J.D., *"Electrolytic behavior of yttria and yttria stabilized hafnia"* in *Retrospective Theses and Dissertations*. 1970, Iowa State University.

14. Weyl, A. and D. Janke, *High-Temperature Ionic Conduction in Multicomponent Solid Oxide Solutions Based on HfO_2.* Journal of the American Ceramic Society, 1996. **79**(8): p. 2145-2155.
15. Vendrell, X. and A.R. West, *Electrical properties of yttria-stabilized zirconia, YSZ single crystal: local AC and long range DC conduction.* Journal of The Electrochemical Society, 2018. **165**(11): p. F966-F975.
16. Ramírez-González, J. and A.R. West, *Electrical properties of calcia-stabilised zirconia ceramics.* Journal of the European Ceramic Society, 2020.
17. Vendrell, X., D. Yadav, R. Raj, and A.R. West, *Influence of flash sintering on the ionic conductivity of 8 mol% yttria stabilized zirconia.* Journal of the European Ceramic Society, 2019. **39**(4): p. 1352-1358.
18. Bruce, P.G. and A. West, *The A-C Conductivity of Polycrystalline LISICON, $Li_{2+2x}Zn_{1-x}GeO_4$, and a Model for Intergranular Constriction Resistances.* Journal of The Electrochemical Society, 1983. **130**(3): p. 662.
19. Li, Y., M. Liu, J. Gong, Y. Chen, Z. Tang, and Z. Zhang, *Grain-boundary effect in zirconia stabilized with yttria and calcia by electrical measurements.* Materials Science and Engineering: B, 2003. **103**(2): p. 108-114.
20. Marrocchelli, D., P.A. Madden, S.T. Norberg, and S. Hull, *Structural Disorder in Doped Zirconias, Part II: Vacancy Ordering Effects and the Conductivity Maximum.* Chemistry of Materials, 2011. **23**(6): p. 1365-1373.
21. Arachi, Y., H. Sakai, O. Yamamoto, Y. Takeda, and N. Imanishai, *Electrical conductivity of the ZrO_2–Ln_2O_3 (Ln= lanthanides) system.* Solid State Ionics, 1999. **121**(1-4): p. 133-139.
22. Vendrell, X. and A.R. West, *Induced p-type semiconductivity in yttria-stabilized zirconia.* Journal of the American Ceramic Society, 2019. **102**(10): p. 6100-6106.
23. Prades, M., N. Masó, H. Beltrán, E. Cordoncillo, and A.R. West, *Field enhanced bulk conductivity of $BaTiO_3$: Mg ceramics.* Journal of Materials Chemistry, 2010. **20**(25): p. 5335-5344.
24. Okubo, M. and A. Yamada, *Molecular orbital principles of oxygen-redox battery electrodes.* ACS applied materials & interfaces, 2017. **9**(42): p. 36463-36472.
25. Sudayama, T., K. Uehara, T. Mukai, D. Asakura, X.-M. Shi, A. Tsuchimoto, B.M. de Boisse, T. Shimada, E. Watanabe, and Y. Harada, *Multiorbital bond formation for stable*

oxygen-redox reaction in battery electrodes. Energy & Environmental Science, 2020. **13**(5): p. 1492-1500.

26. Ramírez-González, J. and A.R. West, *Electrical properties of Mg-doped and Mg, Si co-doped alumina.* Journal of the European Ceramic Society, 2021. **41**(6): p. 3512-3519.

Supplementary data

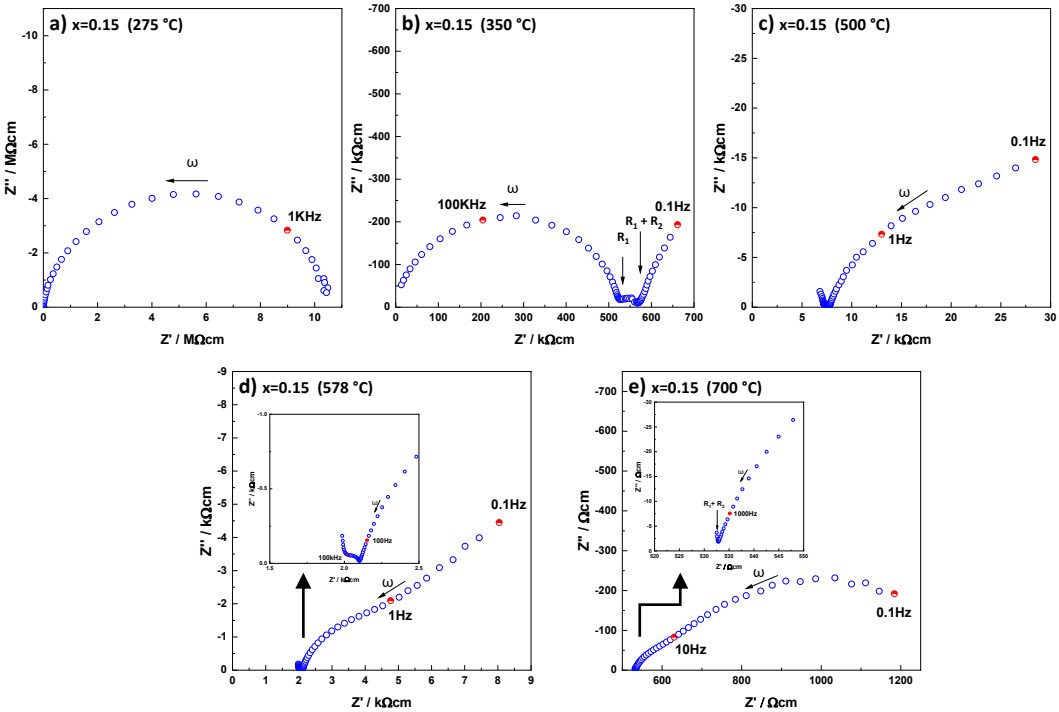

Figure 4.S1 (a-e) Typical complex plane plot (Z*) of x=0.15 at different temperatures.

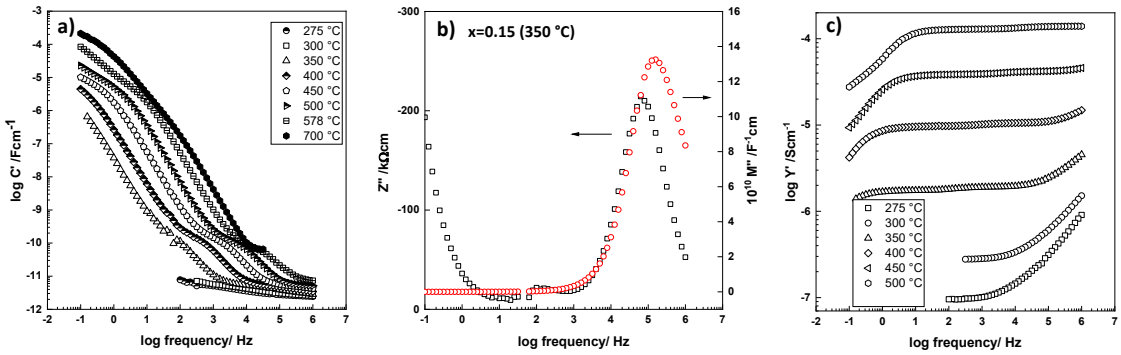

Figure 4.S2 a) C' spectroscopic plot, b) Z''/ M'' spectroscopic plots and c) Y' spectroscopic plot of x=0.15 at different temperatures.

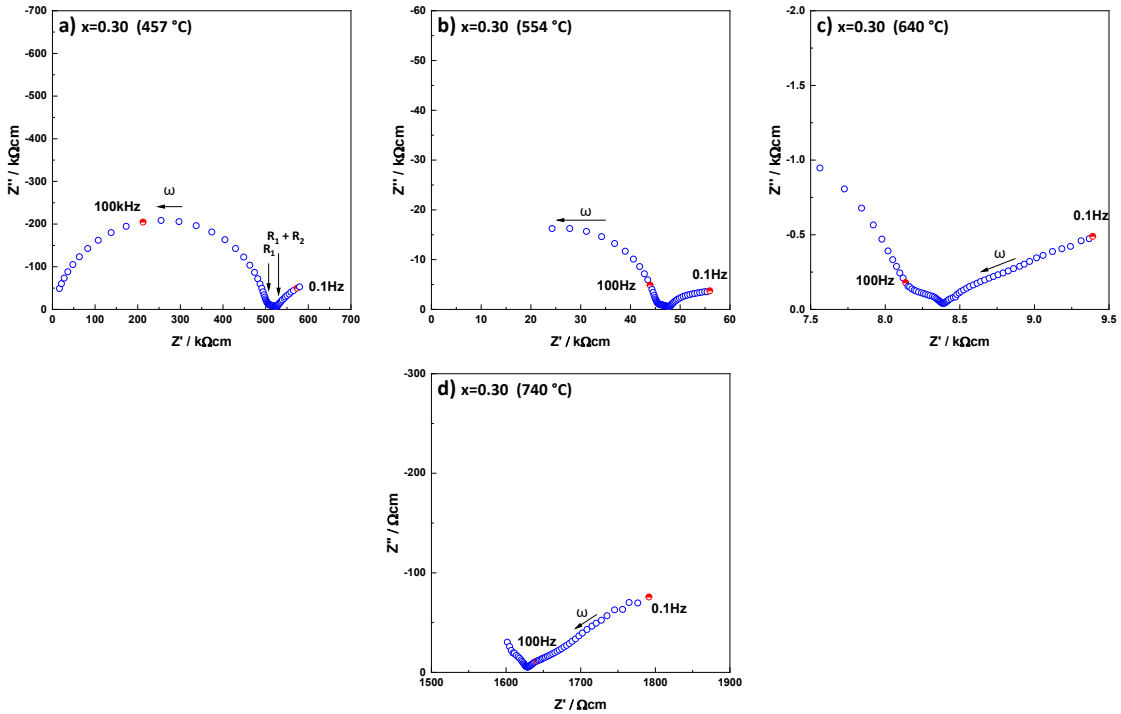

Figure 4.S3 (a-d) Typical complex plane plot (Z*) of x=0.30 at different temperatures.

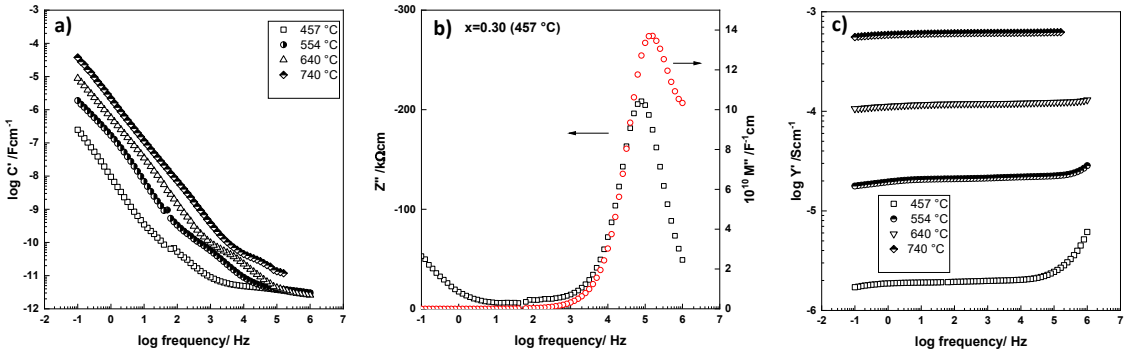

Figure 4.S4 a) C' spectroscopic plot, b) Z''/ M'' spectroscopic plots and c) Y' spectroscopic plot of x=0.30 at different temperatures.

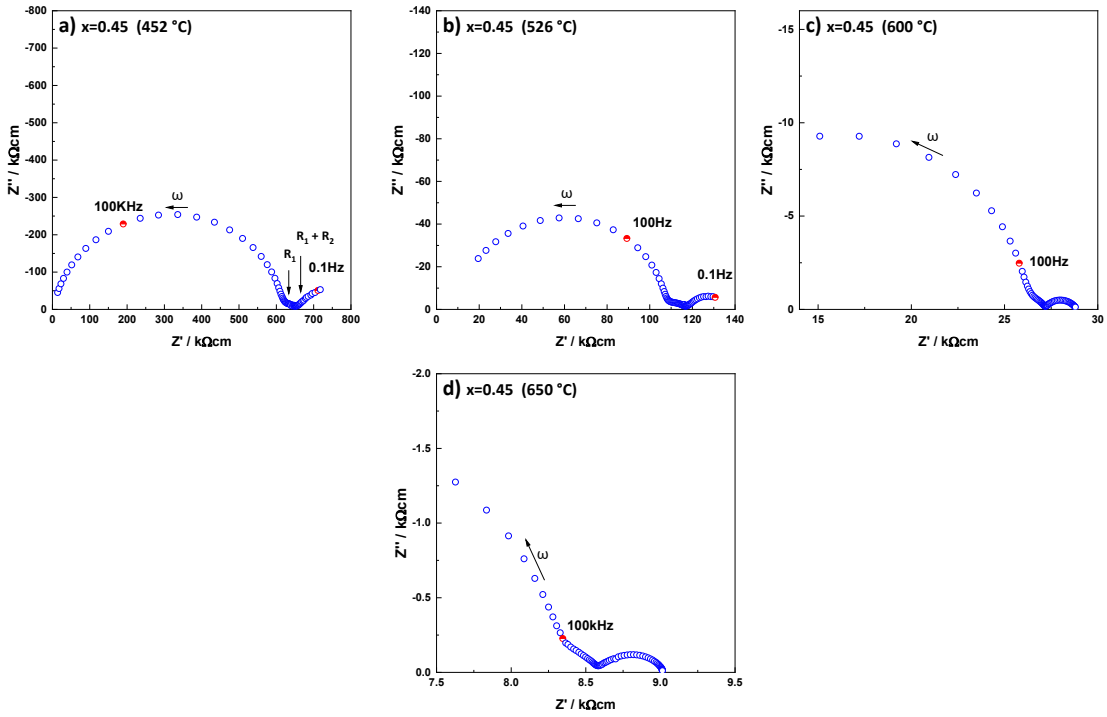

Figure 4.S5 (a-d) Typical complex plane plot (Z*) of x=0.45 at different temperatures.

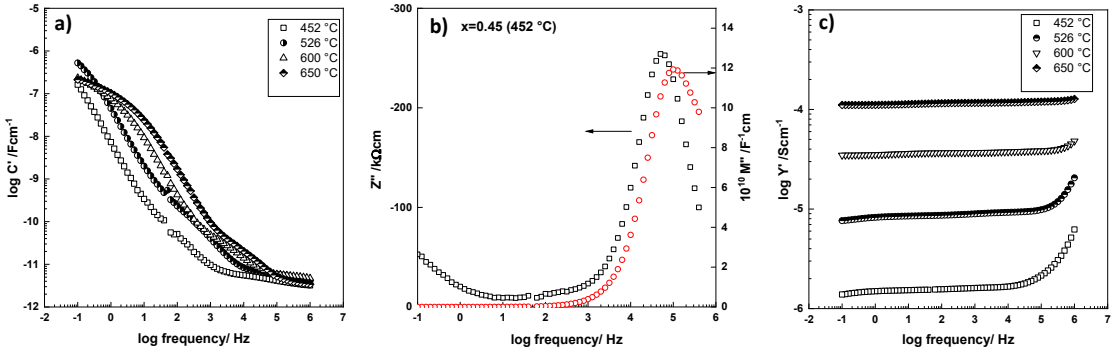

Figure 4.S6 a) C' spectroscopic plot, b) Z''/ M'' spectroscopic plots and c) Y' spectroscopic plot of x=0.45 at different temperatures.

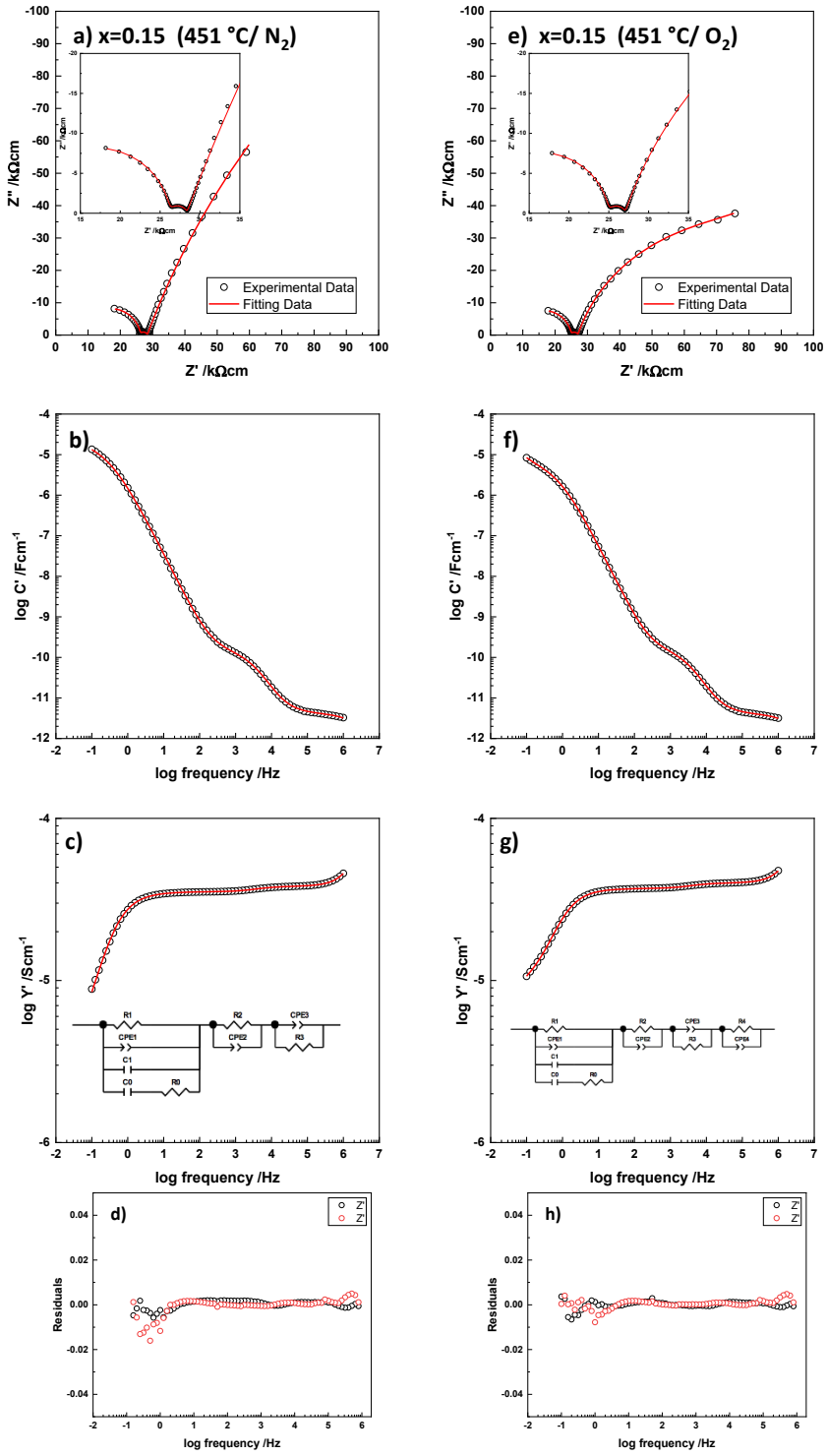

Figure 4.S7 Impedance spectra for x=0.15 measured in dry N_2 and O_2 at 451 °C. Experimental and fitted data to the chosen circuit for (a, e) Z* plots, (b, f) C' spectroscopic plots, (c, g) Y' spectroscopic plots, (d, h) Impedance residuals.

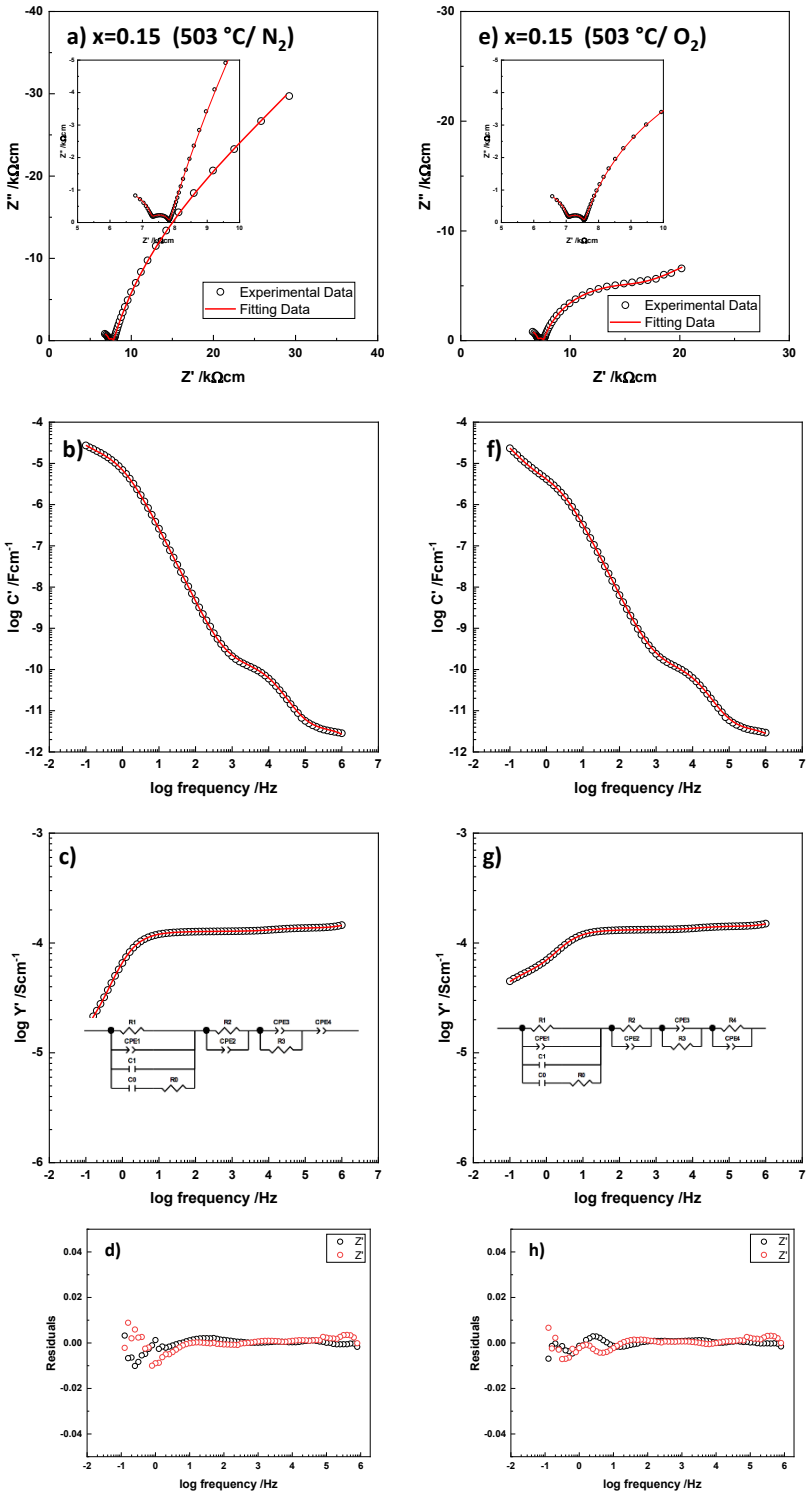

Figure 4.S8 Impedance spectra for x=0.15 measured in dry N_2 and O_2 at 503 °C. Experimental and fitted data to the chosen circuit for (a, e) Z* plots, (b, f) C' spectroscopic plots, (c, g) Y' spectroscopic plots, (d, h) Impedance residuals.

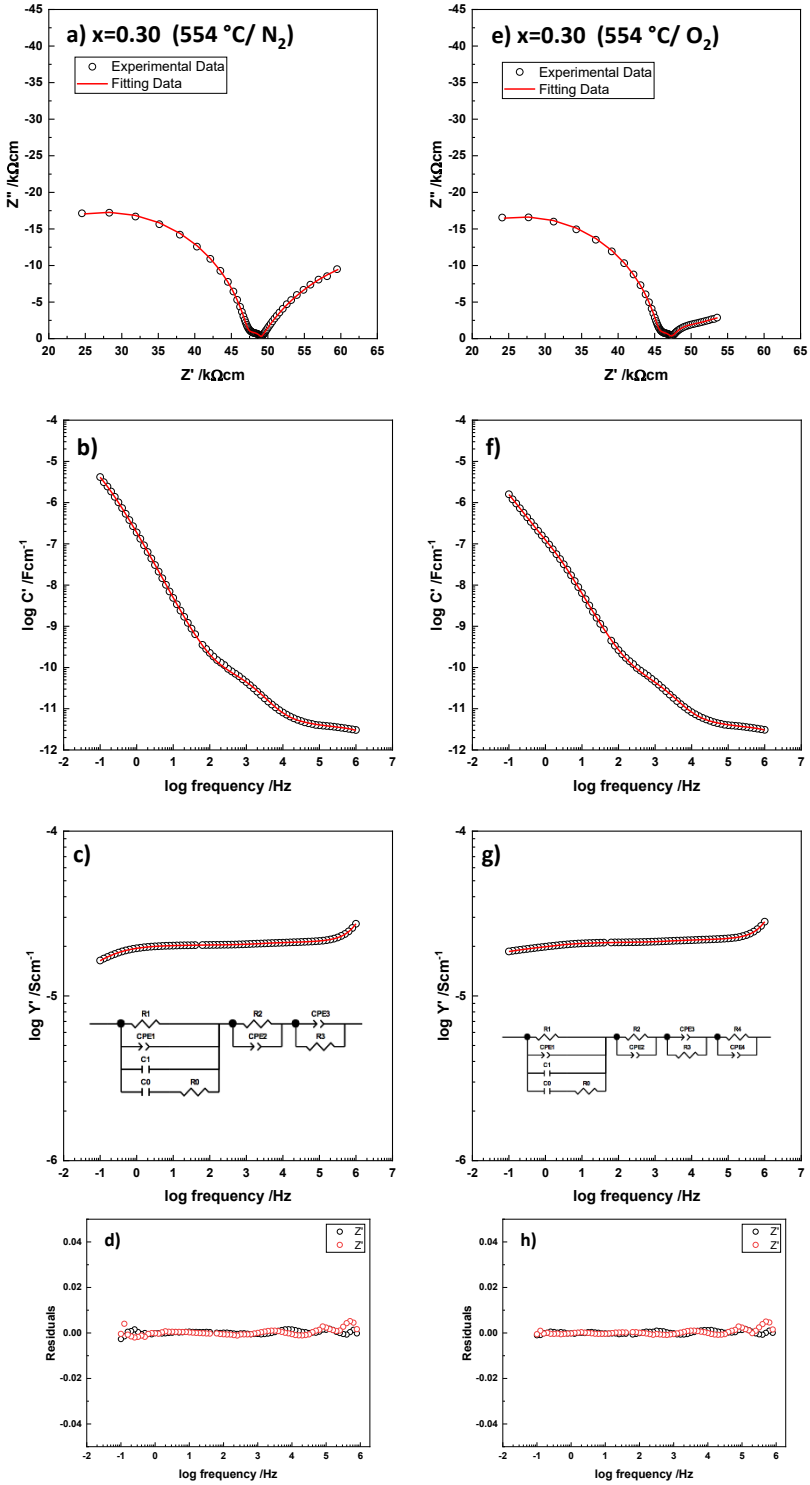

Figure 4.S9 Impedance spectra for x=0.30 measured in dry N_2 and O_2 at 554 °C. Experimental and fitted data to the chosen circuit for (a, e) Z* plots, (b, f) C' spectroscopic plots, (c, g) Y' spectroscopic plots, (d, h) Impedance residuals.

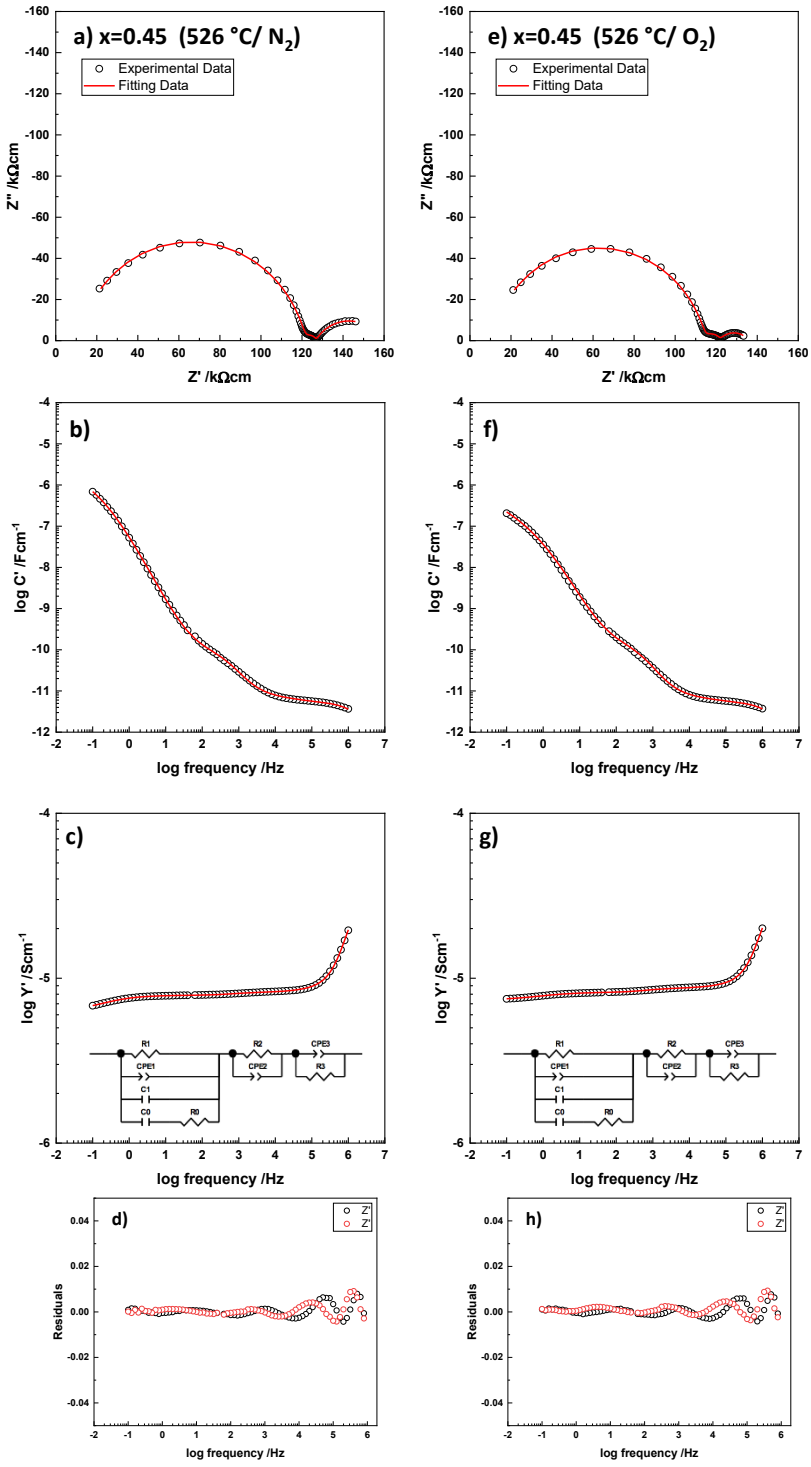

Figure 4.S10 Impedance spectra for x=0.45 measured in dry N_2 and O_2 at 526 °C. Experimental and fitted data to the chosen circuit for (a, e) Z* plots, (b, f) C' spectroscopic plots, (c, g) Y' spectroscopic plots, (d, h) Impedance residuals.

Table 4.S1 Fitted parameters of x=0.15 measured in dry N_2 and O_2 at two different temperatures.

	X=0.15 (451 °C /N_2)	X=0.15 (451 °C /O_2)	X=0.15 (503 °C /N_2)	X=0.15 (503 °C /O_2)
R_1 (kΩcm)	26.29(5)	25.09(2)	7.291(8)	7.046(6)
A_1 (Scm^{-1} rad^{-n})	8(1)E-11	7.5(5)E-11	1E-9(fixed)	1E-9(fixed)
n_1	0.71(fixed)	0.71(fixed)	0.46(fixed)	0.46(fixed)
C_1 (Fcm^{-1})	1E-12(fixed)	1E-12(fixed)	1E-12(fixed)	1E-12(fixed)
C_0 (Fcm^{-1})	1.9(1)E-12	1.91(7)E-12	2.23(6)E-12	2.28(5)E-12
R_0 (kΩcm)	47(4)	51(2)	49(2)	44(2)
R_2 (kΩcm)	2.04(5)	1.96(4)	0.539(9)	0.506(7)
A_2 (Scm^{-1} rad^{-n})	1.21(9)E-7	1.16(4)E-7	1.39(7)E-7	1.39(5)E-7
n_2	0.83(fixed)	0.84(fixed)	0.84(fixed)	0.84(fixed)
A_3 (Scm^{-1} rad^{-n})	2.017(7)E-5	1.292(8)E-5	4.0(8)E-5	2.58(2)E-5
n_3	0.774(2)	0.792(2)	0.79(1)	0.839(2)
R_3 (kΩcm)	450(20	77.8(4)	30(10)	8.27(6)
R_4 (kΩcm)	-------	63(13)	-------	31(2)
A_4 (Scm^{-1} rad^{-n})	-------	0.00016(fixed)	9(3)E-5	0.00016(fixed)
n_4	-------	1.165(fixed)	0.8(1)	0.68(1)

Table 4.S2 Fitted parameters of x=0.30 and x=0.45 measured in dry N_2 and O_2 at two different temperatures.

	X=0.30 (554 °C /N_2)	X=0.30 (554 °C /O_2)	X=0.45 (526 °C /N_2)	X=0.45 (526 °C /O_2)
R_1 (kΩcm)	47.40(3)	45.67(3)	122.2(1)	115.4(1)
A_1 (Scm^{-1} rad^{-n})	7.6(2)E-11	7.4(2)E-11	1.04(2)E-10	1.08(2)E-10
n_1	0.71(fixed)	0.71(fixed)	0.71(fixed)	0.71(fixed)
C_1 (Fcm^{-1})	1E-12(fixed)	1E-12(fixed)	1E-12(fixed)	1E-12(fixed)
C_0 (Fcm^{-1})	1.59(3)E-12	1.65(2)E-12	2.71(3)E-12	2.70(3)E-12
R_0 (kΩcm)	50.8(9)	47.8(8)	49.1(6)	48.4(6)
R_2 (kΩcm)	1.65(3)	1.47(4)	4.6(2)	6.2(2)
A_2 (Scm^{-1} rad^{-n})	3.6(2)E-7	3.4(2)E-7	2.2(2)E-7	1.7(1)E-7
n_2	0.78(fixed)	0.78(fixed)	0.83(fixed)	0.83(fixed)
A_3 (Scm^{-1} rad^{-n})	7.39(2)E-5	7.4(7)E-5	3.18(7)E-5	2.8(1)E-5
n_3	0.662(5)	0.88(4)	0.68(2)	0.62(3)
R_3 (kΩcm)	40(1)	1.5(1)	32(1)	14.2(6)
R_4 (kΩcm)	-------	18(2)	-------	-------
A_4 (Scm^{-1} rad^{-n})	-------	0.00016(fixed)	-------	-------
n_4	-------	0.44(2)	-------	-------

Chapter 5: Resistive-switching in yttria-stabilised hafnia ceramics

5.1 Introduction

There is much current interest in resistive switching, RS, phenomena in thin film devices for memristive applications [1]. An essential feature of these devices appears to be the creation of nano-dimensional conducting filaments on application of a small voltage during a preforming stage. These filaments break and reform during subsequent switching [1,2]. Resistive switching may occur by other mechanisms, including the well-known temperature-induced, metal-insulator Verwey transition in magnetite and VO_2 that is associated with structural changes at a crystallographic phase transition [2-6].

Thin films of pure and doped HfO_2 have received much attention recently because of their ferroelectric and resistive-switching behaviour [7, 8]. RS has been demonstrated in several metal oxides including NiO, TiO_2, HfO_2, ZrO_2, Al_2O_3, and Nb_2O_5 [5, 9] and a common characteristic is that RS occurs in nanometer-thick films and devices. The mechanism of RS is often attributed to the electromigration of either oxygen vacancies or metal cations such as Cu or Ag. These mobile species can join up to form a conductive pathway between opposite electrodes and the forming / breaking of these conducting pathways leads to resistive switching [10-12].

In bulk ceramics, a different type of switching of Ca-doped $BiFeO_3$ at modest temperatures was induced by application of a small *dc* voltage. It was not associated with a crystallographic transition and the resulting high conductivity ON state was isotropic, which excluded the possibility of a switching mechanism based on the making and breaking of conducting filaments [13]. Here in this chapter, resistive switching is reported at high temperatures in bulk ceramics of oxide ion conducting, yttria-stabilised hafnia, YSH; it is the second example of RS in bulk ceramics. This is not associated with a phase transition and occurs in materials that are electronically insulating when prepared by standard synthesis and processing procedures in air. An essential preforming step appears to be the field-induced generation of bulk electronic conductivity at opposite electrodes associated with two carriers, holes and electrons; oxygen exchange with the surrounding atmosphere is also important and, in

combination with application of a bias, leads to creation of a *p-i-n* junction whose forming and breaking is responsible for subsequent resistive switching.

5.2 Experimental procedures

Pellets of compositions $Hf_{1-x}Y_xO_{2-x/2}$: x=0.15, 0.30 and 0.45 with gold electrodes, were prepared, as described previously in chapter 4 [14]. For impedance spectroscopy (IS) measurements, gold electrodes were pasted on opposite pellet faces, dried at 850 °C for 2 h and the pellets loaded into a conductivity jig, placed inside a tube furnace and IS measurements made using either a Modulab XM Solartron analyser over the range 0.01 Hz – 1 MHz or an Agilent 4249A Precision Impedance Analyser, frequency range 40 Hz-1 MHz for IS measurements at the same time as a *dc* voltage was applied

5.3 Results and discussion

Typical IS data of x=0.15, 0.30 and 0.45 are shown in chapter 4 (Figure 4.S1-6). Three main components are apparent in the impedance complex plane plots and assigned, with decreasing frequency, to bulk, grain boundary and sample-electrode impedances. This is confirmed by capacitance, C' plots obtained using the same data sets which show a limiting high frequency capacitance plateau, an intermediate frequency inflection and a limiting low frequency plateau of approximate values 2 $pFcm^{-1}$, 100 $pFcm^{-1}$ and 300 μFcm^{-1}, respectively. The high value of the sample-electrode capacitance indicates that the samples are primarily oxide ion conductors [14].

The total conductivity of x=0.15 as a function of voltage at two temperatures, 457 and 501 °C and in three different atmospheres, O_2, air and N_2 is shown in Figure 5.1. Although these are total conductivities, the impedance complex plane plots of x=0.15 show that at lower temperatures (see previous chapter), the total conductivity is dominated by the bulk conductivity and therefore the changes seen in Figure 5.1 also approximate to bulk conductivity changes. The total conductivity–electric field profile, Figure 5.1, had the same general appearance in all six datasets. The conductivity was voltage-independent initially but then increased rapidly, associated with the onset of electronic conduction, before undergoing a sharp increase by 1.5 to 2.5 orders of magnitude to reach a steady ON state after which no further conductivity increase occurred. At each temperature, the magnitude of the conductivity increase and the steady state value was greatest in N_2 and least in O_2; also the

voltage at which switching occurred was lowest in N_2 and highest in O_2. On decreasing the applied voltage, the high conductivity state was retained to lower applied voltages, leading to hysteresis loops followed by a sudden return to the original conductivity, OFF state.

In all six cases, transition to the ON state was accompanied by a temperature rise of about 8 °C which was reversed on return to the OFF state; the temperature increase, measured by a thermocouple in close proximity to the sample, is attributed to Joule heating caused by reduction in sample resistance without change in the applied voltage. The initial conclusion from these results is, therefore, that the bulk impedance of x=0.15 undergoes a reversible, resistive switching transition at high temperatures and that oxygen partial pressure, pO_2 in the atmosphere is a critical variable in the parameters that control the transition.

Recording photos of x=0.15 pellet at 573 °C, before, during and after application of an electric field of 131 Vcm^{-1} showed that x=0.15 pellet gave a flash luminescence along with a ~two order of magnitude reduction in resistivity under application of the electric field. The flash luminescence event occurred when the sample reached the lower resistance state and disappeared when the sample was in the higher resistance state, Figure 5.2. This flash of the whole pellet indicates that the RS behaviour in YSH ceramics is related to the bulk effect and not associated with filamentary conductive paths and structural changes.

Further indication of the effect of pO_2 for x=0.15 was shown from the time dependence of resistance data with a voltage close to, but initially below, the OFF-ON switching voltage, in the same three atmospheres and at two temperatures, 501 and 531 °C, Figure 5.3. At 501 °C, a small conductivity increase occurred in O_2, but then remained constant in the OFF state. In air and N_2, however, the sample switched to the ON state but slowly, over a period of 5-10 mins; the highest ON state conductivity was obtained in N_2. At a somewhat higher temperature, 531 °C, the sample switched rapidly to the ON state in all three atmospheres but additional time was required to achieve a steady ON state, especially in N_2. A time-dependence was also seen on removing the dc bias; in air and O_2, the resistance increased to its ground state very rapidly but a few minutes were required to achieve this in N_2. There is some scatter and variation in the final state conductivities with the bias removed which may be caused by the time taken for the sample temperature to adjust to a lower value on effective removal of the Joule heating. These various time-dependent and atmosphere-dependent results indicate further that sample-oxygen exchange, in both directions, is a major factor in controlling the voltage-dependent conductivity.

Other compositions (x=0.30 and x=0.45) showed similar behaviour to those obtained in x=0.15. However, Figure 5.4. x=0.45 showed a resistive switching behaviour under just N_2 atmosphere. This can be due to that Y-rich YSH (x=0.45) has less oxygen content and for this reason under O_2 and air atmosphere, the sample needs to more applied voltages to lose oxygen.

The identity of the charge carriers was determined by a combination of IS measurements in atmospheres of different pO_2 and with different *dc* bias applied. A key representative result is shown in Figure 5.5, with interpretation based on the strategy that the effect of increasing pO_2 was either to create holes by absorption, dissociation and ionisation of oxygen according to, ideally:

$$1/2O_2 \rightarrow O^{2-} + 2h^{\bullet} \qquad (5.1)$$

or to trap electrons by:

$$1/2O_2 + 2e^{-} \rightarrow O^{2-} \qquad (5.2)$$

In this way, the distinction between extrinsic p and n carriers was determined, depending on whether the resistance decreased or increased with changing pO_2. From Figure 5.5 (a, c and e), the resistance of x=0.15, 0.30 and 0.45 decreased in O_2 at 500, 661 and 700 °C with a field of 39, 67 and 100 Vcm^{-1}, respectively, indicating *p*-type behaviour. On increasing the bias to 49, 77 and 112 Vcm^{-1} (b, d and f), there was a small decrease in resistance in O_2 but a much greater decrease in N_2, indicating a change to predominantly *n*-type behaviour This means that the carriers responsible for the conductivity are predominantly *p*-type at low field but switch to *n*-type at higher field. Both of these changes occur in the presence of oxide ion conduction which is the main conduction mechanism in the absence of an applied bias.

The presence of *p*-type conductivity and its field-induced increase has been observed previously in yttria-doped zirconia ceramics [15-17] similar to the present YSH material and in acceptor-doped $BaTiO_3$ ceramics such as $BaTi_{1-x}Mg_xO_{3-x}$,[18] both of which have oxygen vacancy creation as the main charge compensation mechanism on substitution of the lower valence cations, Y^{3+} for Zr^{4+} and Mg^{2+} for Ti^{4+}, respectively. The *p*-type conductivity was attributed to the creation of holes on oxide ions by the idealised reaction:

$$O^{2-} \rightarrow O^{-} + e^{-} \qquad (5.3)$$

This reaction occurs with underbonded oxide ions in the vicinity of the dopant cations. The liberated electrons are trapped at the positive electrode and the holes created on oxygen become the main electronic current carrier and are located initially near the ceramic/positive electrode interface, Figure 5.6A.

Equation (5.3) represents the first step in the ionisation of O^{2-} ions.

The presence of *n*-type conductivity is widely observed in materials that lose a small amount of oxygen at high temperatures by double ionisation of oxide ions according to:

$$O^{2-} \leftrightarrow 1/2O_2 + 2e^- \qquad (5.4)$$

It appears that a similar reaction to (5.4) occurs at higher bias fields, leading to charge injection at the negative electrode, Figure 5.6B. In order to account for the resistive switching, an *n-i-p* junction is thereby created that has an *i* region in the ceramic interior. The effect of increasing applied bias, especially in atmospheres of low pO_2, is to increase the amount of oxygen loss, inject more electrons at the negative electrode, increase the thickness of the *n*-type region and cause breakdown of the *n-i-p* junction, Figure 5.6C; breakdown is reversible on removing the source of electrons in the *n*-type region, leading to recovery of the original resistance.

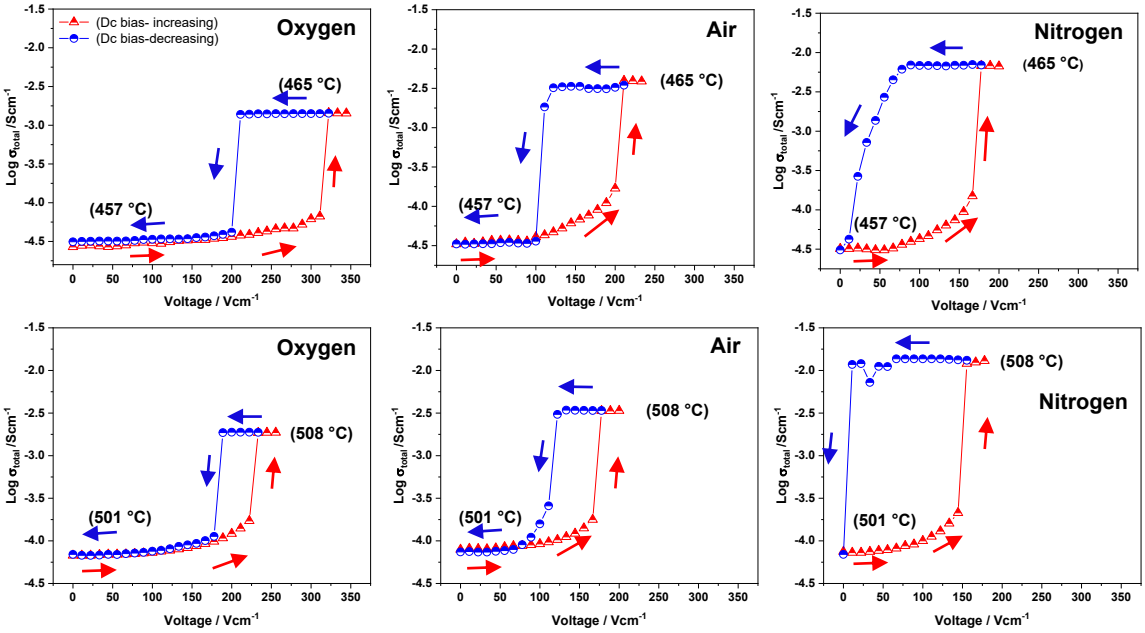

Figure 5.1 Total conductivity of x=0.15 after reaching a steady state against applied voltage at 457 °C and 501°C with the application of different pO_2.

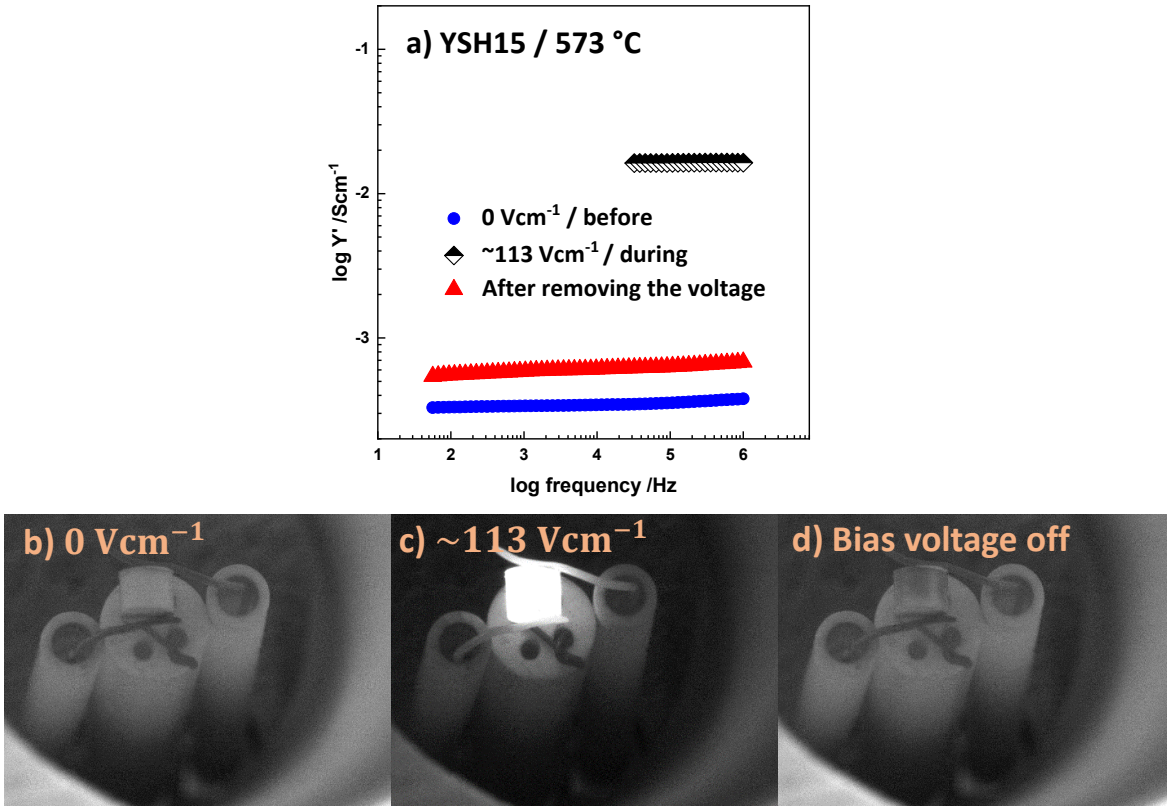

Figure 5.2 a) Spectroscopic plot of admittance of x=0.15 before, during applying a voltage and after removing a voltage. Images of x=0.15 pellet b) before, c) during applying a voltage and d) after removing a voltage

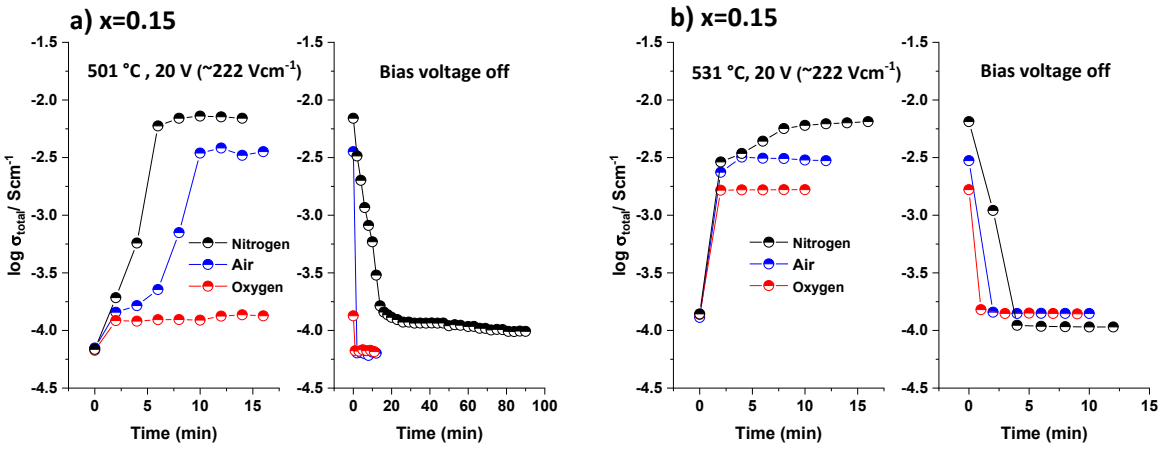

Figure 5.3 Total conductivity of x=0.15 vs time on applying and after removing a voltage a) at 501 °C b) at 531 °C.

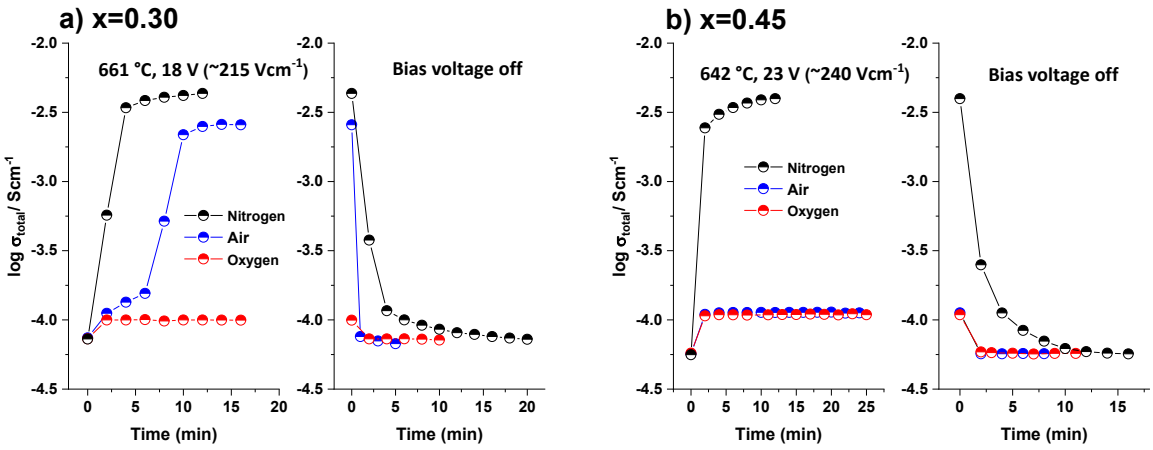

Figure 5.4 Total conductivity vs time on applying and after removing a voltage of a) x=0.30 at 661° C b) x=0.45 at 642 °C.

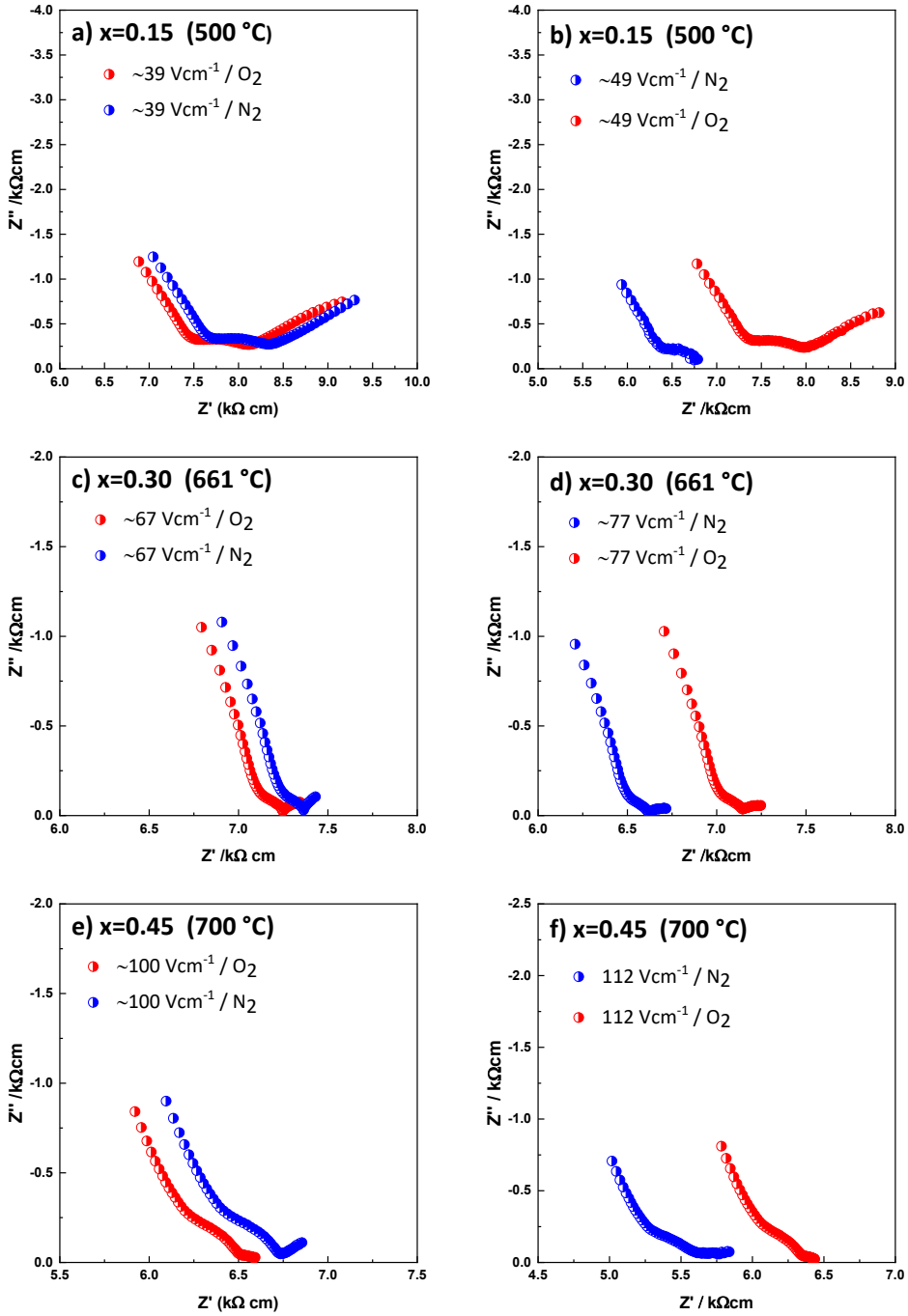

Figure 5.5 Impedance complex plane plots for YSH ceramics measured in dry O_2 and N_2 after applying a small voltage of a, b) 39 Vcm^{-1}, 49 Vcm^{-1} for x=0.15 at 500 °C, c, d) 67 Vcm^{-1}, 77 Vcm^{-1} for x=0.30 at 661 °C e, f) 100 Vcm^{-1}, 112 Vcm^{-1} for x=0.45 at 700 °C. With applying a fixed voltage, the measurements were taken in dry O_2 and then the atmosphere was changed to dry N_2.

A) STAGE (1)

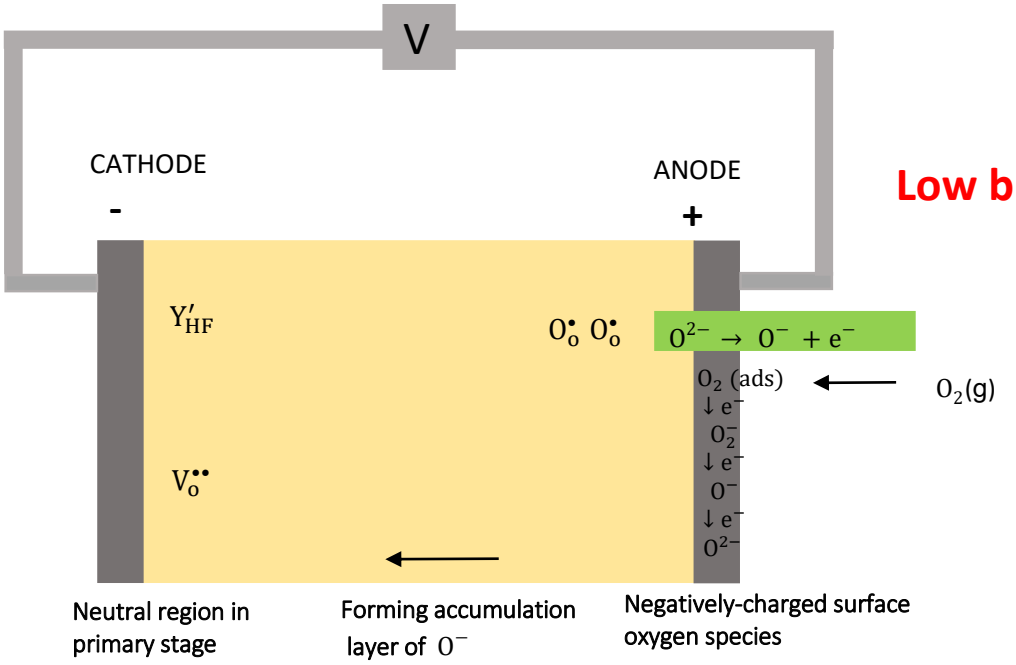

B) STAGE (2)

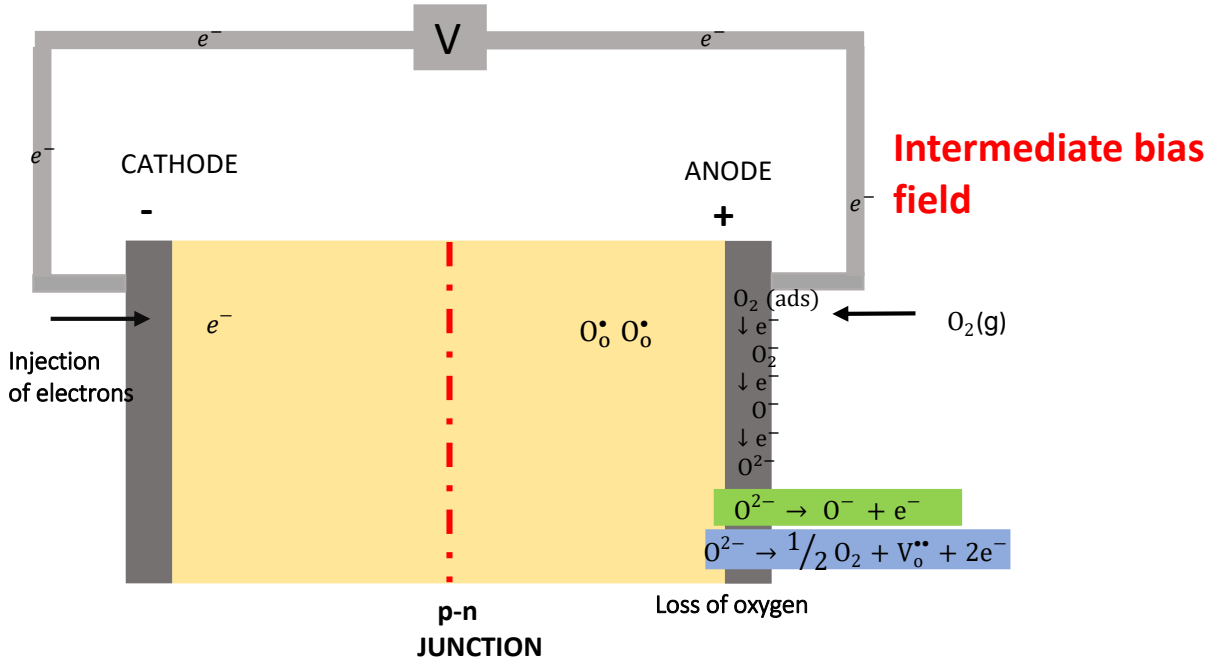

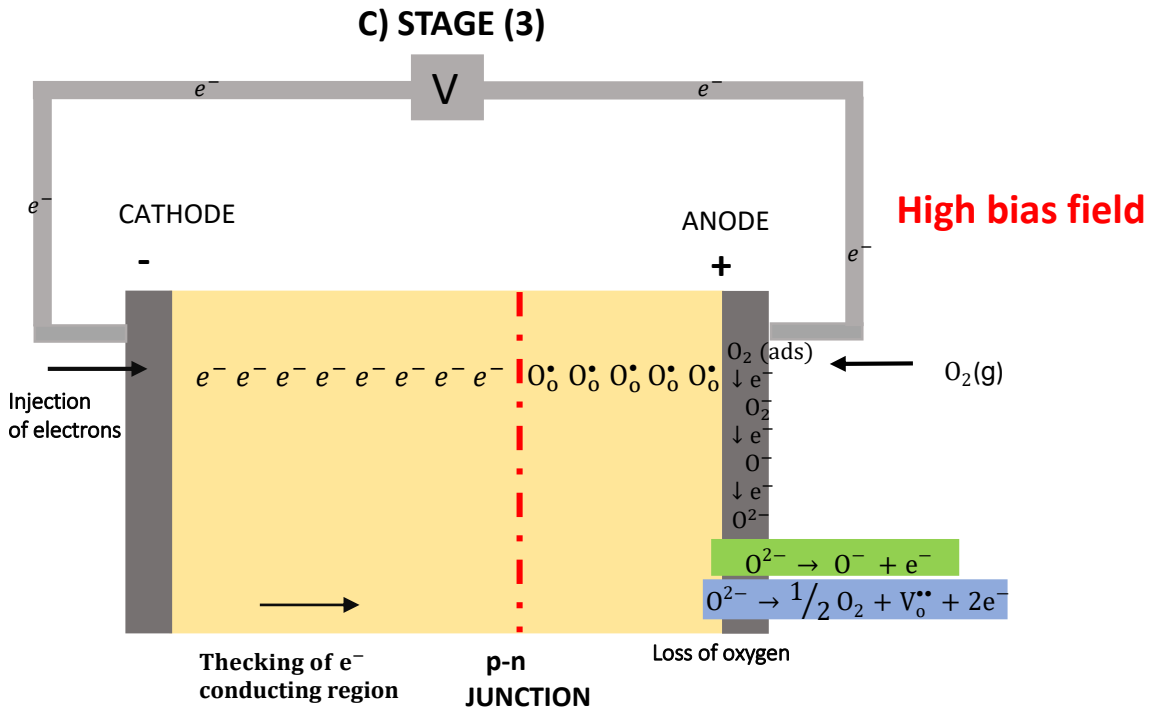

Figure 5.6 Illustrated model to the proposed mechanism of a dc bias-dependent conductivity of YSH ceramics at a) low and b) intermediate and C) high bias field.

The resistive switching in YSH ceramics is clearly electronic in origin. Creation of *n*-type conductivity in ceramics is very well-known, especially that associated with oxygen loss at high temperatures, but an additional mechanism is required to explain the low field *p*-type conductivity and reversible switching observed here. Oxygen in oxides is traditionally assigned the oxidation state -2 and two-electron transfer is therefore involved in sample-atmosphere interactions that involve exchange between O^{2-} ions in a solid and O_2 molecules in the gas phase. In order to account for *p*-type hopping conductivity in materials such as YSH ceramics, it is necessary to determine the location of the holes and, given the absence of cations that can be ionised to a higher oxidation state, the inevitable conclusion is that holes are located on singly-ionised oxygen, as O^- ions. Acceptor-doped materials such as YSH, YSZ [16] and Mg-doped $BaTiO_3$[18] all have oxygen vacancies as the principal charge compensation mechanism and contain under-bonded oxide ions which are in the vicinity of the acceptor dopants. Under-bonded oxide ions have a reduced ionisation potential, may therefore ionise readily and undergo redox reaction with O_2 molecules from the atmosphere. This leads to O^- ions that occupy the lattice vacancies and are the source of resulting *p*-type conductivity:

$$O^{2-} + V_o^{\bullet\bullet} + 1/2O_2 \leftrightarrow 2O^{-} \qquad (5.5)$$

Formation of O^- ions accounts for the spontaneous *p*-type conductivity in YSH, as shown by the variation of conductivity with pO_2 in the surrounding atmosphere [14] which increases under *dc* bias at the positive electrode as reaction (5.5) is driven to the right. At higher bias, double ionisation of oxide ions to O_2 gas occurs, reaction (5.4). This leads to *n*-type behaviour as a consequence of charge injection at the negative electrode, facilitated by oxide ion migration away from the negative electrode under *dc* bias.

We therefore attribute the effect of *dc* bias to generation of holes at one electrode and electrons at the other electrode which are separated by an insulating region that does not have an excess of charge carriers. The effect of time under *dc* bias is to cause thickening of the *p*- and *n*-type regions until they are in direct contact and responsible for the observed resistive switching. The *p*-*i*-*n* structure that forms under *dc* bias is a non-equilibrium state and on removal of the *dc* bias, reactions 5.4 and/or 5.5 are displaced to the left hand side, leading to reformation of the *p*-*i*-*n* structure.

5.4 Conclusions

YSH is the second example, of which we are aware, of low field resistive switching in a bulk ceramic. YSH shows a reversible increase in conductivity, by 1-3 orders of magnitude, on application of a small *dc* voltage. Oxygen partial pressure, pO_2, plays a major role in the resistive-switching behaviour. A mechanism for RS is presented based on the effect of dc bias on the conductivity of YSH ceramics. At low voltage, the increase in conductivity is attributed to the introduction of *p*-type behaviour at the positive electrode. The *p*-type behaviour is attributed to single ionisation of under-bonded O^{2-} ions and creation of holes, located on oxygen as O^- ions. At higher voltage, *n*-type behaviour is attributed to oxygen loss by double ionisation of oxide ions and injection of electrons at the negative electrode, facilitated by field-induced migration of oxide ions towards the positive electrode. *p*- and *n*-type regions are therefore created at opposite electrodes. This leads to creation of a *p*-*i*-*n* structure that, on breakdown, gives an enhancement in the conductivity that is reversible on removal of the bias.

5.5 References

1. Sun, W., B. Gao, M. Chi, Q. Xia, J.J. Yang, H. Qian, and H. Wu, *Understanding memristive switching via in situ characterization and device modeling.* Nature communications, 2019. **10**(1): p. 1-13.
2. Wang, Z., H. Wu, G.W. Burr, C.S. Hwang, K.L. Wang, Q. Xia, and J.J. Yang, *Resistive switching materials for information processing.* Nature Reviews Materials, 2020. **5**(3): p. 173-195.
3. Ielmini, D. and H.-S.P. Wong, *In-memory computing with resistive switching devices.* Nature electronics, 2018. **1**(6): p. 333-343.
4. Sawa, A., *Resistive switching in transition metal oxides.* Materials today, 2008. **11**(6): p. 28-36.
5. Waser, R. and M. Aono, *Nanoionics-based resistive switching memories.* Nature Materials, 2007. **6**(11): p. 833-840.
6. Jeong, D.S., R. Thomas, R. Katiyar, J. Scott, H. Kohlstedt, A. Petraru, and C.S. Hwang, *Emerging memories: resistive switching mechanisms and current status.* Reports on Progress in Physics, 2012. **75**(7): p. 076502.
7. Banerjee, W., A. Kashir, and S. Kamba, *Hafnium Oxide (HfO_2) – a Multifunctional Oxide: A Review on Prospect and Challenges of Hafnium Oxide in Resistive Switching and Ferroelectric Memories.* Small, 2022.
8. Schroeder, U., C.S. Hwang, and H. Funakubo, *Ferroelectricity in Doped Hafnium Oxide: Materials, Properties and Devices*. 2019: Woodhead Publishing.
9. Kim, K.M., D.S. Jeong, and C.S. Hwang, *Nanofilamentary resistive switching in binary oxide system; a review on the present status and outlook.* Nanotechnology, 2011. **22**(25): p. 254002.
10. Waser, R., R. Dittmann, G. Staikov, and K. Szot, *Redox-based resistive switching memories–nanoionic mechanisms, prospects, and challenges.* Advanced materials, 2009. **21**(25-26): p. 2632-2663.
11. Jung, Y.C., S. Seong, T. Lee, S.Y. Kim, I.-S. Park, and J. Ahn, *Improved resistive switching characteristics of a Pt/HfO_2/Pt resistor by controlling anode interface with forming and switching polarity.* Applied Surface Science, 2018. **435**: p. 117-121.

12. Lin, K.-L., T.-H. Hou, J. Shieh, J.-H. Lin, C.-T. Chou, and Y.-J. Lee, *Electrode dependence of filament formation in HfO2 resistive-switching memory.* Journal of Applied Physics, 2011. **109**(8): p. 084104.
13. Masó, N., H. Beltrán, M. Prades, E. Cordoncillo, and A.R. West, *Field-enhanced bulk conductivity and resistive-switching in Ca-doped $BiFeO_3$ ceramics.* Physical Chemistry Chemical Physics, 2014. **16**(36): p. 19408-19416.
14. Alotaibi, M., L. Li, and A.R. West, *Electrical properties of yttria-stabilised hafnia ceramics.* Physical Chemistry Chemical Physics, 2021. **23**(45): p. 25951-25960.
15. Jovaní, M., H. Beltrán-Mir, E. Cordoncillo, and A.R. West, *Field-induced pn transition in yttria-stabilized zirconia.* Scientific Reports, 2019. **9**.
16. Masó, N. and A.R. West, *Electronic conductivity in yttria-stabilized zirconia under a small dc bias.* Chemistry of Materials, 2015. **27**(5): p. 1552-1558.
17. Vendrell, X. and A.R. West, *Induced p-type semiconductivity in yttria-stabilized zirconia.* Journal of the American Ceramic Society, 2019. **102**(10): p. 6100-6106.
18. Prades, M., N. Masó, H. Beltrán, E. Cordoncillo, and A.R. West, *Field enhanced bulk conductivity of $BaTiO_3$: Mg ceramics.* Journal of Materials Chemistry, 2010. **20**(25): p. 5335-5344.

Chapter 6: Impedance analysis of $Hf_{1-x}Zr_xO_2$ thin-films

6.1 Introduction

Ferroelectric behaviour in fluorite –structure oxides was first found in Si doped HfO_2 thin films. Böscke et al. [1] reported the formation of an orthorhombic phase which crystallised under mechanical encapsulation of top and bottom electrodes and had a remanent polarization of 10 $\mu C/cm^2$. A number of studies were then conducted, doping several elements into HfO_2 such as Gd, Al, Y, Zr [2-4]. In recent years, studies have sought to investigate the generic principles of ferroelectricity and phase stability of HfO_2. In this chapter, the aim was to analyse electrical properties of ferroelectric $Hf_{1-x}Zr_xO_2$ (x=0, 0.4, 0.5, 0.6 and 1) thin films and films of x=0.5 exposed to different ozone dose times using impedance spectroscopy. The films were provided by the research group of Uwe Schroeder, Dresden, Germany, as we were interested to compare our impedance results on bulk doped hafnia ceramics with those of thin films. Our results on the temperature-dependent permittivity of the films lead to a joint publication [5].

6.2 Experimental procedure

Samples of three different configurations of $Hf_{1-x}Zr_xO_2$ thin films were provided by Professor Uwe Schroeder, Namlab gGmbH, Dresden, Germany. The first set of samples are three $Hf_{0.5}Zr_{0.5}O_2$, HZO, thin films with thickness 10 nm and had been exposed to O_3 with a different dose time, 0.1, 0.5 and 1 sec, Figure 6.1a. The second set are five $Hf_{1-x}Zr_xO_2$ (x=0, 0.4, 0.5, 0.6 and 1) thin films, but contained only one layer of top electrode: p-Si/TiN/$Hf_{1-x}Zr_xO_2$/TiN, Figure 6.1c. The third is one HfO_2-SiO_2 thin film sample consisting of a bilayer of HfO_2 with thickness 45 nm and SiO_2 with thickness 80 nm: p-Si/TiN/HfO_2/SiO_2/TiN, Figure 6.1b. Samples with three different multilayer configurations are shown in Figure 6.1 and listed in Table 6.1

For the first set of samples, metal-insulator-metal devices containing $Hf_{0.5}Zr_{0.5}O_2$ (HZO) films were fabricated on p-Si substrates, by the collaborators, using the following steps [5, 6]:

I. TiN bottom electrodes with thickness of ~10 nm were deposited on the entire surface of p-Si substrates by physical vapour deposition (PVD, sputter deposition).
II. $Hf_{0.5}Zr_{0.5}O_2$ layers were deposited on top of the TiN layer by atomic layer deposition (ALD) using $Hf[N(CH_3)(C_2H_4)]_4$ and $CpZr[N(CH_3)_2]_3$ precursors as Zr and Hf sources in a

Routh&Rau ALD tool. Ozone, O_3, was applied as the source of oxygen at deposition temperature of 280 °C.

III. TiN top electrodes with thickness of ~10 nm were deposited on entire surface of $Hf_{0.5}Zr_{0.5}O_2$ layers by physical vapour deposition (PVD, sputter deposition).

IV. A post metallisation annealing, PMA, treatment at 600 °C in N_2 atmosphere for 20 seconds was performed in order to obtain the ferroelectric structure of $Hf_{0.5}Zr_{0.5}O_2$ [6].

V. Ti and Pt dots with diameter 200 µm and 10/25 nm thick for Ti and Pt, respectively, were deposited via electron beam evaporation through a shadow mask to obtain capacitor structure.

VI. Uncovered TiN top electrode was exposed to chemical-wet etching using SC1 (H_2O, H_2O_2 and NH_3 in the ratio 50:2:1) to remove TiN top electrode around the dots. $Hf_{1-x}Zr_xO_2$ was confirmed to be stable (not affected) through this process.

For the second set of samples, $Hf_{1-x}Zr_xO_2$ (x=0, 0.4, 0.5, 0.6 and 1) films, Figure 6.1c and for the third set, HfO_2-SiO_2 bilayer films, Figure 6.1b were prepared by a similar procedure, but minimizing the number of electrode layers by excluding steps V and IV (i.e. without Ti/Pt top electrodes).

Impedance spectroscopy (IS) measurements were carried out using Agilent E4980A instrumentation over the frequency range 20 Hz-1 MHz in static air and a Solartron SI 1260 impedance analyser (Solartron Analytical Ltd, Farnborough, UK) over the frequency range 0.01 Hz-1 MHz for measurements under variable oxygen partial pressure. The applied ac voltage for all samples was 100 mV. A geometric factor was not applied to the impedance data because of uncertainty over the actual geometry of the HZO component of the multilayer devices. The devices were used as-received from Germany without further treatment.

For dielectric permittivity measurements, thin film samples were placed between two Pt electrodes in a pressure-contact jig and measured at 5 fixed frequencies of 1, 10, 100, 250 kHz and 1 MHz. Capacitance data were recorded in air every minute from room temperature to 600 °C with heating rate 1 °C min^{-1} using an LCR meter (Model 4284A, Hewlett Packard, HP). The dielectric permittivity, ε_r was calculated using $e_r = C/e_0$, where e_0 is the permittivity of free space, 8.854×10^{-14} Fcm^{-1} and C is the measured capacitance.

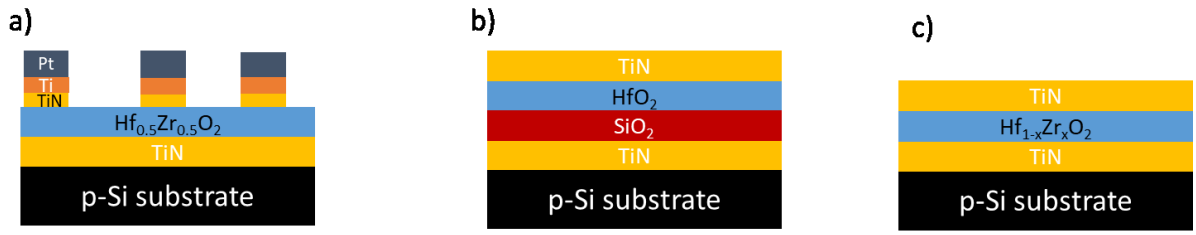

Figure 6.1 Multiple layers and electrode structure of the capacitors for a) HZO-0.1 s, HZO-0.5 s and HZO-1 s and b) HfO_2-SiO_2 and c) $Hf_{1-x}Zr_xO_2$ (x=0, 0.4, 0.5, 0.6 and 1).

Table 6.1 Thin-film samples and their labels.

Label	Sample configuration
HZO-0.1 s	p-Si/TiN/$Hf_{0.5}Zr_{0.5}O_2$/TiN/Ti/Pt with 0.1 s O_3 dose time
HZO-0.5 s	p-Si/TiN/$Hf_{0.5}Zr_{0.5}O_2$/TiN/Ti/Pt with 0.5 s O_3 dose time
HZO-1 s	p-Si/TiN/$Hf_{0.5}Zr_{0.5}O_2$/TiN/Ti/Pt with 1 s O_3 dose time
$Hf_{1-x}Zr_xO_2$ (x=0, 0.4, 0.5, 0.6 and 1)	p-Si/TiN/$Hf_{1-x}Zr_xO_2$/TiN/Ti/Pt
HfO_2-SiO_2	p-Si/TiN/SiO_2 80nm/HfO_2 45nm/TiN

6.3 Results

This chapter contains sets of results for a) impedance of HZO thin films with different ozone, O_3, dose time (HZO-0.1 s, HZO-0.5 s, and HZO-1 s) b) impedance of five sets of films $Hf_{1-x}Zr_xO_2$ (x=0, 0.4, 0.5, 0.6 and 1) which includes data on pure HfO_2 and ZrO_2 and c) impedance of HfO_2-SiO_2 bilayer films. Each set has two types of impedance analysis i) variable frequency impedance measurements at fixed temperatures in the range 46-803 °C ii) temperature sweeps of the permittivity over the range 25-600 °C at 5 fixed frequencies between 1 kHz and 1 MHz.

6.3.1 Impact of O_3 dose time on $Hf_{0.5}Zr_{0.5}O_2$ (HZO)

(i) Typical impedance data

Impedance data measured in air at four temperatures for HZO-0.1 s are shown in Figure 6.2. The complex plane plots Z*, (a), show a single, approximately semicircular arc for all temperatures; the sample resistance is obtained from the low frequency intercept of the arcs on the Z' axis.

To obtain more information, the same data are replotted in various ways (b-d). The Z''/M'' spectroscopic plots, (b), show a single overlapping peak at high frequency in Z'' and M'' with

approximate Debye-like width at half maximum, FWHM, close to the ideal value for a Debye peak of 1.14 decades, indicating a good degree of electrical homogeneity in the main resistive component of the bulk sample. Capacitance, C' data (c) show a constant value at low frequencies but a dispersion to lower values with increasing frequency. This dispersion may indicate either the presence of a second component which, from its smaller capacitance value, has greater thickness than the main resistive component (assuming capacitance of a sample component is inversely proportional to its thickness) or it may indicate electrical inhomogeneity in the main bulk component (possibly associated with changes during ozone treatment).

Admittance, Y', data (d), show a low frequency plateau which represents the dc conductivity. At high frequency, a dispersion is seen which may represent either Jonscher Power Law behaviour that is a well-known phenomenon in materials that have ionic and/or electronic hopping conductivity or it may represent relaxation of the main sample resistance leading to a much smaller resistance at higher frequencies.

The initial conclusion from these results, therefore, is that sample HZO-0.1 s has a main overall resistance attributable to a significant fraction of the sample bulk, but there may be some variation in conductivity through the sample bulk. The conduction appears to be entirely electronic since there is no evidence in the capacitance data for a blocking capacitance that could be attributed to oxide ion conduction and a double layer capacitance at the sample-electrode interfaces.

Impedance data for HZO-0.5 s and HZO-1 s, Figure 6.3 and Figure 6.4, were similar in appearance to those of HZO-0.1 s but with different resistance and capacitance values. They also showed a small frequency dependence of the high frequency capacitance which, again, may be associated with electrical inhomogeneity. Interestingly, the magnitude of the low frequency plateau for HZO-1 s is around 2-3 pF whereas that for the other two samples is around 5-6 pF. This may indicate that the resistive layer, low frequency region in the HZO-1 s sample, is thicker than the other two which could possibly be due to increased oxidation at longer ozone treatment times.

Arrhenius plots of the total conductivities of HZO-0.1 s, HZO-0.5 s and HZO-1 s, are shown in Figure 6.5. The conductivities of HZO-0.1 s and HZO-0.5 s were comparable with a little difference in activation energies at lower temperature. However, HZO-1 s, that had the same composition but longer exposure to O_3, had a somewhat lower conductivity than those that

were exposed to a shorter O_3 time (HZO-0.1 s and HZO-0.5 s). On cooling, the conductivity of HZO-0.1 s is reversible, but HZO-1 s which was measured to higher temperature shows a higher conductivity on cooling than on heating. This indicates that HZO thin films can be influenced by either atmospheric conditions, especially at higher temperature, or changes as a result of annealing.

Arrhenius conductivity plots are shown over a wide temperature range for HZO-0.5 s in order to study how HZO-0.5 s thin films behave with increasing temperature, Figure 6.5. The conductivity of HZO-0.5 s increased, at first, linearly with activation energy 0.44(2) eV prior to levelling off at an approximate plateau between 125 and 200 °C but then increased again at higher temperature to reach a steady state at ~ 350 °C and above which, no further conductivity increase occurred. Possibly the plateau between 125-200 °C represented annealing-or atmospheric-induced changes referred to above. The rapid rise in conductivity between ~325 and 350 °C may represent a phase change in the sample. Further studies including the collection of data on cooling from different temperature are needed to understand this behaviour.

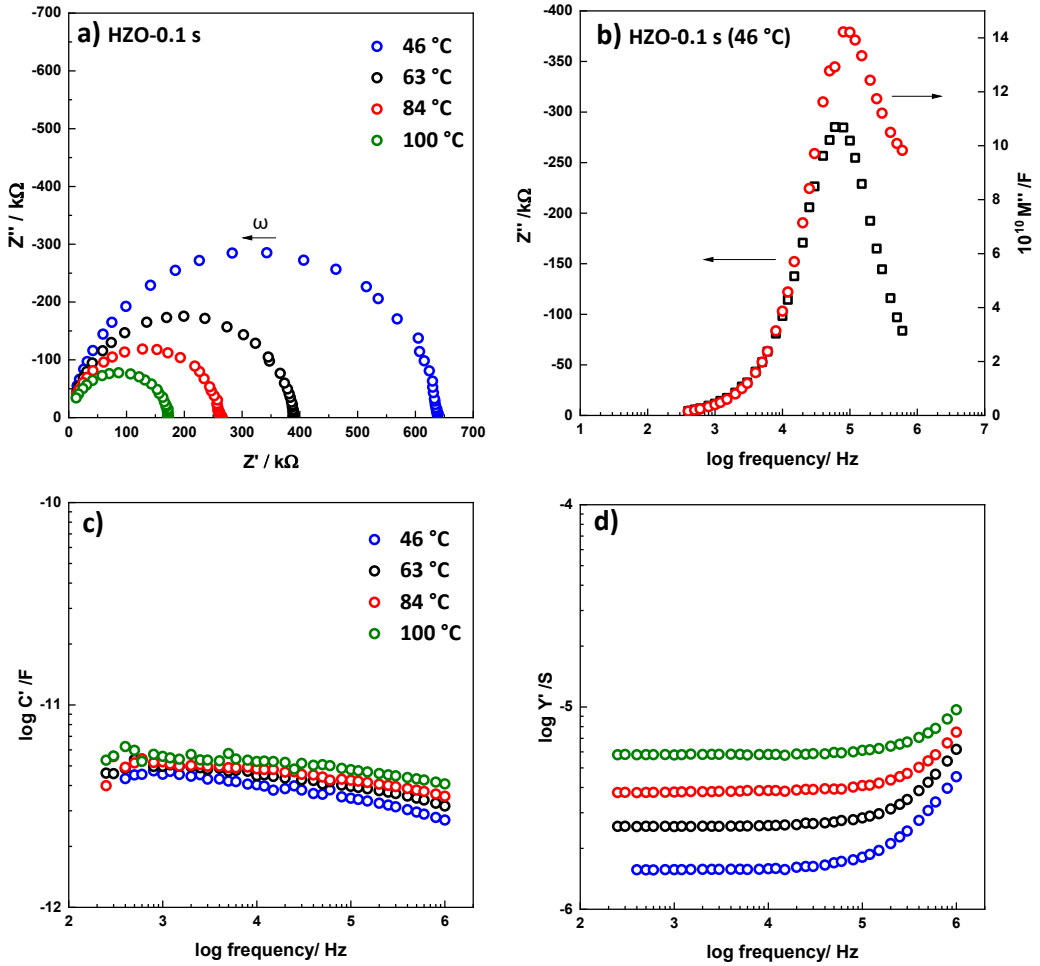

Figure 6.2 a) complex plane plot (Z*), b) Z''/ M'', c) capacitance, d) admittance plots of HZO-0.1 s at different temperatures.

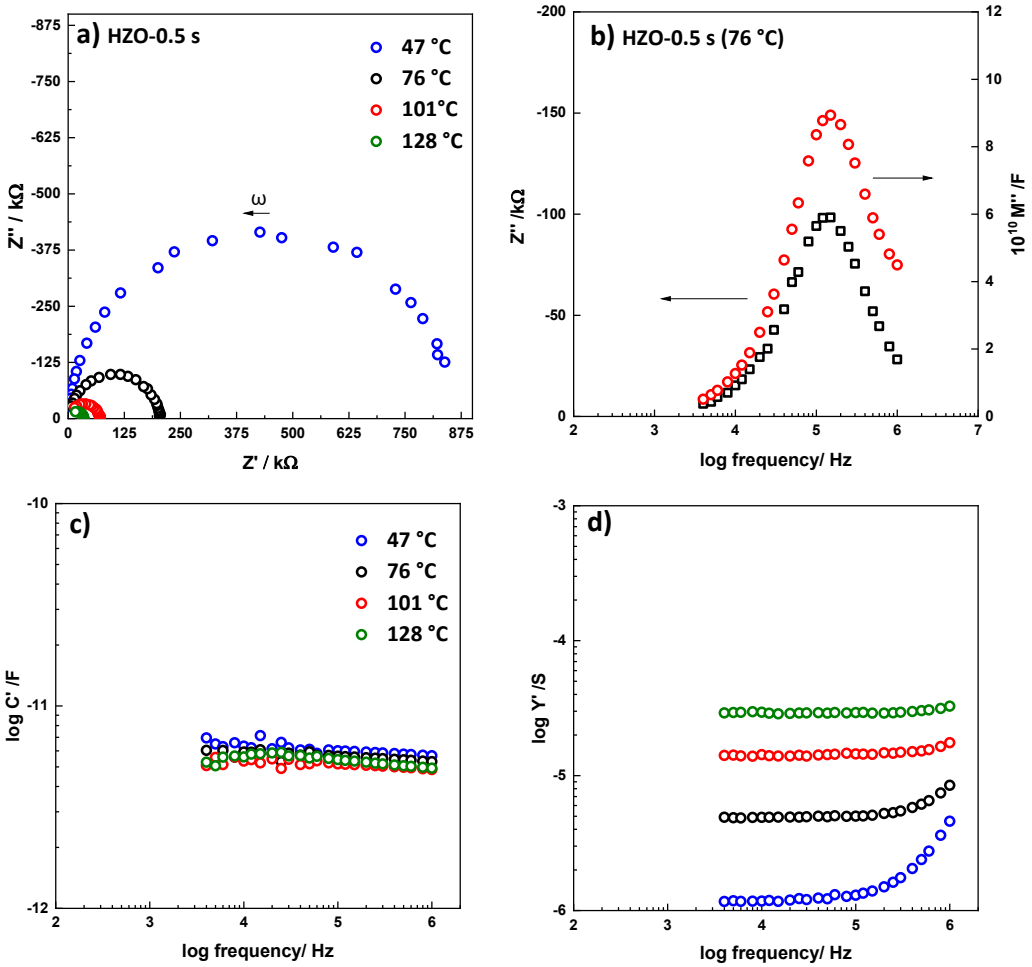

Figure 6.3 a) complex plane plot (Z*), b) Z''/ M'', c) capacitance, d) admittance plots of HZO-0.5 s at different temperatures.

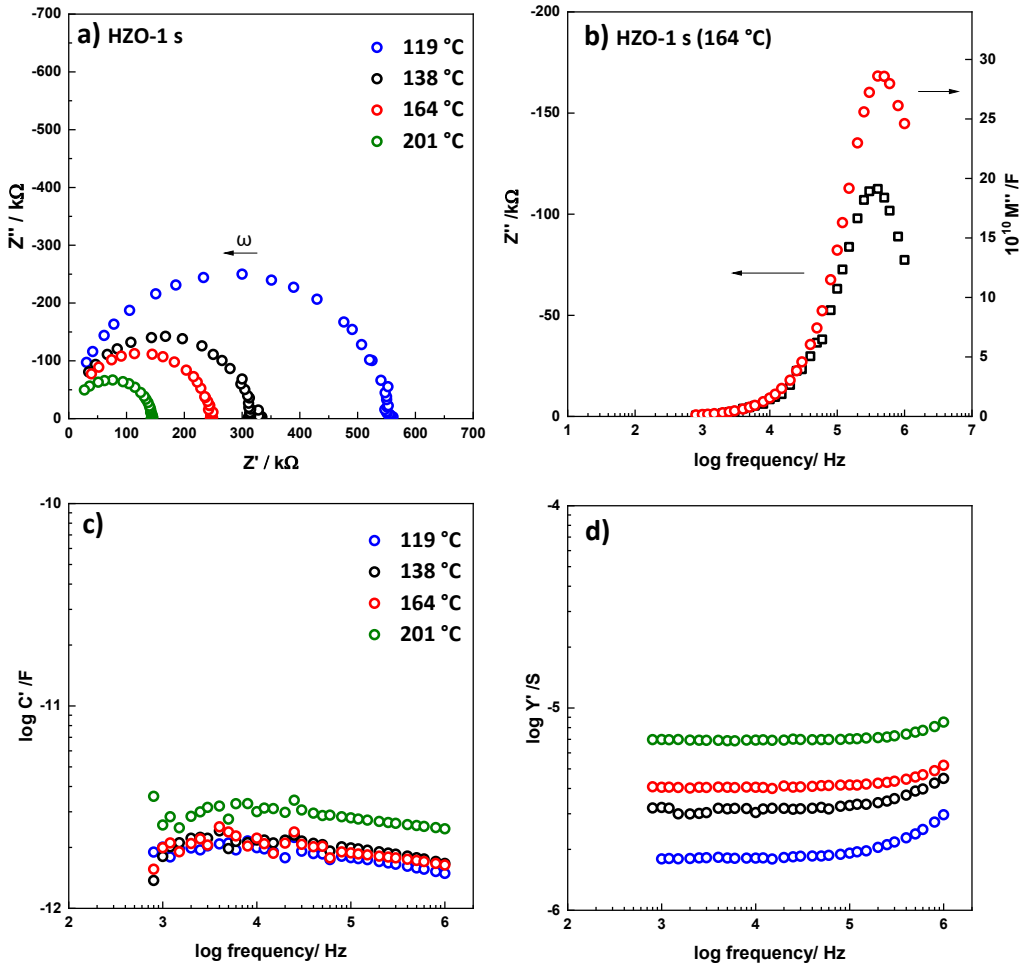

Figure 6.4 a) complex plane plot (Z*), b) Z''/ M'', c) capacitance, d) admittance plots of HZO-1 s at different temperatures.

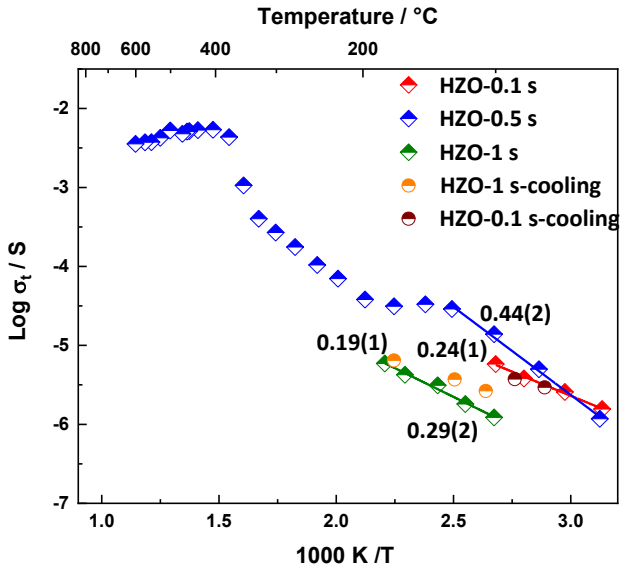

Figure 6.5 Arrhenius plot of σ_t of HZO-0.1 s, 0.5 s and 1 s versus reciprocal temperature. Activation energy, Ea, values in eV are included.

(ii) Effect of oxygen partial pressure, pO_2, during impedance measurements

The effect of pO_2 on impedance data is widely used to discriminate between p-type and n-type conductivity behaviour of materials whose electronic conductivity is extrinsic. With changing pO_2, the electronic carrier concentration of either holes or electrons may change according to the following reactions:

$$1/2O_2 + V_O^{\bullet\bullet} + 2e' \rightarrow O_O^X \qquad 6.1$$

$$1/2O_2 + V_O^{\bullet\bullet} \rightarrow O_O^X + 2h^{\bullet} \qquad 6.2$$

Data were obtained in atmospheres of different pO_2, on all three samples with different O_3 dose time as shown in Figure 6.6. For all samples, resistance decreased reversibly in the sequence N_2-air-O_2 and may attributed to an increase in p-type conductivity caused by the sample-atmosphere exchange reaction, equation 6.2. The conclusion, therefore, is that the samples are extrinsic semiconductors and p-type.

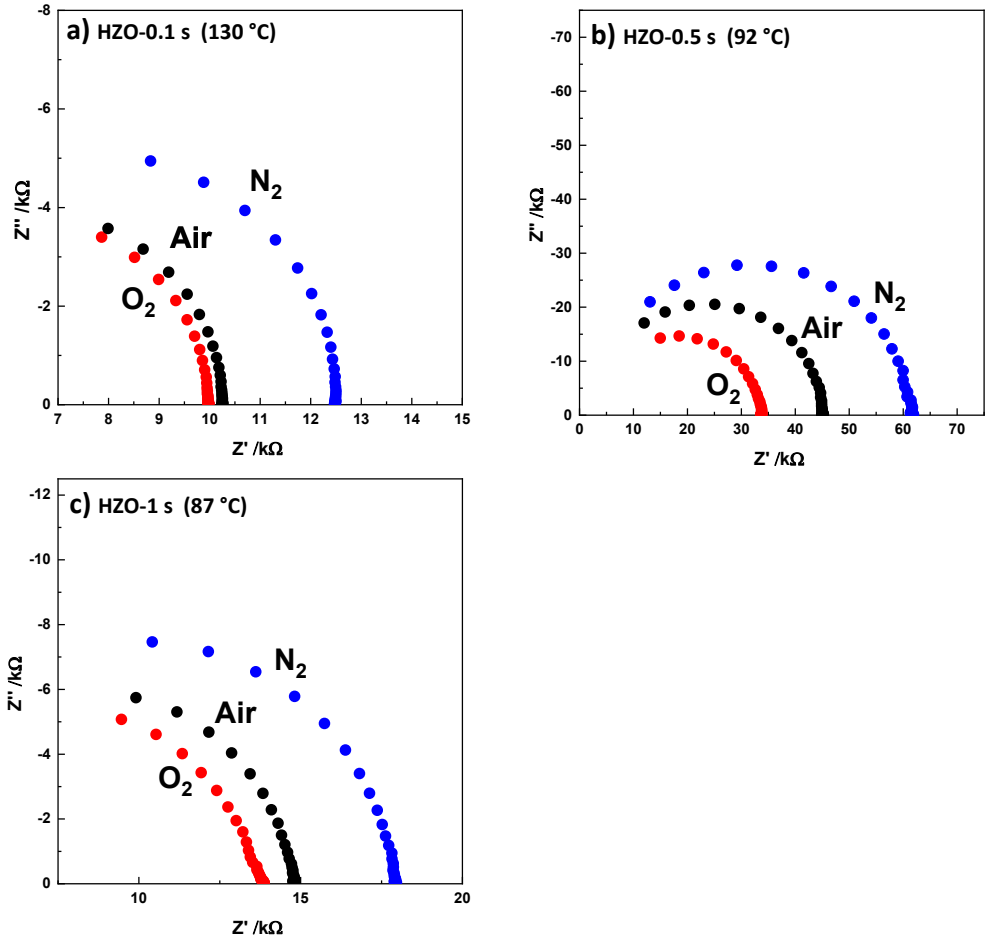

Figure 6.6 Complex plane plot (Z*) of a) HZO-0.1 s, b) HZO- 0.5 s and d) HZO-1 s under different atmosphere.

(iii) Modelling of impedance spectroscopy data of HZO thin films

In order to determine the most appropriate equivalent circuit to represent impedance data and obtain the most appropriate physical interpretation of the impedance parameters, fitting data analysis was carried out. Three equivalent circuits were tested to fit the bulk response of HZO thin film samples. The first circuit consists of a parallel resistor (R), constant phase element (CPE) and capacitor (C) (circuit A), Figure 6.7a. The second circuit consists of a resistor (R) in parallel with a series-connected CPE-C element (circuit B), Figure 6.7e. This equivalent circuit is taken from a recent study of $Pb(Mg_{1/3}Nb_{1/3})O_3$ (PMN) equivalent circuit simulation that shows a high accuracy fitting to impedance data of PMN, relaxor ferroelectric [7]. The third circuit is composed of two parallel RC elements connected in series (circuit C), Figure 6.7, which is commonly used to represent ceramic materials with bulk and grain boundary components.

Figure 6.7 shows the experimental data at 100 °C for HZO-0.1 s and fits to circuits A, B and C. Circuits A and C fit the impedance data of HZO-0.1 s approximately but with 1) a deviation in capacitance, C', data at low frequency, Figure 6.7b, j and 2) a small deviation in admittance, Y', data at high frequency, Figure 6.7c, k. Also, the residuals of circuits A and C (d, l) are poor. By contrast, Circuit B fitted the data well in all presentations as shown with fitted and experimental data (e, f and g) and for other temperatures, Figure 6.8. The residuals in Figure 6.7 (h) and Figure 6.8 (d, h and l) show good accuracy of fits for the whole frequency range with a little inaccuracy at high frequency and lowest temperature (d) which can be associated with either the presence of a second, more conductive component or inaccuracies in experimental data at the frequency limits of the instrumentation.

Circuit B, also, gave a high accuracy fitting in all kind of plots (Z', M', C', Y' and residuals) for the other two samples, HZO-0.5 s and HZO-1 s, Figure 6.9 and Figure 6.10. Complete sets to fitted data of circuit B for HZO-0.1 s, HZO-0.1 s and HZO-1 s are given in Table 6.2-6.4.

Arrhenius plots of σ_1 obtained from the fitting of circuit B are shown Figure 6.11a. The data show that conductivity of three samples, HZO-0.1 s, HZO-0.5 s and HZO-1 s, at lower temperatures are identical to those obtained by visual inspection of the impedance complex plane, Z*, plots, Figure 6.5, with a little difference in the activation energy of HZO-1 s.

The fitted data of bulk capacitance, C_1, showed comparable values for HZO-0.1 s and 0.5 s which are lower than the fitted capacitance of HZO-1 s. This supports the suggestion that

the region responsible for the main resistance is thicker in sample HZO-1 s than in the other two samples.

The CPE_1 values of *A* and n obtained from circuit B are shown Figure 6.11b, c and d. The conductivity of CPE, *A*, of HZO-1 s and HZO-0.1 s were lower than that of HZO-0.5 s. This indicates the behaviour similarity between the conductivity of main component, R_1, of HZO-0.5 s, that showed a higher conductivity than HZO-0.1 s and HZO-1 s and the CPE conductivity, *A*.

Circuit B consists of a resistor (R) in parallel with a series-connected CPE-C element which is attributed to the bulk impedance response. The inclusion of R in the equivalent circuit used to fit impedance data of all HZO thin film devices means that there is a leakage conductivity. Therefore, all HZO thin films appear to act as a leaky capacitor and this leakage current is associated with dc conductivity.

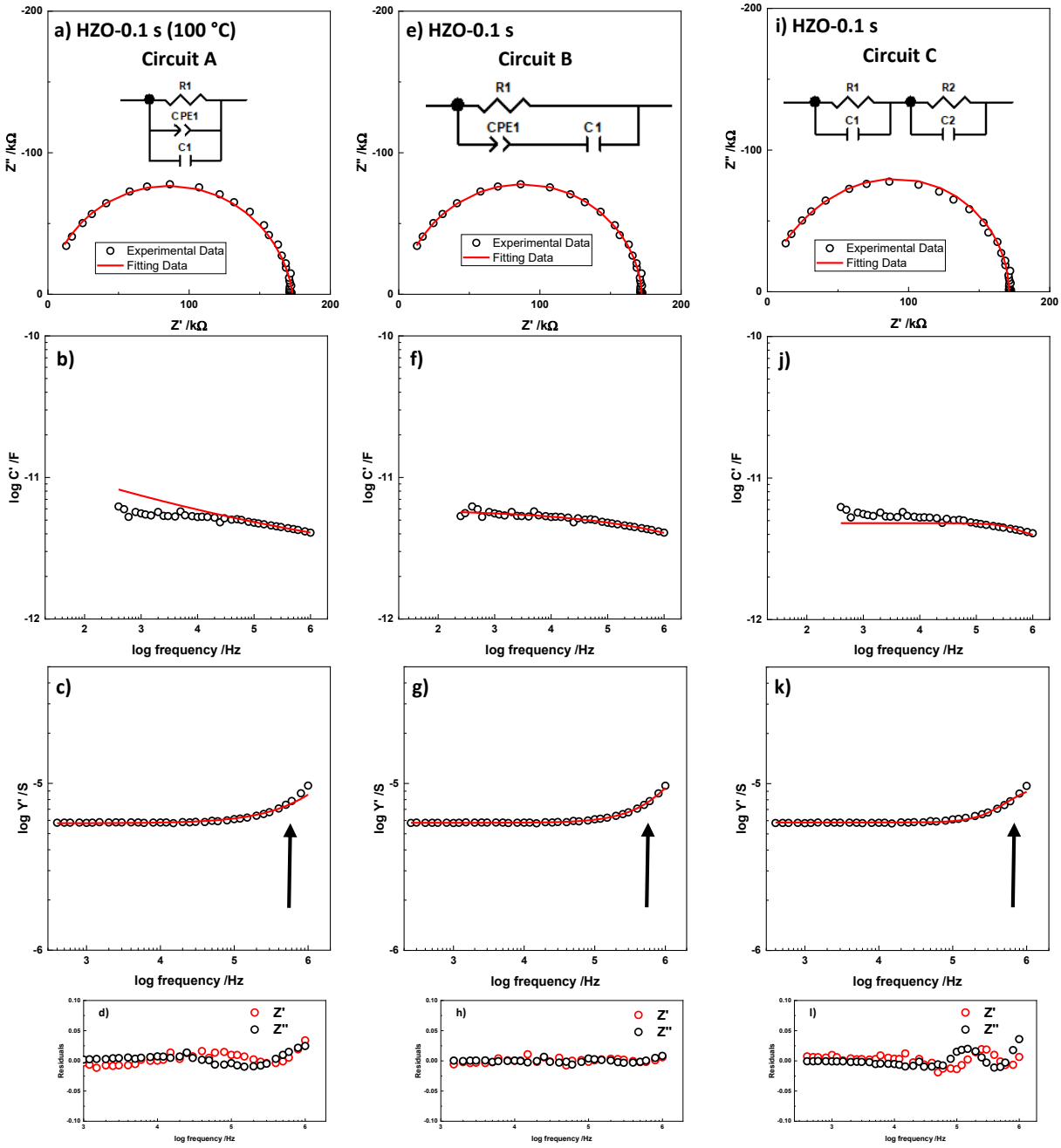

Figure 6.7 Experimental and fitted data to circuit A, B and C for a, e and i) complex plane plot (Z*), b, f and j) capacitance, c, g and k) admittance plots d, h and l) Impedance residuals of HZO-0.1 s at 100 °C.

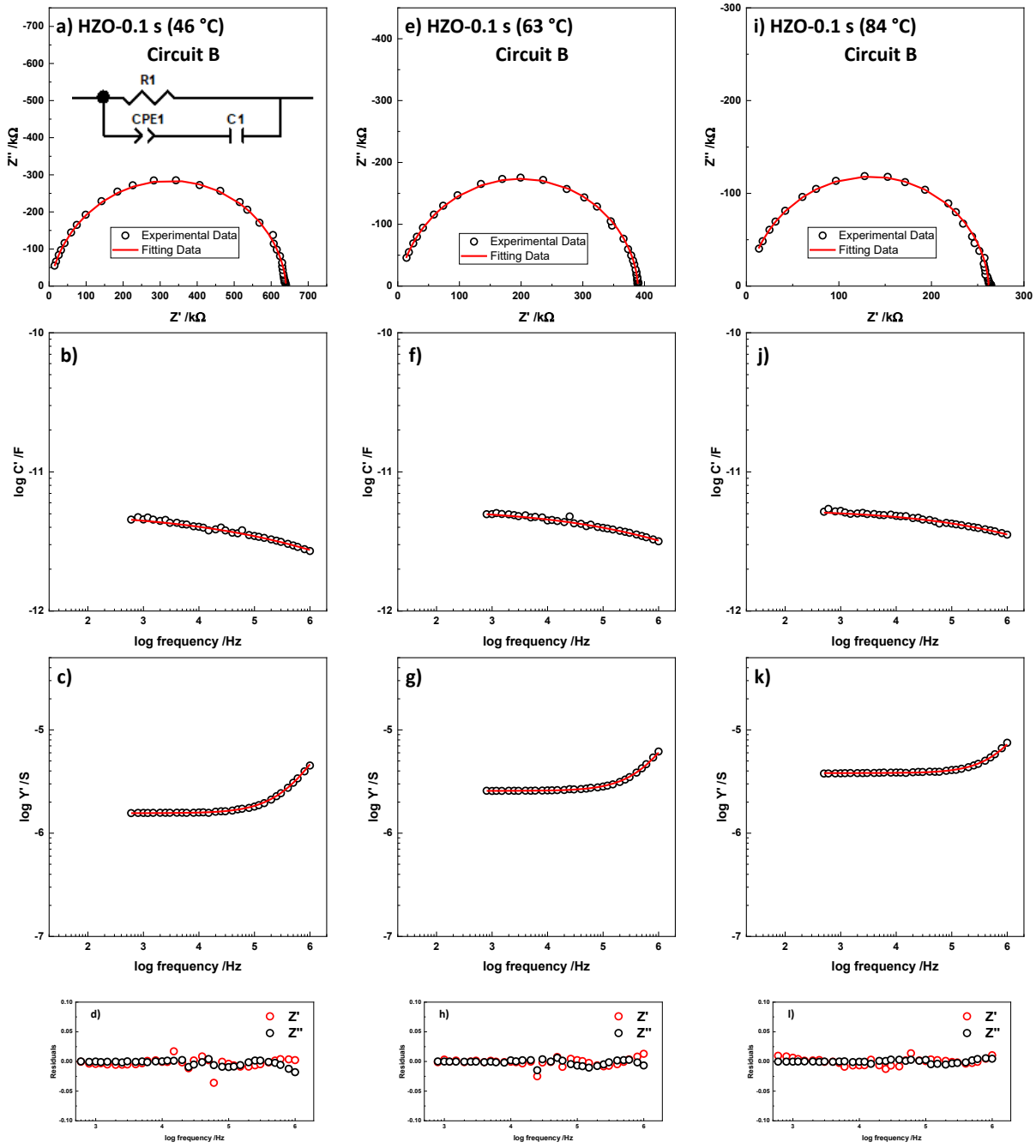

Figure 6.8 Experimental and fitted data to circuit B for a) complex plane plot (Z*), b) Z''/ M'', c) capacitance, d) admittance plots and l) Impedance residuals of HZO-0.1 s at different temperatures.

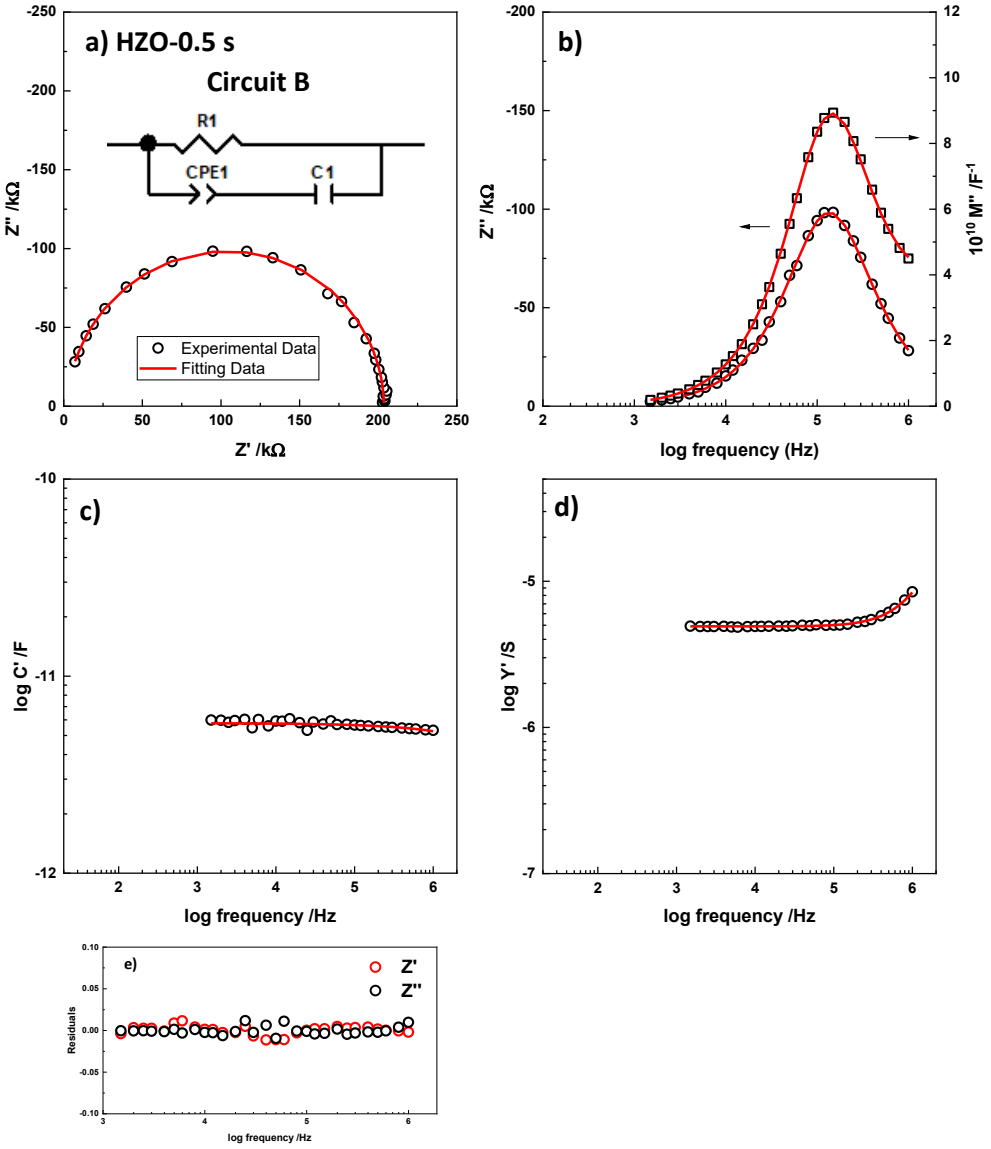

Figure 6.9 Experimental and fitted data to circuit B for a) complex plane plot (Z*), b) Z''/ M'', c) capacitance, d) admittance plots and l) Impedance residuals of HZO-0.5 s at 76 °C.

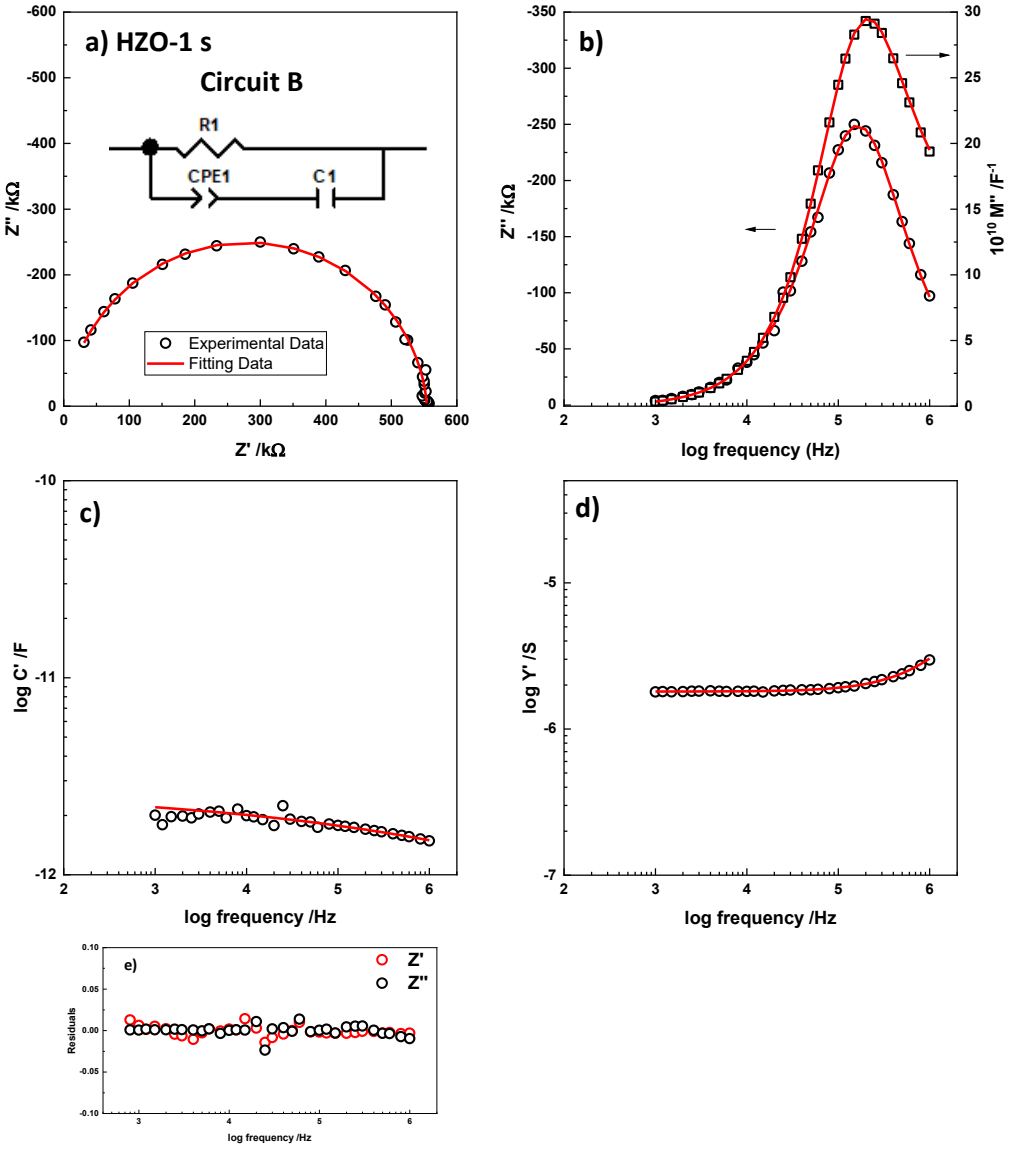

Figure 6.10 Experimental and fitted data to circuit B for a) complex plane plot (Z*), b) Z''/ M'', c) capacitance, d) admittance plots and l) Impedance residuals of HZO-1 s at 119 °C.

Table 6.2 Fitted parameters for HZO-0.1 s of circuit B collected at lower temperatures.

T (°C)	R_1 (kΩ)	A	n	C_1 (F)
46	640(1)	3.1(8)E-10	0.75(1)	5.6(2)E-12
63	390.0(4)	7(1)E-10	0.71(1)	5.2(1)E-12
84	262.6(2)	9.6(1)E-10	0.71(fixed)	5.3(3)E-12
100	172.1(1)	9.99(8)E-10	0.72(fixed)	5.92(2)E-12

Table 6.3 Fitted parameters for HZO-0.5 s of circuit B collected at lower temperatures.

T (°C)	R_1 (kΩ)	A	n	C_1 (F)
47	853(3)	4.5(5)E-8	0.55(fixed)	6.32(3)E-12
76	204(3)	4(2)E-7	0.41(3)	5.78(3)E-12
101	70.8(1)	7.9(4)E-8	0.5(fixed)	5.45(4)E-12
128	34.35(4)	8.6(4)E-7	0.36(fixed)	5.36(3)E-12

Table 6.4 Fitted parameters for HZO-1 s of circuit B collected at lower temperatures.

T (°C)	R_1 (kΩ)	A	n	C_1 (F)
119	552.2(7)	7(4)E-11	0.80(3)	2.6(2)E-12
138	320(1)	7.0(3)E-11	0.81(fixed)	3.1(1)E-12
164	234.6(4)	1.13(3)E-10	0.81(fixed)	3.35(5)E-12
201	144.5(1)	1.53(3)E-10	0.81(fixed)	3.40(3)E-12

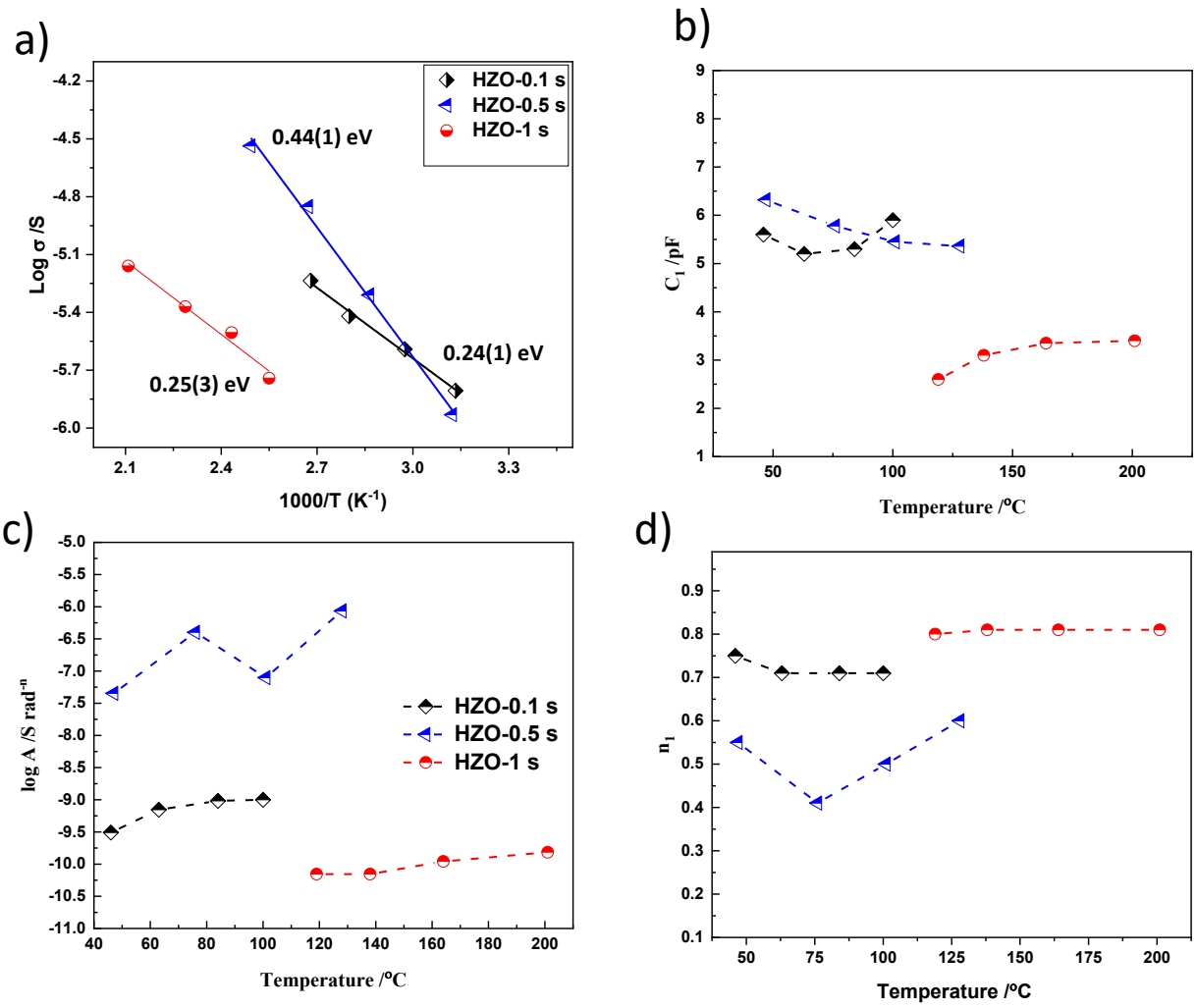

Figure 6.11 a) Arrhenius plot for fitted values of R_1. Fitted parameters of (b) C_1 and (c and d) A, n of CPE_1 of circuit B for HZO-0.1 s, HZO-0.5 s and HZO-1 s.

(ii) Permittivity results

Results of fixed frequency, variable temperature sweeps of relative permittivity, ε_r, are shown in Figure 6.12. HZO-0.1 s and HZO-1 s, show a sharp permittivity peak at 474 and 465 °C, respectively, while HZO-0.5 s shows two broader peaks at 423 and 465 °C, Figure 6.12c. The permittivity maxima, $\varepsilon_{r,max}$, are ~10600, 11048 and 11100 at 474, 465 and 465 °C for HZO-0.1 s, HZO-0.5 s and HZO-1 s, respectively. These permittivity peaks are presumably associated with a ferroelectric-paraelectric phase transition at the Curie temperature, T_c. The magnitude of permittivity maxima, $\varepsilon_{r,max}$, decreased with frequency at T_c. All samples show a strong frequency dependence of the peak maximum with the same peak temperature (T_c). Therefore, space charge capacitance may have an impact on the magnitude of the peak

permittivity maximum. More measurements are needed to investigate the effects of space charge on the permittivity of HZO thin films.

HZO-0.5 s, Figure 6.12c, behaves slightly different and shows two permittivity peaks at ~ 423 and 465 °C which could possibly be associated with phase transitions from orthorhombic to tetragonal and from tetragonal to monoclinic phases as discussed in chapter 2 section 2.5.2. Alternatively, the sample may be electrically inhomogeneous and contain two orthorhombic phases with slightly different composition or oxygen content and therefore, different T_c. Permittivity values of HZO-0.5 s extracted from impedance data follow a similar trend, Figure 6.12d.

At lower temperatures before the Curie temperature, Figure 6.12b, d and g, the permittivity of HZO-0.1 s shows almost constant values and then a reduction before it increased rapidly at ~410 °C. For HZO-0.5 s, the data shows a broader peak at ~125 °C, while the permittivity data of HZO-1 s increased gradually until reached at 400 °C at which a sharp increase in the permittivity occurred, Figure 6.12g.

According to these results, HZO thin films are ferroelectric with a high permittivity value similar to that of the well-known ferroelectric $BaTiO_3$. As far as we are aware, this high permittivity at high temperature of HZO thin films has not been reported before.

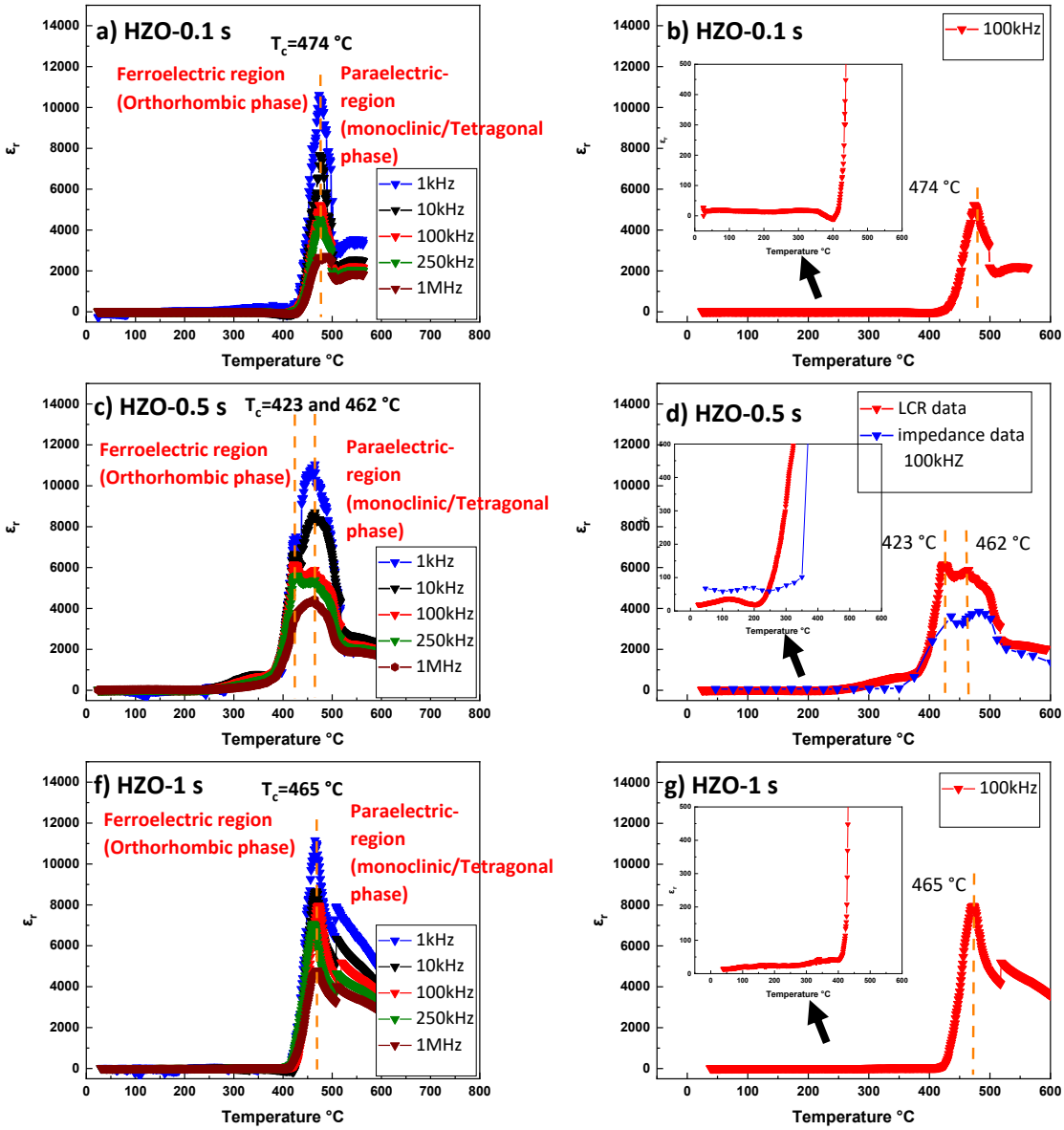

Figure 6.12 Permittivity as a function temperature measured at different frequencies for a, b) HZO-0.1 and c, d) HZO-0.5 s and f, g) HZO-1 s.

6.3.3 Impact of composition x in $Hf_{1-x}Zr_xO_2$

(i) Typical impedance data

Impedance data measured in air for five compositions of $Hf_{1-x}Zr_xO_2$ (x=0, 0.4, 0.5, 0.6 ,and 1) are shown in Figure 6.. The Z^* complex plane plots (a) for all samples, show a single, approximately semicircular arc whose resistances obtained from the low frequency intercepts were used for the conductivity Arrhenius plots in Figure 6.14.

The Z''/M'' spectroscopic plots for $Hf_{0.5}Zr_{0.5}O_2$, Figure 6.14b, show single overlapping peaks at high frequency with approximate Debye-like width at half maximum, FWHM, close to the ideal value for a Debye peak of 1.14 decades. This is a similar to that obtained in samples with top electrodes (HZO-0.1, 0.5 1 s) and indicates a good degree of electrical homogeneity in the main resistive component of the sample which, presumably, is the bulk component. All other compositions, $Hf_{1-x}Zr_xO_2$ (x=0, 0.4, 0.6, and 1) showed a similar behaviour.

Capacitance, C' data for all samples (c) show a high frequency plateau in the range 6-8 pF attributable to the sample bulk, expect for ZrO_2 that shows higher capacitance values ~10 pF.

Admittance, Y' data, (d), show a low frequency plateau which represents the *dc* conductivity. At high frequency, a dispersion is seen which may represent Jonscher Power Law behaviour similar to that of HZO samples, described above.

The Arrhenius plots in Figure 6.14 show the total conductivity of five compositions of $Hf_{1-x}Zr_xO_2$ (x=0, 0.4, 0.5, 0.6, and 1). The conductivity of pure ZrO_2 thin film is larger than pure HfO_2 by half order of magnitude. When Hf doped with ZrO_2 ($Hf_{0.4}Zr_{0.6}O_2$), its conductivity becomes in between pure ZrO_2 and HfO_2. In contrast, Zr doped HfO_2 thin films ($Hf_{0.5}Zr_{0.5}O_2$ and $Hf_{0.6}Zr_{0.4}O_2$) show a different behaviour and the conductivities of $Hf_{0.5}Zr_{0.5}O_2$ and $Hf_{0.6}Zr_{0.4}O_2$ thin films became smaller than that of pure HfO_2. The activation energy of all samples were in the range of 0.34-0.55 eV. All five compositions of $Hf_{1-x}Zr_xO_2$ (x=0, 0.4, 0.5, 0.6, and 1) thin films including pure HfO_2 and ZrO_2 appear to be high semiconducting materials with smaller activation energies. These conductivities of $Hf_{1-x}Zr_xO_2$ (x=0, 0.4, 0.5, 0.6, and 1) are far away from the same material in ceramics that have high resistance values with larger activation energy.

It was suspected that the impedance measurements and data may have been influenced by atmospheric conditions as occurred with HZO 0.1, 0.5 and 1 s, Figure 6.6. Data of $Hf_{1-x}Zr_xO_2$ (x=0, 0.4, 0.5, 0.6 ,and 1) were therefore collected in different pO_2 , as shown in Figure 6.15. For all five samples, resistance decreased with changing atmosphere from N_2-air-O_2 and may attributed to an increase in p-type conductivity, as occurred with HZO samples.

(ii) Permittivity results

Results of fixed frequency, variable temperature sweeps of permittivity, ε_r, of $Hf_{1-x}Zr_xO_2$ (x=0, 0.4, 0.5, 0.6 ,and 1) are shown in Figure 6.16. These five samples do not have a top grid electrode. $Hf_{0.5}Zr_{0.5}O_2$ and ZrO_2 show a peak at 380-390 °C. $Hf_{0.6}Zr_{0.4}O_2$, $Hf_{0.5}Zr_{0.5}O_2$, and

$Hf_{0.4}Zr_{0.6}O_2$, and ZrO_2 show a peak between 431-455 °C. Apart from $Hf_{0.6}Zr_{0.4}O_2$, all samples show a peak above 510 °C, Figure 6.16f. However, by comparing $Hf_{0.5}Zr_{0.5}O_2$ data with HZO samples that have identical composition and the only differences in top electrodes and exposure to O_3 dose, $Hf_{0.5}Zr_{0.5}O_2$ did not show the same HZO permittivity peak positions and magnitude. Also, all $Hf_{1-x}Zr_xO_2$ (x=0, 0.4, 0.5, 0.6, and 1) samples exhibited rather inconsistent results. This appears to indicate the importance of the top grid electrode, perhaps by providing a protective layer to prevent the TiN electrode from oxidation or a kinetic stability of sample electrical behaviour. Further studies are needed to understand this.

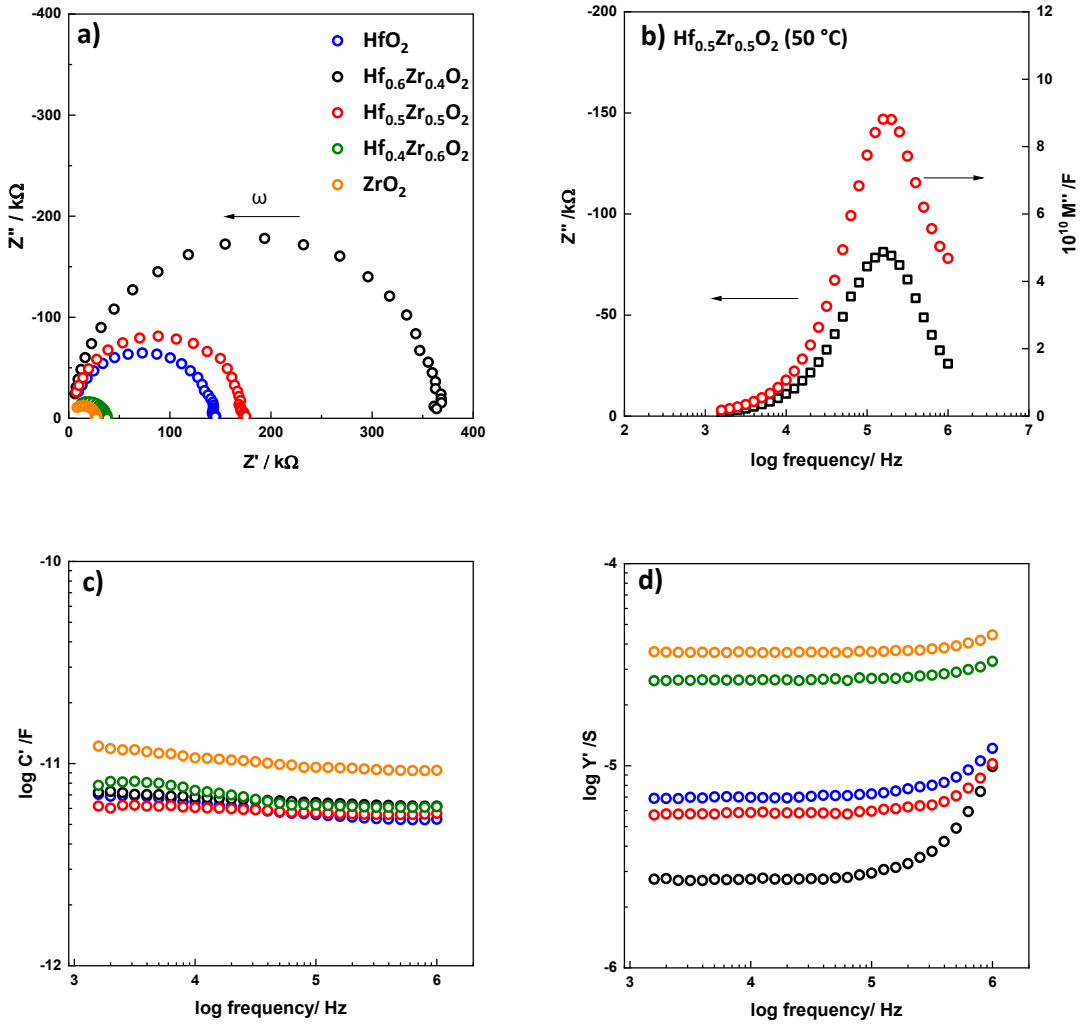

Figure 6.13 a) complex plane plot (Z*), c) capacitance, and d) admittance plots of five samples $Hf_{1-x}Zr_xO_2$ (x=0, 0.4, 0.5, 0.6 ,and 1). B) Z''/ M'' plot of $Hf_{0.5}Zr_{0.5}O_2$at 50 °C.

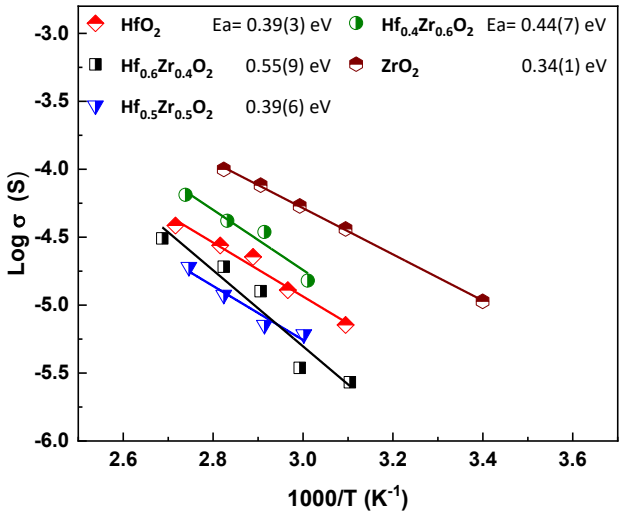

Figure 6.14 Arrhenius plot of σ_t of $Hf_{1-x}Zr_xO_2$ (x=0, 0.4, 0.5, 0.6, and 1) versus reciprocal temperature. Activation energy, Ea, values in eV are included.

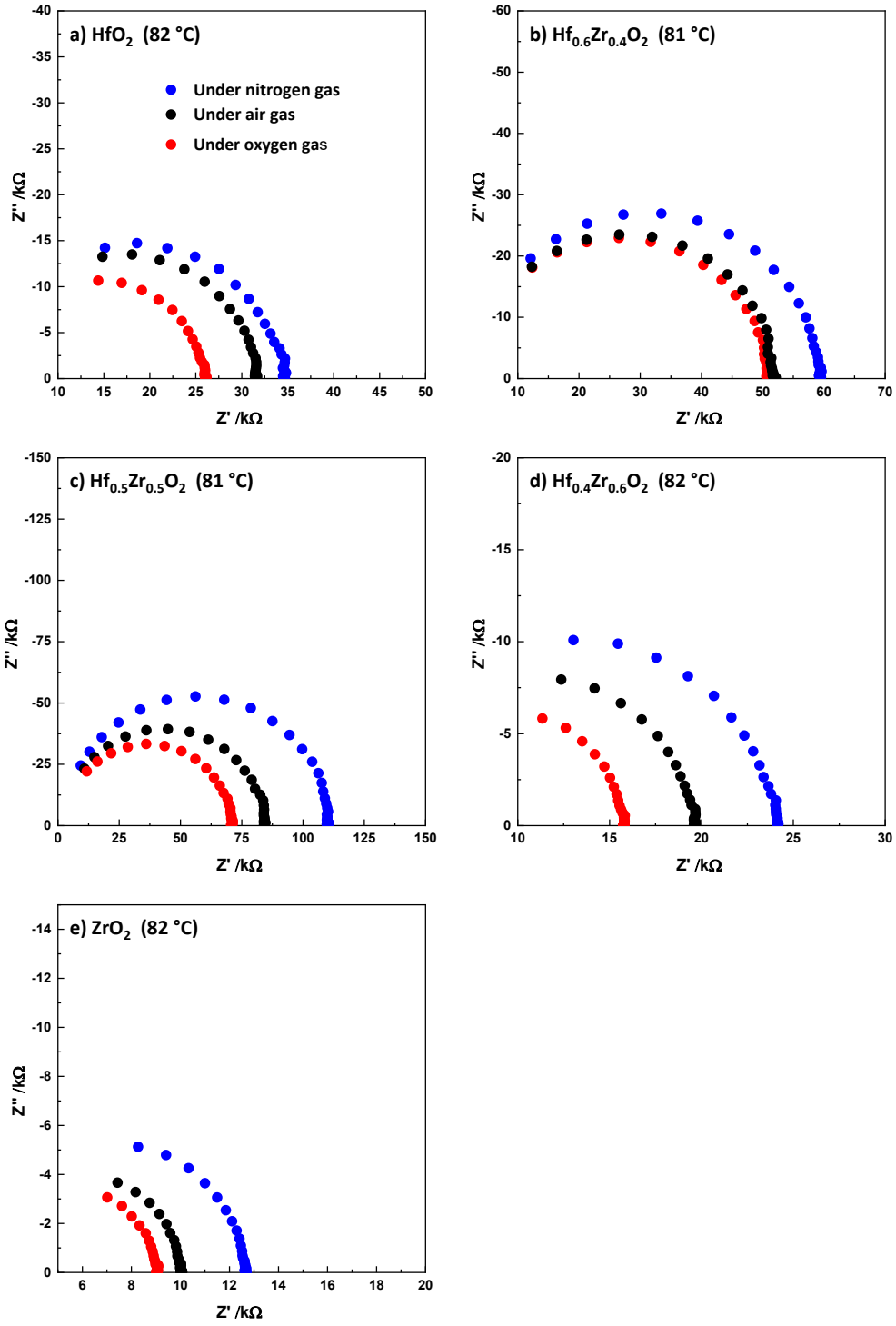

Figure 6.15 Complex plane plot (Z*) of a) HfO_2, b) $Hf_{0.6}Zr_{0.4}O_2$, c) $Hf_{0.5}Zr_{0.5}O_2$, d) $Hf_{0.4}Zr_{0.6}O_2$, e) ZrO_2 under different atmosphere.

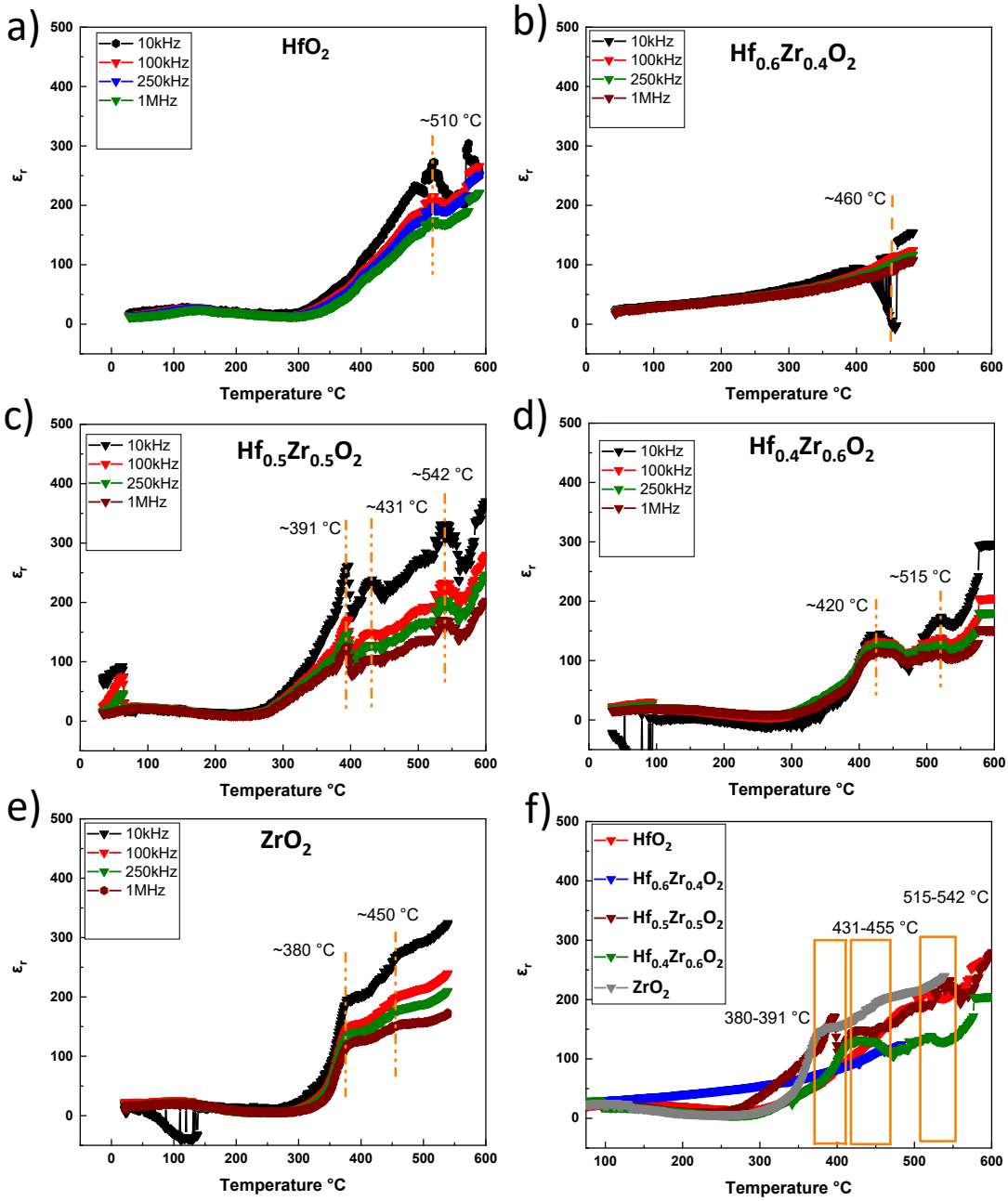

Figure 6.16 Permittivity as a function temperature measured at different frequencies for a) HfO_2, b) $Hf_{0.6}Zr_{0.4}O_2$ c)$Hf_{0.5}Zr_{0.5}O_2$, d) $Hf_{0.4}Zr_{0.6}O_2$ e) ZrO_2 and f) comparison for all compositions.

6.3.4 Impact of adding SiO_2 layer in Hafnia thin films device

For sample HfO_2-SiO_2, the impedance data were insulating at room temperature, R>>10 MΩ. Impedance data were therefore recorded in air at 507, 603, 703, 803 °C, Figure 6.17. The total resistance is still >> 10 MΩ but a high frequency component with much smaller

resistance, R_1 can be seen with an approximate value 100 kΩ at 803 °C. Circuit fitting to obtain accurate values for R_1 has not been carried out but approximate values are shown in the conductivity Arrhenius plot in Figure 6.18.

The same date reprocessed and plotted as log C' vs log f in Figure 6.17c. Data show a high frequency plateau in the range 1 – 10 pF and a low frequency plateau around 100 pF. Clearly, the sample contains two resistive components with relative thicknesses in the approximate ratio (20-100):1. For a typical ceramic, these would be assigned to bulk and grain boundary impedances. This is further emphasised in the M"/Z" vs log f plots, (e), which show a high frequency peak in M" that probably represents the bulk (HfO_2) or TiO_2 layer that can be formed by oxidation of TiN at high temperature and the tail of a large Z" peak at low frequencies that represents a more resistive layer probably silica component or a grain boundary impedance. It is clear from Figure 6.17, however, the two resistance in the hafnia-silica sample differ by many orders of magnitude. We do not know the exact microstructure of the sample, but, in general, SiO_2 layer shows to block the current which was the aim of preparing this thin film sample.

The Arrhenius plots of R_1 of the HfO_2-SiO_2 showed that high frequency component, R_1, of HfO_2-SiO_2 sample had much lower conductivity and greater activation energy, 0.94 eV, than pure HfO_2 thin film sample, Figure 6.18. This probably means that R_1 could be associated with HfO_2 layer that is fully oxidised at higher temperature, leading to a reduction in its conductivity by many orders of magnitude or may belong to TiO_2 layer rather than HfO_2 layer.

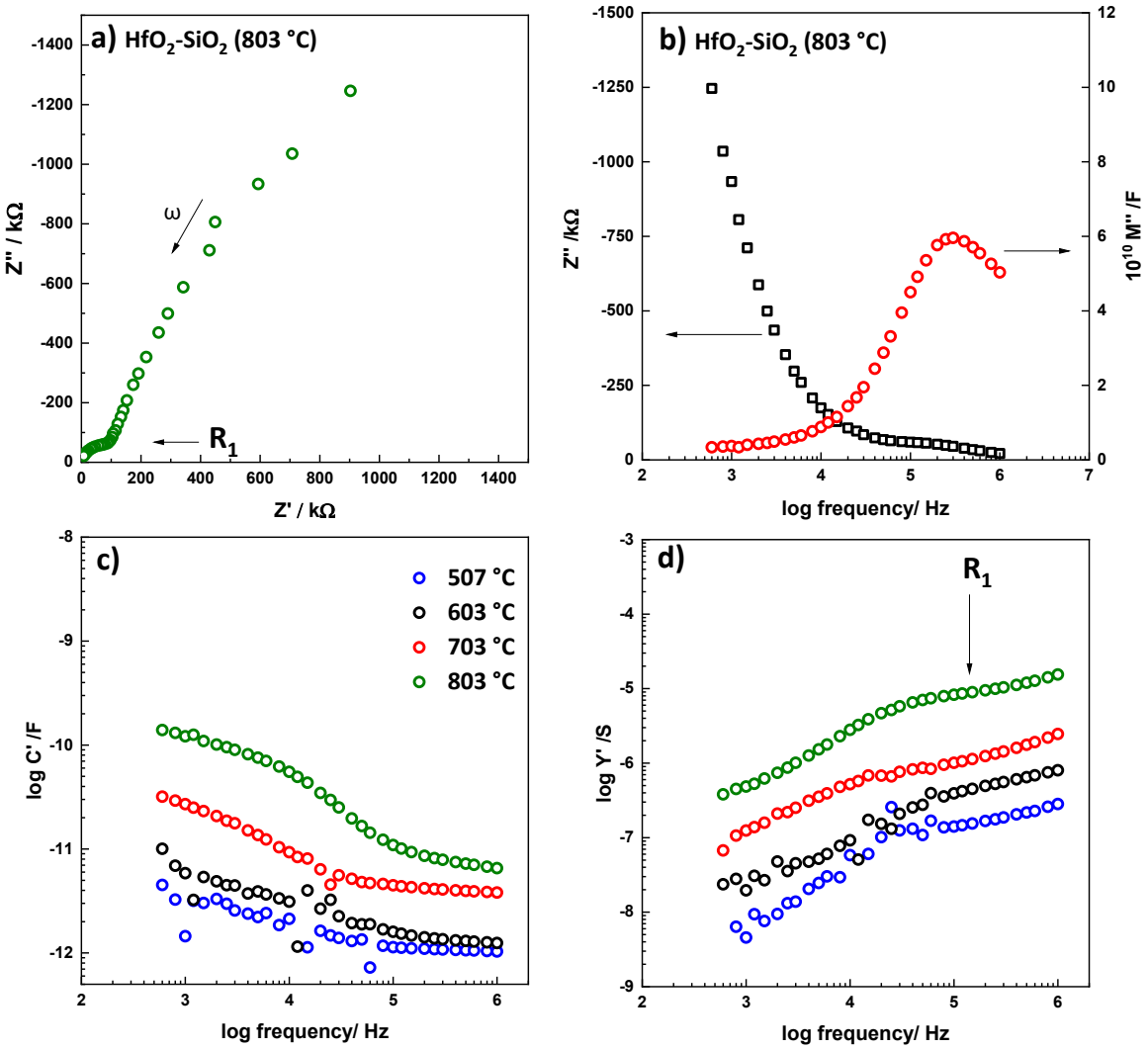

Figure 6.17 a) complex plane plot (Z*), b) Z''/ M'', c) capacitance, d) admittance plots of HfO_2-SiO_2 sample at different temperatures.

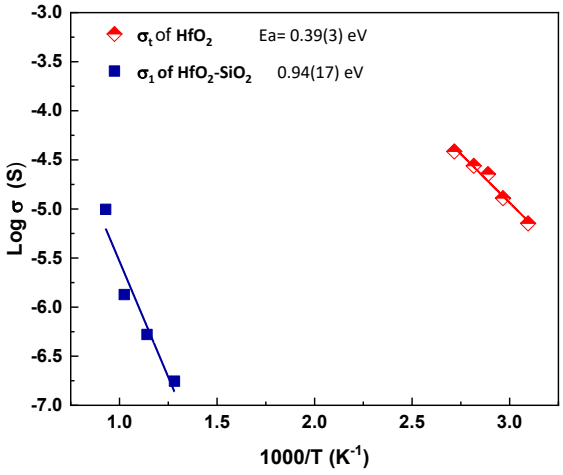

Figure 6.18 Arrhenius plot of σ_1 of HfO_2-SiO_2 and σ_t of HfO_2 versus reciprocal temperature. Activation energy, Ea, values in eV are included.

6.4 Discussion

This chapter reports impedance measurements on several sets of ferroelectric HZO thin-films which offer a new insight into the electrical properties of HZO thin films, their sensitivity to oxygen partial pressure, the most appropriate equivalent circuit to model HZO thin films and the nature of the ferroelectric-paraelectric phase transition in the films.

Impedance data of $Hf_{1-x}Zr_xO_2$ thin films show one homogenous component, associated with the main resistive component of the sample which, presumably, is the bulk component. This means that there is no significant impact of bottom and top electrodes on the overall impedance and all layers above and below HZO-bulk are very conductive. The SiO_2-HfO_2 thin film sample was prepared in the same way as the HZO films but silica is included as one of the layers in order to investigate if we can separate the impedance of the hafnia component from that of silica. The results show two components with high total resistance values that cannot be measured at any temperature below 803 °C. The second component, R_1, can be measured with a much smaller resistance of ~100 kΩ. This second component has a much smaller conductivity than that of pure HfO_2 thin films. R_1, therefore, can probably be related either to TiO_2 layer formed by oxidation of TiN at high temperature or HfO_2 that becomes fully oxidised at high temperature. However, in general, the SiO_2 layer, whose impedance in series with the HfO_2 component, was found to block the current completely which was the reason for preparing and measuring this thin film sample.

The conductivity of HZO thin films, Figure 6.5, shows that HZO-1 s had lower conductivity than HZO-0.1 s and HZO-0.5 s. It appears that when HZO films are exposed to O_3 for a slightly longer time (1 second), the carrier concentration is reduced which lowers the conductivity. HZO films, that are deposited with a short O_3 dose time (0.1 s), contain a non-polar tetragonal/ polar orthorhombic phase mixture with a large portions of non-t phase, while HZO deposited with a slightly longer O_3 time contains a highest o- polar phase [6]. This large portion of o-polar phase and its polarisation ability to store the charges could cause a reduction on the conductivity. This is supported by the permittivity data, showing that the permittivity maxima, $\varepsilon_{r,max}$, of HZO-1 s had bigger values than other two samples.

The Arrhenius plots, Figure 6.5, especially the non-linear behaviour for HZO-0.5 s which was obtained over a wide temperature range, together with frequency-dependent ε' data at

high frequencies indicate that the sample bulk response may not be entirely homogenous but may be atmosphere-dependent and in particular, can be affected by the ozone treatment.

The effect of pO_2 on the resistance of $Hf_{1-x}Zr_xO_2$ thin films indicates the presence of electronic conduction within the thin-film samples. All samples show a decrease in the resistance with increasing pO_2. This means that $Hf_{1-x}Zr_xO_2$ thin films have p-type behaviour. In p-type materials, holes are introduced, resulting in an increase in the charge carrier concentration, therefore this leads to enhance the conductivity. Since thermal activation takes a role in conduction of the current materials, the holes ought to be located on particular atomic species. There are two possibilities for the location of holes. First, in insulating oxides, holes can be on impurities such as Fe that may exist in the raw materials or impurities created during the preparation of thin-films. Second, several high purity ceramic oxides show that, since there are no cations that is able to ionize to a higher oxidation state, holes are attributed to reaction of under-bounded oxygen and absorbed O_2 molecules [8-10]:

$$O^{2-} + V_O^{\bullet\bullet} + 1/2O_2 \rightarrow 2O^- \qquad (6.3)$$

This leads to that O^- occupies the lattice vacancies and be the source of p-type conductivity.

Temperature sweeps of the permittivity over the range 25-600 °C at 5 fixed frequencies show a maximum peak permittivity attributed to the Curie temperature for all samples (HZO-0.1 s, HZO-0.5 s and HZO-1 s). This result is the first report of a maximum peak permittivity of ferroelectric based-HfO_2 thin films and is consistent with XRD data that indicate the absence of a ferroelectric phase between at 740 K (465 °C) [5]. Also, the Curie temperatures are comparable with that deduced from XRD data of Y-doped and non-doped HfO_2 films reported in the literature [11, 12].

6.5 Conclusions

- The impedance data of $Hf_{1-x}Zr_xO_2$ thin films show one homogenous component which is associated with a ferroelectric hafnia component.
- The conductivity of all thin films samples increased reversibly with increasing pO_2 and is attributed to an increase in p-type electronic conduction.
- A possible circuit, that gave an accurate fitting of the data of all samples, is composed of a resistor in parallel with a series-connected CPE-C element.

- HZO-0.1 s, HZO-0.5 s and HZO-1 s thin films appear to be ferroelectric with high relative permittivity values, ~10600, 11048 and 11100 at 474, 465 and 465 ˚C, respectively, that have not been reported previously.
- Results of fixed frequency variable temperature sweeps of permittivity, ε_r, of $Hf_{1-x}Zr_xO_2$ (x=0, 0.4, 0.5, 0.6 and1) thin films, that is without top electrode, does not show a maximum permittivity peak (unlike to that obtained in samples with top electrodes, HZO-0.1, 0.5, 1 s). This indicates the importance of the top grid electrode in providing a protection layer to give kinetic stability to the thin film device.

6.6 References

1. Böscke, T., J. Müller, D. Bräuhaus, U. Schröder, and U. Böttger, *Ferroelectricity in hafnium oxide thin films.* Applied physics letters, 2011. **99**(10): p. 102903.
2. Böscke, T., J. Müller, D. Bräuhaus, U. Schröder, and U. Böttger. *Ferroelectricity in hafnium oxide: CMOS compatible ferroelectric field effect transistors*. in *2011 International Electron Devices Meeting*. 2011: IEEE.
3. Park, M.H., Y.H. Lee, T. Mikolajick, U. Schroeder, and C.S. Hwang, *Review and perspective on ferroelectric HfO_2-based thin films for memory applications.* MRS Communications, 2018. **8**(3): p. 795-808.
4. Müller, J., E. Yurchuk, T. Schlösser, J. Paul, R. Hoffmann, S. Müller, D. Martin, S. Slesazeck, P. Polakowski, and J. Sundqvist. *Ferroelectricity in HfO_2 enables nonvolatile data storage in 28 nm HKMG*. in *2012 Symposium on VLSI Technology (VLSIT)*. 2012: IEEE.
5. Schroeder, U., T. Mittmann, M. Materano, P.D. Lomenzo, P. Edgington, Y.H. Lee, M. Alotaibi, A.R. West, T. Mikolajick, and A. Kersch, *Temperature-Dependent Phase Transitions in $Hf_xZr_{1-x}O_2$ Mixed Oxides: Indications of a Proper Ferroelectric Material.* Advanced Electronic Materials, 2022: p. 2200265.
6. Mittmann, T., M. Materano, S.-C. Chang, I. Karpov, T. Mikolajick, and U. Schroeder. *Impact of oxygen vacancy content in ferroelectric HZO films on the device performance*. in *2020 IEEE International Electron Devices Meeting (IEDM)*. 2020: IEEE.
7. Vendrell, X., J. Ramírez-González, Z.-G. Ye, and A.R. West, *Revealing the role of the constant phase element in relaxor ferroelectrics.* Communications Physics, 2022. **5**(1): p. 1-10.
8. Jovaní, M., H.c. Beltrán-Mir, E. Cordoncillo, and A.R. West, *Atmosphere-and Voltage-Dependent Electronic Conductivity of Oxide-Ion-Conducting $Zr_{1-x}Y_xO_{2-x/2}$ Ceramics.* Inorganic chemistry, 2017. **56**(12): p. 7081-7088.
9. Masó, N. and A.R. West, *Electronic conductivity in yttria-stabilized zirconia under a small dc bias.* Chemistry of Materials, 2015. **27**(5): p. 1552-1558.
10. Guo, M., N. Masó, Y. Liu, and A.R. West, *Electrical Properties and Oxygen Stoichiometry of $Ba_{1-x}S_xTiO_{3-\delta}$ Ceramics.* Inorganic chemistry, 2018. **57**(1): p. 64-71.

11. Shimizu, T., K. Katayama, T. Kiguchi, A. Akama, T.J. Konno, O. Sakata, and H. Funakubo, *The demonstration of significant ferroelectricity in epitaxial Y-doped HfO_2 film.* Scientific Reports, 2016. **6**(1): p. 1-8.
12. Nishimura, T., L. Xu, S. Shibayama, T. Yajima, S. Migita, and A. Toriumi, *Ferroelectricity of nondoped thin HfO_2 films in TiN/HfO_2/TiN stacks.* Japanese Journal of Applied Physics, 2016. **55**(8S2): p. 08PB01.

Chapter 7: Conclusions and Further work

7.1 Conclusions

This project was targeted on the electrical properties of doped hafnium oxide. At first, the electrical properties of yttria-stabilised hafnia ceramics were studied, particularly to determine ionic and/or electronic conduction with increasing Y^{3+} content and study their response to different pO_2 or/and dc bias application. Arising from this study, YSH ceramics were found to show resistive switching phenomena and its study has been the second objective in this project. Finally, as doped hafnia thin films have ferroelectric properties, impedance spectroscopy was used to investigate their electrical properties.

7.1.1 Electrical properties of YSH ceramics

Synthesis of Y-doped HfO_2, YSH, was carried out by solid state reaction. Phase-pure products of $Hf_{1-x}Y_xO_{2-x/2}$ (x=0.15, 0.30 and 0.45) with homogenous distribution of Y were obtained. The lattice parameter increased with x, consistent with Vegard's law.

Detailed impedance analysis of the three compositions showed three main components related, with decreasing frequency, to bulk, grain boundary and sample-electrode responses. This is confirmed by C' plots for x=0.15 of the same data sets which showed high, intermediate and low frequency plateaus of approximate values 3, 100 pF/cm and 300 µF/cm, respectively. An inclined Warburg spike at low frequency and high value of sample-electrode capacitance is clear evidence of oxide ion conduction in x=0.15.

Impedance of x=0.30 and 0.45 showed a similar response but with two clear differences a) the low frequency spike turned into a small arc at high temperature for x=0.45 b) a clear reduction in the capacitance value of the low frequency plateau from 300 to 0.1 µF/cm occurred with increasing x. The two results indicate the onset of electronic conduction in Y-rich YSH ceramics, similar to results obtained in Y-rich YSZ ceramics [1].

Arrhenius plots indicated that the total conductivities of x=0.15, 0.30 and 0.45 are dominated by the bulk conductivity and the conductivity of x=0.15 is ~ one order of magnitude larger than that of x=0.30 and 0.45. A similar reduction of conductivity with increasing x has been observed in other dopant-rich materials such yttria-, scandic- and calcia-stabilised zirconia [1-5]. This is attributed to attractions of the type $(Y'_{Hf} - V_o^{\bullet\bullet} - Y'_{Hf})$ or aggregation of $(V_o^{\bullet\bullet} - V_o^{\bullet\bullet})$ pairs.

The total conductivities of x=0.30 and 0.45 were similar which can be attributed to the composition of higher yttrium content (x=0.45) having less oxide ion conductivity but more electronic conductivity. In x=0.45, the two effects cancel to give comparable overall conductivity to that of x=0.30.

Impedance measurements in different oxygen partial pressure, pO_2, showed that YSH materials are primarily oxide ion conductors, but with increasing pO_2, they are found to be at the crossover region between the electrolytic and p-type domains. A reversible increase in conductivity with increasing pO_2 is attributed to electronic conduction (holes) which takes place in parallel with the pre-existing oxide ion conduction. The creation of holes is believed to be located on under-bonded oxygen ions. YSH materials are the second example to show the onset of p-type conductivity in fluorite-structured oxides after the family of zirconia-based oxide ion conductors [1, 6, 7].

Results of oxygen transport number measurements (t_i) of all three compositions illustrated that t_i of x=0.15 was less than unity at 800 °C and reduced with x. This means x=0.15 had some electronic conduction which increased with x, consistent with the results obtained in different pO_2.

7.1.2 Resistive-switching in YSH ceramics

The electrical properties of YSH materials under the application of a small applied voltage were studied. Results showed that the conductivity increased a little with increasing applied voltage until a critical voltage at which, a sharp increase in conductivity occurred by 1-2.5 orders of magnitude to reach a low resistance state (LRS). This LRS was retained on subsequently decreasing the applied voltage until a (resit) voltage was reached at which the original high resistance state (HRS) was recovered. This means that YSH materials are the second example to show reversible low field resistive switching in bulk ceramics between OFF (HRS) and ON (LRS) states.

Oxygen partial pressure is a critical factor in this behaviour. The conductivity of LRS was larger and the switching voltage from HRS to LRS was lower with decreasing pO_2. All three compositions x=0.15, 0.30 and 0.45 showed similar results.

The change of conductivity under applied bias voltage appears to occur in two stages. First, at lower applied voltage, the enhanced conductivity is associated with p-type conduction (creation of holes). The p-type conductivity is attributed to the ionisation of

under-bonded oxygen from O^{2-} to O^{-} at the positive electrode. Second, at higher applied voltage, the enhancement in conductivity changed from p-type to n-type behaviour and is attributed to loss of oxygen molecules by double oxidation of oxide ions and injection of electrons at the negative electrode. Such a p-n change has been reported only once before, in YSZ with high Y content ($Y_{0.50}Zr_{0.49}Mg_{0.01}O_{1.74}$) [8].

P- and n-type regions appear to form at opposite electrodes and give rise to the formation of a p-i-n structure. With increasing applied voltage, the thickness of the p- and n-type region appears to increase until a direct contact occurs, leading a dramatic increase in the conductivity at the OFF-ON transition.

7.1.3 Impedance analysis of HZO thin films

Thin films of $Hf_{1-x}Zr_xO_2$ (x=0.4, 0.5, 0.6 and 1) were studied using impedance spectroscopy. Impedance results of all thin films demonstrated a single homogeneous component associated with the bulk layer (nominally, $HfZrO_2$). Resistance measured in different pO_2 indicated that all the thin films had p-type behaviour. In p-type materials, a decrease in resistance is related to the increase in number of holes that can probably be located on either under-bonded oxygen ions or ionisable impurities created during the thin film preparation.

Samples with three different configurations of thin film layers were provided by the Schroeder group. The first one had the layer sequence: p-Si/TiN/$HfZrO_2$/TiN/Ti/Pt. The second was prepared in the same way as the first one, but contained only one layer of top electrode: p-Si/TiN/$HfZrO_2$/TiN. Results show the apparent importance of the top platinum (Pt) electrode in providing a protection layer to give kinetic stability to the thin film device at high temperature.

In a third layer configuration, a layer of SiO_2 was added to give: p-Si/TiN/HfO_2/SiO_2/TiN. Results showed that the overall device impedance was insulating even at high temperature (803 °C) with total resistance of >> 10 MΩ. At high frequency and 803 °C, a second component, R_1, can be seen with a much smaller resistance of ~100 kΩ. This second component can possibly be related either to HfO_2 or a TiO_2 layer formed by oxidation of TiN at high temperature. However, in general, the SiO_2 layer was found to block the current completely which was the reason for preparing and measuring this thin film sample.

The temperature dependent ε_r for HZO thin film samples showed a sharp permittivity peak at ~465-471 °C that appears to be related to a ferroelectric-paraelectric phase transition

at the Curie temperature, T_c. The maximum permittivity value of all thin film samples is ~10600-11100. This result is the first to report the existence of peak permittivity and confirmed the XRD analysis which showed the phase transition of hafnia ferroelectric thin film from orthorhombic (ferroelectric) phase to monoclinic at ~465 °C [9-11].

7.2 Further work

The effect of external dc bias on the electrical properties of materials has come more frequently to attention in two important areas, flash-sintering (FS) and resistive-switching. FS is a novel, friendly and rapid sintering technology that uses the application of bias voltage and heat to sinter certain materials in a few seconds and at much lower temperature than need for conventional sintering. In resistive switching, the resistance of a material changes reversibly in response to applying a dc bias voltage. It is clear that the utilization of external bias voltage is the key factor in both processes.

Based on the results in this project, the conductivity of YSH15 increased with increasing the applied dc voltage until it reached a lower resistance state. At low voltage, the increase in conductivity is related to the generation of holes at the positive electrode while at high voltage, the increase in conductivity is dominated by the generation of electrons at the negative electrode. This leads to formation of a p-i-n structure which collapsed with increasing dc voltage giving a dramatic enhancement in the conductivity, described more previously.

In Chapter 5, Figure 5.2, YSH15 pellets showed a flash luminescence event occurred when the sample reached the lower resistance state and disappeared when the sample reached the higher resistance state during the application of the bias. This flash luminescence appears to be the same as what happens in flash-sintering, which indicates a clear connection between resistive switching and flash luminescence in yttria-stabilised hafnia ceramics. Further investigation of this subject is important in order to understand whether creation of a p-n electronic junction is important to give the flash event as well as to assist flash sintering.

The two examples known so far that show resistive switching behaviour in bulk ceramics are Ca-doped $BiFeO_3$ [12] and Y-doped HfO_2. Both examples have oxygen vacancies as a result of a charge compensation mechanism and both have p-type electronic conduction. Therefore,

there is a big question about the importance of oxygen vacancies and p-type electronic conduction in resistive switching behaviour of bulk materials. A more extensive study of possible low-field resistive switching of other bulk ceramics will help to give a better understanding of RS phenomena via answering the following questions.

I. Is mixed conduction important in resistive switching behaviour?
II. Is hole conductivity in p-type materials essential to have RS behaviour?
III. Is electron conductivity alone in n-type materials sufficient to have RS behaviour?

For thin film memristive devices, there are current issues involved in understanding the mechanism of RS as well as developing the scalability, retention and uniformity of the conductive filaments. Oxide ion conductors with low level of electronic conduction such as $Na_{0.5}Bi_{0.5}TiO_3$ (NBT) [13] have been shown to have resistive switching behaviour with a high performance (stable switching, strong endurance, uniformity, fast speed, low switching voltage and free electroforming process) when fabricated as thin films [14]. Therefore, a YSH15 shows a resistive switching in bulk ceramics, it would be interesting to prepare YSH15 thin film devices, analyse their resistive-switching behaviour and compare it with those of typical memristive devices.

In chapter 6, the impedance data of $Hf_{1-x}Zr_xO_2$ thin films without top electrodes did not show a permittivity peak maximum. Possibly, the top electrode is important for providing a protection layer to TiN (to avoid oxidation) and give kinetic stability for the electrical behaviour of the thin film device. Therefore, $Hf_{1-x}Zr_xO_2$ (x=0, 0.4, 0.5, 0.6, 1) thin films samples with top electrode would be studied by impedance spectroscopy in order to see the effect of Zr on the thin film properties.

7.3 References

1. Jovaní, M., H.c. Beltrán-Mir, E. Cordoncillo, and A.R. West, *Atmosphere-and Voltage-Dependent Electronic Conductivity of Oxide-Ion-Conducting $Zr_{1-x}Y_xO_{2-x/2}$ Ceramics.* Inorganic chemistry, 2017. **56**(12): p. 7081-7088.
2. Arachi, Y., H. Sakai, O. Yamamoto, Y. Takeda, and N. Imanishai, *Electrical conductivity of the ZrO_2–Ln_2O_3 (Ln= lanthanides) system.* Solid State Ionics, 1999. **121**(1-4): p. 133-139.
3. Ramírez-González, J. and A.R. West, *Electrical properties of calcia-stabilised zirconia ceramics.* Journal of the European Ceramic Society, 2020.
4. Norberg, S.T., S. Hull, I. Ahmed, S.G. Eriksson, D. Marrocchelli, P.A. Madden, P. Li, and J.T. Irvine, *Structural Disorder in Doped Zirconias, Part I: The $Zr_{0.8}Sc_{0.2-x}Y_xO_{1.9}$ (0.0≤ x≤ 0.2) System.* Chemistry of Materials, 2011. **23**(6): p. 1356-1364.
5. Marrocchelli, D., P.A. Madden, S.T. Norberg, and S. Hull, *Structural Disorder in Doped Zirconias, Part II: Vacancy Ordering Effects and the Conductivity Maximum.* Chemistry of Materials, 2011. **23**(6): p. 1365-1373.
6. Masó, N. and A.R. West, *Electronic conductivity in yttria-stabilized zirconia under a small dc bias.* Chemistry of Materials, 2015. **27**(5): p. 1552-1558.
7. Vendrell, X. and A.R. West, *Induced p-type semiconductivity in yttria-stabilized zirconia.* Journal of the American Ceramic Society, 2019. **102**(10): p. 6100-6106.
8. Jovaní, M., H. Beltrán-Mir, E. Cordoncillo, and A.R. West, *Field-induced pn transition in yttria-stabilized zirconia.* Scientific Reports, 2019. **9**.
9. Schroeder, U., T. Mittmann, M. Materano, P.D. Lomenzo, P. Edgington, Y.H. Lee, M. Alotaibi, A.R. West, T. Mikolajick, and A. Kersch, *Temperature-Dependent Phase Transitions in $Hf_xZr_{1-x}O_2$ Mixed Oxides: Indications of a Proper Ferroelectric Material.* Advanced Electronic Materials, 2022: p. 2200265.
10. Shimizu, T., *Ferroelectricity in HfO_2 and related ferroelectrics.* Journal of the Ceramic Society of Japan, 2018. **126**(9): p. 667-674.
11. Shimizu, T., K. Katayama, T. Kiguchi, A. Akama, T.J. Konno, O. Sakata, and H. Funakubo, *The demonstration of significant ferroelectricity in epitaxial Y-doped HfO_2 film.* Scientific Reports, 2016. **6**(1): p. 1-8.

12. Masó, N., H. Beltrán, M. Prades, E. Cordoncillo, and A.R. West, *Field-enhanced bulk conductivity and resistive-switching in Ca-doped $BiFeO_3$ ceramics.* Physical Chemistry Chemical Physics, 2014. **16**(36): p. 19408-19416.
13. Li, M., M.J. Pietrowski, R.A. De Souza, H. Zhang, I.M. Reaney, S.N. Cook, J.A. Kilner, and D.C. Sinclair, *A family of oxide ion conductors based on the ferroelectric perovskite $Na_{0.5}Bi_{0.5}TiO_3$.* Nature Materials, 2014. **13**(1): p. 31-35.
14. Yun, C., M. Webb, W. Li, R. Wu, M. Xiao, M. Hellenbrand, A. Kursumovic, H. Dou, X. Gao, S. Dhole, D. Zhang, A. Chen, J. Shi, K.H.L. Zhang, H. Wang, Q. Jia, and J.L. MacManus-Driscoll, *High performance, electroforming-free, thin film memristors using ionic $Na_{0.5}Bi_{0.5}TiO_3$.* Journal of Materials Chemistry C, 2021. **9**(13): p. 4522-4531.